Utilisation de composants sur étagère pour la propulsion des nanosatellites : à quel prix ?

Gary Quinsac

PSL UNIVERSITÉ PARIS

THÈSE DE DOCTORAT
DE L'UNIVERSITÉ PSL

Préparée à Observatoire de Paris

From commercial off-the-shelf to expected propulsion in nanosatellites

Soutenue par
Gary QUINSAC
Le 10 Septembre 2019

École doctorale n°127
Astronomie et astrophysique d'Ile-de-France

Spécialité
Astronomie et Astrophysique

Composition du jury :

Jérôme LESUEUR Professeur, ESPCI	*Président*
Christelle PITTET Ingénieure HDR, CNES	*Rapporteur*
Stéphane MAZOUFFRE Directeur de Recherche, CNRS	*Rapporteur*
Laurent DUSSEAU Professeur, Université de Montpellier	*Examinateur*
Käthe DANNENMAYER Docteur, ESA	*Examinateur*
Benoît MOSSER Professeur, Observatoire de Paris	*Directeur de thèse*
Boris SEGRET Ingénieur, Observatoire de Paris	*Co-encadrant de thèse*
Christophe KOPPEL Ingénieur, KopooS Ind.	*Co-encadrant de thèse*

l'Observatoire de Paris

À mon père Jean-Pierre
À ma mère Corinne
À mon parrain François

Aknowledgements

This thesis was originally funded with a grant from PSL University. It was carried out in the frame of the BIRDY-T project, a technological development of autonomous navigation for interplanetary/deep space nanosatellites. This project is supported by C^{2}ERES, the space pole of PSL University.

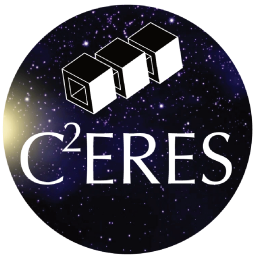

Je tiens à remercier toutes les personnes qui ont contribué au succès de ma thèse et qui m'ont aidé lors de la rédaction de ce mémoire.

Je voudrais dans un premier temps remercier mes encadrants pour leur investissement et leurs précieux avis : mon directeur de thèse Benoît Mosser, et mes co-encadrants, Boris Segret et Christophe Koppel. Leur bienveillance et leur compréhension, ainsi que celles de Pierre Drossart, directeur de recherche au LESIA, m'ont été chères dans les moments difficiles.

Je souhaite également remercier les différentes personnes impliquées dans le projet BIRDY-T, en commençant par Daniel Hestroffer, Marco Agnan et Jordan Vannitsen. Je n'oublie bien évidemment pas l'ensemble des stagiaires ayant de près ou de loin participé à l'avancée de ce projet ni les étudiants et chercheurs de la National Cheng Kung University.

J'adresse aussi mes sincères remerciements aux personnels de l'Observatoire de Paris, sans lesquels rien de tout cela n'aurait été possible. Ils auront su me tirer de quelques mauvais pas administratifs.

Nombreux sont les proches que je souhaiterais mentionner, pour leur écoute et leur aide :

- *Chloé, qui m'a aidé en prenant le temps de partager sa propre expérience de la thèse.*

- *Julien, Jean-François et Vivien, pour avoir relu et corrigé mon mémoire. Leurs conseils de rédaction ont été précieux.*
- *Amélie, Fanny, Anaïs et Daniel, qui se sont prêtés au jeu des répétitions de soutenance.*
- *Gilles, pour m'avoir communiqué sa motivation au travers de ses nombreux encouragements.*
- *Sébastien, mon collègue de bureau, qui s'est brillamment assuré que je ne dépérisse pas durant les derniers mois.*
- *Benjamin, Maxime et tous les autres, trop nombreux pour être cités ici. J'espère avoir réussi à vous exprimer ma gratitude.*

Enfin, je tiens à témoigner toute ma reconnaissance à Sarah, qui m'a accompagné durant les joies et les peines ayant émaillé ces dernières années. Son soutien, sa patience et ses encouragements m'auront porté. Je lui dois bien plus que cette thèse.

Content

Acronyms

ACT Attitude Control Thruster.
ADCS Attitude Determination & Control System.
AOCS Attitude & Orbit Control System.

BOL Beginning Of Life.

CDS CubeSat Design Specification.
CGT Cold Gas Thruster.
CNES Centre National d'Études Spatiales.
COE Classical Orbital Element.
COG Center Of Geometry.
COM Center Of Mass.
COP Center Of Pressure.
COTS Commercial Off-The-Shelf.

DCM Direction Cosine Matrix.

ECEF Earth-Centered Earth-Fixed.
ECI Earth-Centered Inertial.
EMC ElectroMagnetic Compatibility.
ESA European Space Agency.
ESD ElectroStatic Discharge.

FEEP Field Emission Electric Propulsion.

GEO Geostationary Earth Orbit.
GNC Guidance Navigation & Control.
GTO Geostationary Transfer Orbit.

HET Hall Effect Thruster.

IFOD In-Flight Orbit Determination.
IGRF International Geomagnetic Reference Field.

JAXA Japan Aerospace Exploration Agency.

LEO Low Earth Orbit.
LLA Latitude Longitude Altitude.
LTI Linear Time-Invariant.

MEO Medium Earth Orbit.
MSL Mars Science Laboratory.
MTQ Magnetic TorQuer.

NASA National Aeronautics and Space Agency.
NEA Near Earth Asteroid.
NED North East Down.
NEO Near Earth Object.

OAP Orbit Average Power.

PD Proportional Derivative.
POD Precise Orbit Determination.
PPT Pulsed Plasma Thruster.

RAD Radiation Assessment Detector.
RF Radio Frequency.
ROC Rate Of Change.
RW Reaction Wheel.

SADT Structured Analysis & Design Technique.
SEE Single Event Effect.
SPE Solar Particle Event.
SRP Solar Radiation Pressure.
SSO Sun Synchronous Orbit.

TCM Trajectory Correction Maneuver.
TID Total Ionizing Dose.
TRL Technology Readiness Level.

UHF Ultra High Frequency.
UPS Unified Propulsion System.

VAT Vacuum Arc Thruster.
VHF Very High Frequency.
VLBI Very-Long-Baseline Interferometry.

List of Symbols

Mathematical Notations

$\mathbf{v}$	Vector
$\mathbf{v} \cdot \mathbf{w}$	Scalar product between vectors $\mathbf{v}$ and $\mathbf{w}$
$\mathbf{v} \times \mathbf{w}$	Vector product between vectors $\mathbf{v}$ and $\mathbf{w}$
$\hat{\mathbf{v}}$	Unit vector
$\boldsymbol{\omega}_a^{ab}$	Rotational velocity of frame a with respect to frame b, seen in the frame a
$\mathbf{M}$	Matrix
$\mathbf{M}^{-1}$	Inverse of $\mathbf{M}$
$\mathbf{M}^T$	Transpose of $\mathbf{M}$
$\det \mathbf{M}$	Determinant of $\mathbf{M}$
$\mathbf{I}_{n\times n}$	Identity matrix
$\mathbf{M}_{F'F}$	Transformation matrix from frame F to F'
q	Quaternion
q_0	Quaternion's scalar part
$\mathbf{q}_{1:3}$	Quaternion's vector part
$q_{F'F}$	Quaternion from frame F to F'

Physical Constants

c	Speed of light in vacuum	$299,792,458\,[\mathrm{m\,s^{-1}}]$
G	Gravitational constant	$6.67408 \times 10^{-11}\,[\mathrm{m^3\,kg^{-1}\,s^{-2}}]$
g_0	Standard acceleration due to gravity	$9.80665\,[\mathrm{m\,s^{-2}}]$

Standard Symbols

ΔV	Incremental velocity	$[\mathrm{m\,s^{-1}}]$
v_e	Exhaust velocity	$[\mathrm{m\,s^{-1}}]$
m_p	Mass of propellant	[kg]
I_{sp}	Specific impulse	[s]
I_{ssp}	System specific impulse	[s]
I_{tot}	Total impulse	[N s]

$\oplus$	Earth	
$\odot$	Sun	
ν	True anomaly	[rad]
a	Semimajor-axis	[m]
e	Eccentricity	[N/A]
i	Inclination	[rad]
ω	Argument of perigee	[rad]
Ω	Right ascension of the ascending node	[rad]
$\mathbf{I}$	Inertia tensor	$[\mathrm{kg\,m^2}]$
$\mathbf{H}$	Angular momentum	$[\mathrm{kg\,m^2\,s^{-1}}]$
$\mathbf{T}$	Torque	$[\mathrm{N\,m}]$
$\mathbf{B}$	Magnetic field	[T]
$\boldsymbol{\omega}$	Angular velocity vector	$[\mathrm{rad\,s^{-1}}]$
$\mathbf{x}$	m-dimensional state vector	
$\mathbf{y}$	n-dimensional state vector	

List of Figures

List of Tables

Introduction

While space exploration is proving to be more and more costly, can CubeSats propose interesting alternatives, in complement to larger systems? This will depend on their capacity to unlock remaining barriers, among which is orbital autonomy. Paris Observatory - Université Paris Sciences & Lettres (PSL) accompanies this space trend with several undergoing projects, from Earth science missions to interplanetary constellations of nanosatellites. But first, what is a nanosatellite, and what purpose does it serve?

Since the beginning of the Space Age in 1957 with the launch of Sputnik 1, progress has been enormous. Yet, after a golden age during the first decades, major projects tend to become scarce. Investments for the scientific exploration of space decrease, while the space business flourishes, and main agencies have to team up to achieve large exploration missions with a complicated payload. Despite countless successes, the need for such cooperation is also a symptom of the difficulties encountered. This is where nanosatellites, and CubeSats in particular, come into play. They propose to build single-instrument satellites at low cost, hence opening up access to space to new actors in general, and laboratories in particular. The reduction in size and mass of satellites has been going on for quite some time now, but who could have imagined that the 21^{st} century would start with a new standard of $\sim$ 1-kg satellite, when classical satellites used to weigh several tons? Yet here we are, and the sustainability of this new approach requires innovative mission concepts. For laboratories, this new approach implies to develop skills in platform development and to design a space mission from beginning to end. This can be considered as a chance or a risk.

Similarly to what happened for bigger satellites, the performance of small platforms is increasing by the day, thanks to the miniaturization of key components. However, CubeSat missions are still mainly limited by their rideshares and usually remain in Low Earth Orbit (LEO). In this regard, the advent of propulsion systems for these nanosatellites is expected to guarantee their bright future, giving them access to a variety of new orbits. In this manner, interplanetary CubeSat missions are on the rise, as demonstrated by the twin Mars Cube One (MarCO) CubeSats [1]. In order to avoid any additional risk, they were considered as an independent mission; therefore they required propulsion provided by a Cold Gas Thruster (CGT), and finally could provide a real-time communication link between the Earth and Insight, during the Martian descent of the latter.

Propulsion is only one aspect of the building bricks leading to orbital autonomy. Although trajectory maneuvers and their implementation have been thor-

oughly studied for classical satellites, the high level of constraints on CubeSats in terms of mass, volume and power, makes the transition delicate. Orbit, attitude and power subsystems limit too optimistic performance available in literature. This thesis falls within this context and aims to clarify this crucial aspect of future nanosatellites by adopting a high-level approach.

Ambitious scientific applications, which have motivated this work, were suggested and are now investigated at Paris Observatory. The first chapter presents two of them, both based on interplanetary CubeSats that will have to perform trajectory correction maneuvers to carry out their mission. The first one proposes to perform space weather measurements on an Earth-Mars trajectory so as to assess the radiative environment. The second one is meant to estimate the mass distribution of an asteroid by performing radio-science measurements in close proximity.

Since orbital control is expected to boost CubeSats potential, chapter two digs further in the world of propelled nanosatellites. By performing a state of the art of current technologies based on well-known performance indexes, we identify intrinsic system limits. If some propulsion concepts are more promising than others, we need to develop a proper way for selecting them. Furthermore, their integration and the numerous coupling with other components also need to be considered.

The system integration of propulsion is carried out with a functional analysis of the Attitude & Orbit Control System (AOCS) for our two scientific missions. Hence, chapter three gathers the relevant considerations for the expression of technical requirements. That is in this chapter that the need of relevant case studies in Earth orbits to investigate the coupling between attitude and orbit control is clearly identified.

The fourth chapter introduces the various concepts necessary to the development of a simulation environment for attitude and orbit control. We analyze the attitude control, then present a trajectory solver in Earth orbit, based on the perturbed two-body problem. The simulation we finally propose brings together those two aspects and can now be used to investigate our Earth orbiting case studies.

The identification of the required components for the two fictional case studies is developed in the fifth chapter, followed by the simulation of their performance and interactions. The investigation of configurations resulting from different integration errors shows that neglecting those mutual impacts will automatically result in dramatic increase, either of maneuver duration or propellant consumption, and even in mission loss in some cases.

Unfortunately, these perturbations are not the only difficulties, as we can see all along this work. Commonly used indexes presented in the second chapter are not able to relay these issues. What happens if the propulsion system requires more power than what is commonly available on CubeSats? How can the need for a propulsion concept to provide both attitude and orbit control be taken into account? Such questions, and others, have led to the proposition of a new performance indicator, inspired by the work of Erichsen [2], and presented in the last chapter.

From the scientific cases investigated at the Paris Observatory to representative case studies in Earth orbit and to a novel performance index, we arrive to the end of this work, where the lessons learned can be discussed in light of future developments.

CHAPTER I

Scientific Applications

I.1 - Twenty Years of Revolution

Twenty years ago, the proposition of a new format of satellites hastened the emergence of what is now called the *New Space*: the CubeSat standard. It was created in 1999 by California Polytechnic State University, San Luis Obispo University and the Space Systems Development Lab of Stanford University. The idea behind this was to facilitate the education of space scientists and engineers, as well as provide a low-cost platform for testing and for space qualification of future small payloads. The "base unit" (U) of a CubeSat is a 10 cm long cube of $\sim$ 1.33 kg. Because the cost of a satellite scales well with its mass, it is usual to classify satellites according to their mass, as evidenced in figure I.1. CubeSats are among the nanosatellite family (1 kg to 50 kg). Just above are the small satellites, weighing less than 300 kg. Satellites smaller than nanosatellites are called picosatellites. One example of picosatellite is the ChipSat [3]. Among the satellite family, this puts CubeSats almost at the low end, while classic satellites weigh several tons. In terms of cost, a CubeSat costs approximately one million euros, although this depends to a large extent on the mission.

The first success of the standard came with the development of a deployer capable of accommodating three 1U CubeSats [4] and releasing them in space from a launcher. In addition to the initial form factor and mass, this came from a number of requirements:

- Safety. The deployer must ensure the protection of the launch vehicle and primary payload from any kind of interference from the CubeSats, and the release of a CubeSat must minimize the risks of collision with the launch vehicle or other CubeSats.

- Standardization. The deployer must interface with a variety of launch vehicles with minimum modifications and with no change of the CubeSat standard. It should also allow different numbers of CubeSats to be launched on a given mission, while not resulting in complicated and expensive CubeSat construction.

From that time on, it was possible to access to space without having to pay an

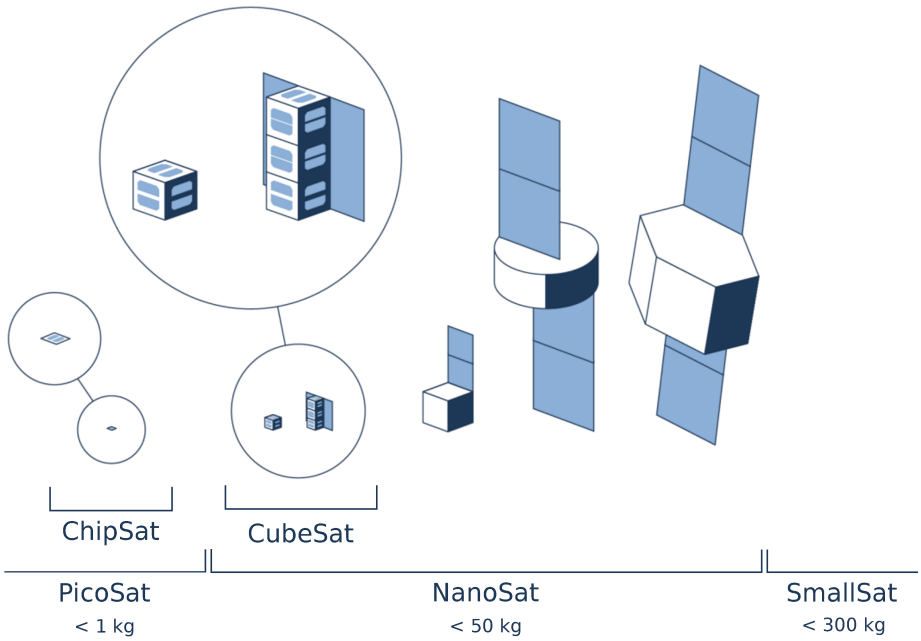

Figure I.1: Common classification of satellites by their mass. Credit: C^{2}ERES

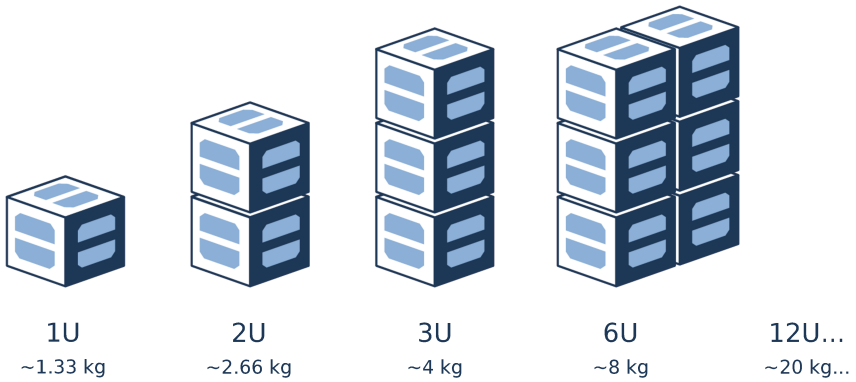

Figure I.2: CubeSat standard. Credit: C^{2}ERES

unaffordable launch. Those tiny satellites could be piggy-backed by a host mission whose orbit they would share. This is how we saw the multiplication of 1U CubeSat powered by $\sim 1\,\mathrm{W}$ when covered with solar cells. The low capacity of the UHF/VHF antennas that could be accommodated in such a constrained satellite were sufficient to ensure communication with Low Earth Orbit (LEO). Universities benefited from this new access to space, and countries saw in this format the opportunity to become a space nation. We can cite the Colombian Libertad 1, the Vietnamese F-1 or the Estonian ESTCube-1.

It took a decade for the standard to really disseminate, and first years have seen a high number of mission failures [5], often related to deficiencies during integration and tests. As time went on, CubeSats made of assembled units started emerging (see figure I.2). In the last CubeSat Design Specification (CDS) [6], cubesat.org sets the requirements for 1.5U (length of 15 cm and mass of 2 kg), 2U (length of 20 cm

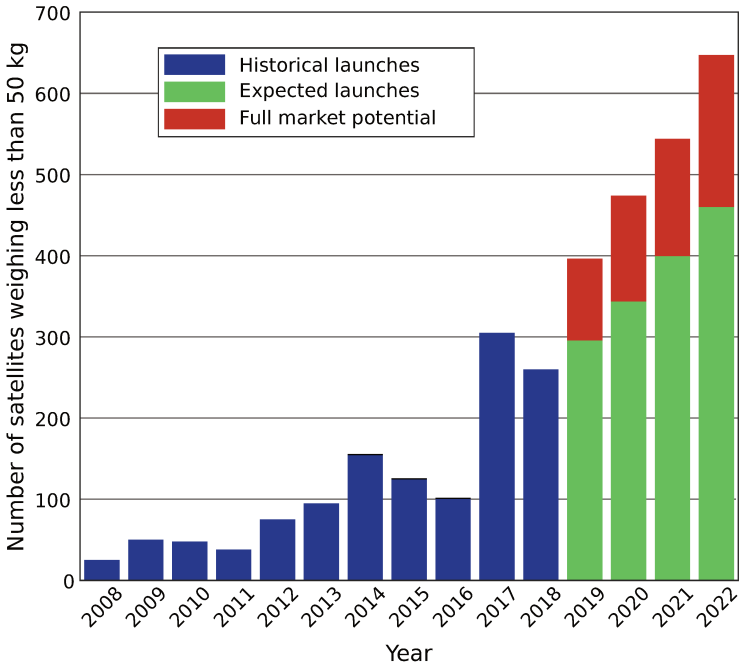

Figure I.3: Evolution of the number of nano/micro-satellite launches. CubeSats represent the majority of those launches. Data from SpaceWorks [7].

and mass of 2.66 kg), 3U (length of 30 cm and mass of 4 kg) and 3U+ (3U with a "tuna can"). More recently, 6U, 12U and up to 27U CubeSats emerged, proving the vitality of the *New Space*. Yet, some of these bigger CubeSats tend to drift away from the initial philosophy, and requirements and constraints are now sometimes discussed directly with the launch provider/main mission. This form factor has now become very popular, as shown by the number of launches of nano/micro-satellites (1 kg to 50 kg) in figure I.3 [7].

Many private companies entered the *New Space* and participated to its growth. The classic case-by-case development of subsystems is now replaced by Commercial Off-The-Shelf (COTS), components designed by manufacturers to be easily installed and used with other existing components. Hence, all the essential subsystems to build a CubeSat are available and it has become possible to send a satellite without having to design a single component. One can cite companies such as GomSpace (www.gomspace.com), ISIS (www.isispace.nl), Berlin Space Technologies (www.berlin-space-tech.com), Blue Canyon Technologies (www.bluecanyontech.com), CubeSpace (www.cubespace.co.za), or DHV Technology (www.dhvtechnology.com). With the miniaturization of technologies, the performance of essential subsystems has highly improved, paving the way to more complex missions. Deployable solar panels provide an increased available power, S-band and X-band antennas allow the transmission of large amount of data, all-in-one Attitude Determination & Control System (ADCS) enables reliable pointing (with various accuracy), and so on. Regarding this thesis, propulsion system providers are now scaling down solutions previously designed for larger satellites (see section II.3) to enable more complex mission profiles with CubeSats. A state of the art of small spacecraft technologies is proposed by the National Aeronautics and Space Agency (NASA) [8].

Figure I.4: MSL-Curiosity rover and its Radiation Assessment Detector (RAD) instrument (left). Schematic of the working principle of RAD (right). Credit: NASA and Southwest Research Institute.

It is in this favorable context that two mission profiles emerged at Paris Observatory. They are the scientific motivations to this thesis. In the following sections, I introduce those two mission concepts based on the extensive presentation made by B. Segret in his PhD. dissertation [9].

I.2 - Interplanetary Space Weather — Cruise Context

As seen in the previous section (I.1), CubeSats rely on rideshares to access to space. Although CubeSats are mainly launched in LEO, the improvement of COTS paves the way to more complex missions, including deep space missions. Rideshares to interplanetary targets are rare but somewhat regular (see section II.1). The Mars Cube One (MarCO) CubeSats are a perfect example of nanosatellites deployed on an Earth-Mars trajectory [1]. Such interplanetary trajectories open up new fields of application for CubeSats, among which are in situ measurements. From this observation emerged the idea of a space weather CubeSat that would fill the data gaps of interplanetary highly energetic particles.

The BIRDY project (Bleeping Interplanetary Radiation Determination Yo-yo), started in 2013, is inspired by the Radiation Assessment Detector (RAD) instrument on-board the rover Curiosity, which is part of the Mars Science Laboratory (MSL) from NASA [10] (see figure I.4). The instrument was turned on during its way to Mars and collected data about two solar particle events that occurred over this period. Because those events were also detected by sensors on Earth and by probes orbiting Mars, their propagation was measured twice in multiple locations of the solar system. In particular, such measurements are interesting for evaluating the dose of highly energetic particles a human crew would receive on a Mars journey. Although RAD measurements were imprecise (it was not calibrated to operate inside MSL), they tend to minimize alarming projections. More generally, cosmic rays remain poorly observed since they require in situ measurements.

BIRDY is a project for a CubeSat dedicated to in situ measurements of the

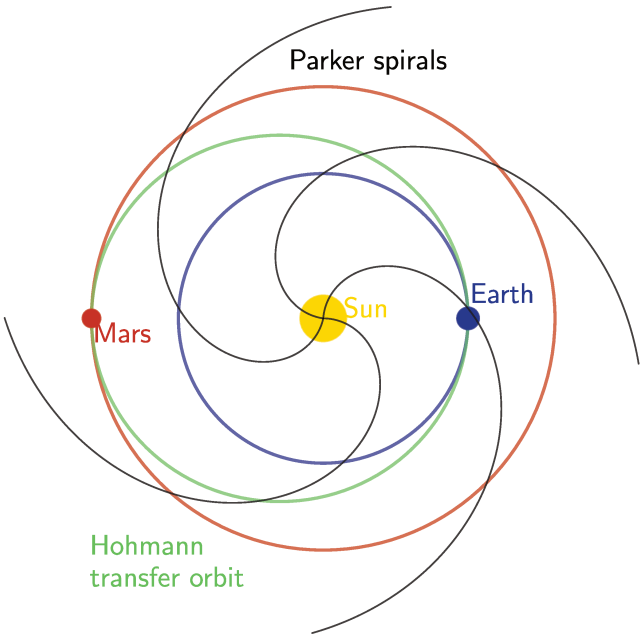

Figure I.5: Parker spirals for a given energy (black) on an Earth-Mars transfer trajectory (green). The orbits of the Earth and Mars are in blue and red respectively. Tick marks indicate constant time intervals (in days). Inspired by Posner et al. [12].

Hohmann-Parker effect on an Earth-Mars trajectory (the concept remains of interest on any interplanetary trajectory). Parker spirals describe the propagation of the solar wind in the interplanetary space (see figure I.5). It follows that a spacecraft released on an Earth-Mars transfer orbit will detect the same flux of particles as detectors at Earth and Mars, but at different times. Essential propagation and comparative studies can result from such a mission.

The question is now: can the payload fit to CubeSat constraints? The team who developed the instrument is confident that a miniaturized version of RAD, that could fit a 3U CubeSat, is feasible [9]. The light power demand and produced data volume are compatible with an interplanetary journey. Yet, one particular limitation is the incapacity to distinguish incident and secondary particles detailed in [11], but it does not question the pertinence of the mission.

The initial trajectory is based on the proposition of a human spaceflight to Mars in 2018 from Dennis Tito [13]. This trajectory, with a free return after a Mars fly-by, is represented in figure I.6. The plan is to benefit from a rideshare to Mars. Once the main mission has been injected on the interplanetary trajectory, the CubeSat can be deployed. A first set of measurements is then performed on the way to Mars. During the fly-by of the red planet, data are transferred to a Mars orbiter (used as a data relay). If the fly-by goes to plan, a second set of measurements is possible on the free return to Earth before a final data transmission in the vicinity of the Earth.

We now review the crucial aspects of the BIRDY mission concept:

- The science case has been thoroughly investigated by Jordan Vannitsen in his PhD [14]. He presents a tool for the exploitation of heterogeneous measurements of solar energetic particles by various probes, particularly to support this CubeSat mission [11]. The 1U payload is compatible with a 3U CubeSat

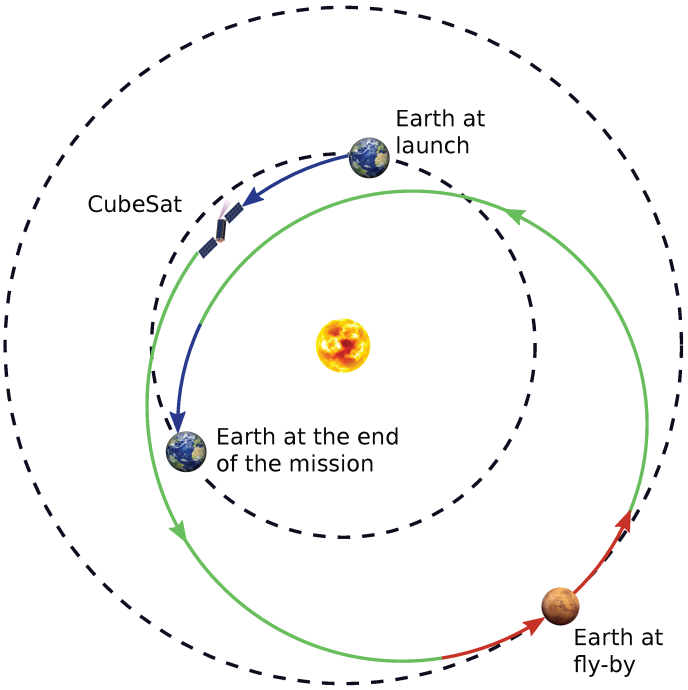

Figure I.6: Earth-Mars Hohmann transfer orbit. Adapted from Tito et al. [13].

platform and requires to slowly spin in the ecliptic plane to detect incident particles.

- On an Earth-Mars trajectory, telecommunication with ground stations on Earth is impossible, especially with classic CubeSat equipment. Therefore, the spacecraft must be autonomous during the majority of his life, which imposes drastic constraints. The first one concerns the determination of its orbital position. To that end, B. Segret is developing an In-Flight Orbit Determination (IFOD) concept, topic of his PhD [9]. The IFOD must provide an estimate of the position of the spacecraft without any ground assistance. The precision of this estimate has to be accurate enough to detect any drift from the reference trajectory, and enable propulsion to correct it. Those corrections must at least permit the data relay with a Martian orbiter. Indeed, only the first half of the trajectory is mandatory for the minimal success of the mission (including the data relay). However, the scientific bonus coming from a second set of measurements is non-negligible.

- A propulsion system is necessary to perform trajectory corrections during the cruise and enable the expected trajectory, based on the information coming from the IFOD. Catching the proper free-return trajectory consists in ending the Mars fly-by in the correct orbital plane to meet the Earth. First investigations have shown that only several meters per second of ΔV are necessary to significantly modify the resulting orbital plane [15].

- A sizing of the telecommunication subsystem was performed in both Ultra High Frequency (UHF)/Very High Frequency (VHF) and in S-band for commissioning and data relay modes. A weekly beacon shall transmit the general

status of the spacecraft to an antenna of the Very-Long-Baseline Interferometry (VLBI).

While this application of the BIRDY project is currently in standby, many studies were conducted and led to the identification of technological obstacles. Since then, all the focus has been on the IFOD, and the name of the project changed to BIRDY-T to acknowledge the navigation technology under development.

Hereafter, this concept of operation may be referred to as cruise context.

I.3 - Space Geodesy of Asteroids — Proximity Operations Context

In the recent years, a growing interest for small bodies in general, and asteroids in particular, appeared in the space community. The probe Rosetta from European Space Agency (ESA) successfully investigated comet 67P/Churyumov-Gerasimenko from 2,014 to 2,016 [16], while the Japan Aerospace Exploration Agency (JAXA) probes Hayabusa and Hayabusa 2 were both designed to study and return samples from Near Earth Asteroid (NEA) targets, Itokawa and Ryugu respectively [17, 18]. Hayabusa brought asteroid fragments back to Earth in 2010 and Hayabusa 2 is supposed to do the same in 2023. NASA has not been left behind since the OSIRIS-REx satellite is currently probing NEA Benu and is also expected to return with a sample in 2023 [19]. This enthusiasm for Near Earth Object (NEO) is motivated by several prospects:

- Scientists predict that the study of the small bodies of the solar system will tell us more about its formation and our origins.
- Mining exploration has become an economic motivation. For instance, Luxembourg encourages the creation of start-ups and the installation of companies dedicated to asteroid mining.
- Earth protection and asteroid impact avoidance is another interest, just as important for the public.

From there, CubeSat mission concepts to small bodies started flourishing. The QBDIM mission emerged at Paris Observatory in 2015 under the conduct of Daniel Hestroffer (principal investigator). The scientific objective is to achieve radio science measurements during free-fall arcs in the very close proximity of an asteroid, using the autonomous navigation from BIRDY-T (the two projects quickly merged under the name BIRDY-T). Between two successive free-fall arcs, a propulsive maneuver is necessary to return in the vicinity of the target, as shown in figure I.7.

This operational process is inspired by the hyperbolic arcs performed by Rosetta in order to determine the gravity field of 67P/Churyumov-Gerasimenko before getting closer to the comet. Contrary to Rosetta, the CubeSat would not have an important team of experts ready to operate the probe and process the data. It is

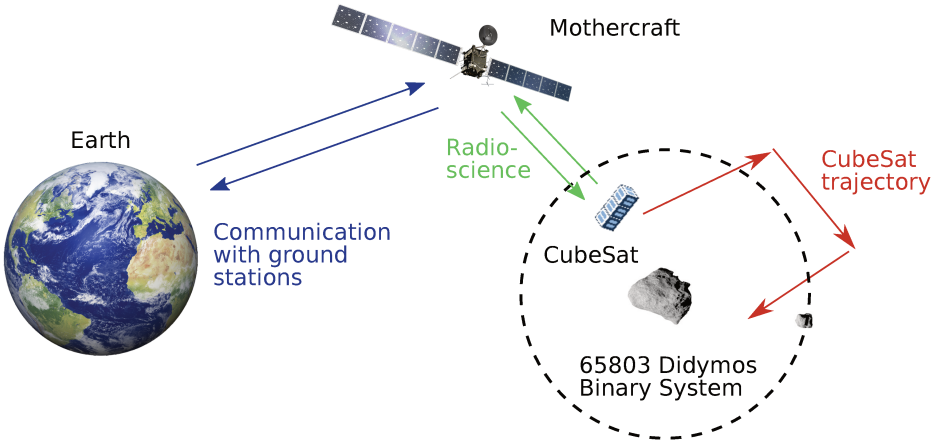

Figure I.7: Mission profile for a CubeSat conducting radio science measurements around Didymos.

meant to be deployed by a mothercraft in the vicinity of an asteroid, after which it is expected to be as autonomous as possible not to overload the main mission.

The radio science concept relies on Doppler measurements performed on signals between the CubeSat and the mothercraft or VLBI ground stations on Earth to reconstruct precisely the path of the CubeSat. The deflection of the nanosatellite trajectory by the gravity field of an asteroid will tell us about its mass. Thanks to images, one can use trajectography to deduce the density of the asteroid, which is usually a characteristic hard to evaluate because of the various porosity and composition of these bodies. Similarly, its homogeneity can be inferred thanks to overflights at different latitudes. At the end of the mission, a slow crash on the surface of the target may be feasible to get precious information, like Rosetta did on comet 67P/Churyumov-Gerasimenko.

Radio science for geodesy primarily requires the exchange of signals between a spacecraft whose trajectory is perturbed and a reference. The signals must be perfectly dated to post-reconstruct the satellite position and velocity with sufficient precision. In case it is a one-way signal, meaning that the probe sends a signal that is received by the ground station or the mothercraft, an ultra-stable oscillator (USO) must be carried on-board the probe. The stability of a USO depends on a precise and complex thermal regulation that would be hard to provide on such a small platform, without mentioning the need for regular clock synchronization. On the contrary, a solution with two-way signals, in which the probe only requires a transponder to receive and send back the signal to the emitter, is largely feasible with a CubeSat. In case the emitter is the mothercraft, it must possess a USO, which may be problematic. Yet, performing the radio science with the main satellite permits to circumvent perturbations to the signal due to Earth atmosphere (local meteorological measurements are usually performed to subtract the atmospheric effect). Whether the science is carried out with ground stations or with another satellite, the transmissions need to be in S-band or X-band to obtain a sufficient resolution. Such antennas are becoming more common on these small platforms.

Once the measurements have been transferred to the ground segment, the Precise Orbit Determination (POD) can start. Its objective is to reconstruct precisely

the trajectory of the CubeSat. Tools exist to fit the gravitational model of the body to the radio science measurements, such as GINS (Géodésie par Intégrations Numériques Simultanées) made available by Centre National d'Études Spatiales (CNES). The POD is essential because its performance sets requirements for the entire upstream measurement chain.

As an accompanying probe, the scientific targets will depend on the main satellite and so does the mission type. Two very different types of mission exist: fly-by and rendezvous missions. In the case of a single fly-by, the performance can be expressed in terms of altitude and relative velocity [9]. Regarding the orbital control, such a mission would be similar to the cruise context introduced in section I.2, particularly because the relative velocities for an asteroid fly-by are usually higher than $10\,\mathrm{km\,s^{-1}}$, meaning that no deceleration can be expected from a CubeSat.

The team of BIRDY-T assumes that the CubeSat will be released near a small asteroid, after the mothercraft has performed the rendezvous. This is based on the ongoing proposal from ESA for the Hera mission [20], targeting the binary system 65803 Didymos, made of two asteroids nicknamed Didymain and Didymoon. Another mission, this time from NASA, targets this NEA: Double Asteroid Redirection Test (DART). Together, those two missions constitute the Asteroid Impact and Deflection Mission (AIDA). AIDA aims to perform an asteroid deflection test by means of a kinetic impactor (DART) and to investigate the changes in geophysical and dynamic properties of the system of asteroids after the impact. This joint mission is expected to provide numerous information, specifically about asteroid deflection for Earth protection. Two 6U CubeSats will be carried with Hera and released in situ. Although no radio science is currently planned with the CubeSats, the addition of a USO on-board Hera would enable two-way radio signals with the CubeSats, as well as with ground stations.

For the moment, a radio science experiment is proposed with the instrument RSE [21]. It is expected to provide, together with imagery, the mass of Didymoon with a 1.6 % accuracy. This is where the low cost of a CubeSat comes into play, by allowing a riskier approach to the binary system compared to the mothercraft. Hence, an accuracy of 1 % can be obtained with very slow overflights at low altitudes from a CubeSat, together with the determination of the gravity field with several spherical harmonics [9].

Hereafter, we will commit ourselves to a radio science mission with a CubeSat around Didymos, that we will sometimes refer to as proximity operations. Although the binary system has a semi-major axis of approximately 1.64 au [22], its highly elliptical orbit ($e \simeq 0.38$) means the distance to the Sun varies along the orbit from 1.02 UA to 2.26 UA. The distance between the two asteroids is (1180^{+40}_{-20} m) and the orbital period is ($11.920^{+0.004}_{-0.006}$ h). The total mass of the system (mainly due to Didymain) is estimated to be $5.28 \pm 0.54 \times 10^{11}$ kg. The diameter and density of Didymain are 780 m($\pm$10%) and 2.1($\pm$30%) respectively. When it comes to Didymoon, its diameter is estimated to be 163 ± 18 m. The aim of the mission is to determine its mass with a precision better than 10 %, and its density (expected to be in the range from 1 to 2.1) with a precision better than 20 %.

In the configuration of the binary system, it has been shown that stable orbits associated with resonances or located at the Lagrangian points exist [23]. Although the former provide long arc motions, they remain situated in a small range of inclina-

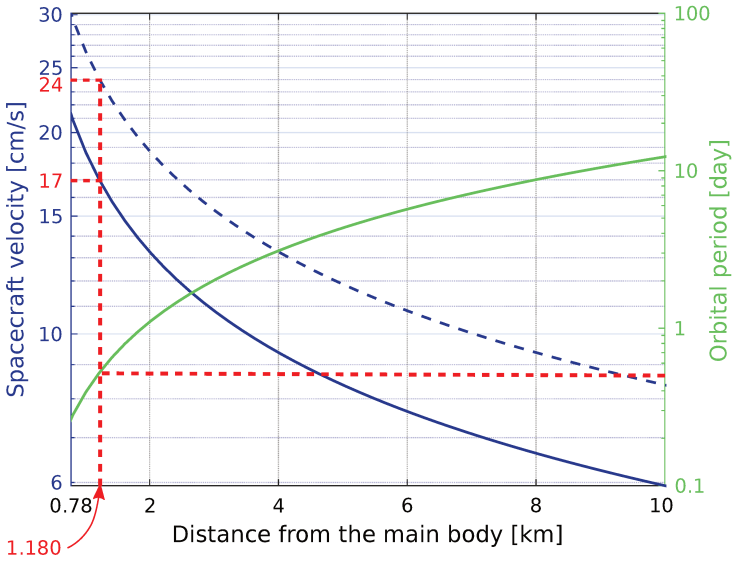

Figure I.8: Velocity and orbital period around Didymos. Spacecraft velocities are in blue, and the orbital period is in green. The solid line indicates the minimum velocity to remain in orbit while the dashed line represents the escape velocity (the concept of orbital period does not make sense for a spacecraft traveling at the escape velocity). Red marks highlight those parameters at the distance of Didymoon.

tions and distances from the central body and require very small relative velocities, of the order of few dozens of $\mathrm{cm\,s^{-1}}$. For instance, the linear velocity of Didymoon orbiting Didymain is $\sim 17\,\mathrm{cm\,s^{-1}}$. I draw the orbital and escape velocities as a function of the distance to Didymain in figure I.8 to highlight that the slightest excess in orbital velocity would result in the CubeSat escaping the binary system. Needless to say, orbiting Didymoon would be even harder considering its very low mass. In any case, such orbits are not recommended for planetary geodesy. We are more interested in "3D" motion arcs at various distances from the investigated object because they facilitate estimates for orbit and gravity field parameters. As previously mentioned, the concept of operation is based on alternating hyperbolic arcs in free-fall conditions and Trajectory Correction Maneuvers (TCMs). The hyperbolic arcs should be traveled at about $1\,\mathrm{m\,s^{-1}}$ of relative velocity. Because the hill sphere radius of the binary system is approximately 70 km (calculated from the data provided earlier in this section), the operation concept suggests hyperbolic arcs to last roughly one day ($\sim 86\,\mathrm{km}$).

The requirements over the Guidance Navigation & Control (GNC) are related to the need of autonomy and the uncertainty about the local environment. Moreover, the knowledge of the orbital position coming from the IFOD will include an uncertainty that still has to be assessed in this context of proximity operations. Hence, we will be looking for robust and safe TCMs, maximizing the CubeSat autonomy. As a first optimistic approximation, we anticipate each TCM to use $2\,\mathrm{m\,s^{-1}}$ of ΔV. The total budget of ΔV will linearly depend on the number of hyperbolic arcs that the science case requires. Conversely, the number of scientific measurements may be limited by the lifetime of the on-board propulsion.

CHAPTER II

CubeSats with Propulsion

Now that CubeSats have become very popular, one of the most important next technical frontiers is orbital control. Propulsion is meant to enable new orbits for CubeSats and a variety of novel applications. We review some of those orbits and applications, before dealing with parameters used to evaluate the performance of propulsion systems. Finally, we present our state of the art of CubeSat propulsion.

II.1 - New Applications for CubeSats

Orbital control has been a priority for mission planners since the beginning of the space area. To that end, various propulsion systems were developed, and the first electric propulsion (a Pulsed Plasma Thruster) flew in 1964 [24]. Numerous missions have successfully used propulsion since then, both chemical and electric, showing the maturity of these techniques. With the current miniaturization trend, the challenge is to design thrusters that can adapt to extremely constrained formats, as will be seen in section II.3.

When talking about space propulsion, one must separate propulsion for launchers and for satellites. On the one hand, launchers propulsion is responsible for putting satellites in orbit, which means they need to provide velocity increments (ΔV) of about $7\,\mathrm{km\,s^{-1}}$ to $15\,\mathrm{km\,s^{-1}}$ and very high thrust levels. It is achieved by very powerful chemical thrusters that have a small airlift capability. Orbital propulsion on-board satellites takes action once the main transfer has been performed by the launcher.

Orbital control is intended to increase the lifetime of satellites by enabling drag compensation [25], provide deorbiting capabilities [26], allow formation flying constellation management [27, 28] and attain new orbits, around the Earth or beyond [29, 30]. To that end, many subsystems have been developed, especially propulsion systems based on various technologies [24, 31].

One can see that historically, CubeSats have been launched in Earth orbits, especially in Low Earth Orbit (LEO). This is due to their low telecommunication capabilities, and it was probably encouraged by the frequency of available rideshares to these orbits. A LEO is an Earth-centered orbit with an altitude of less than

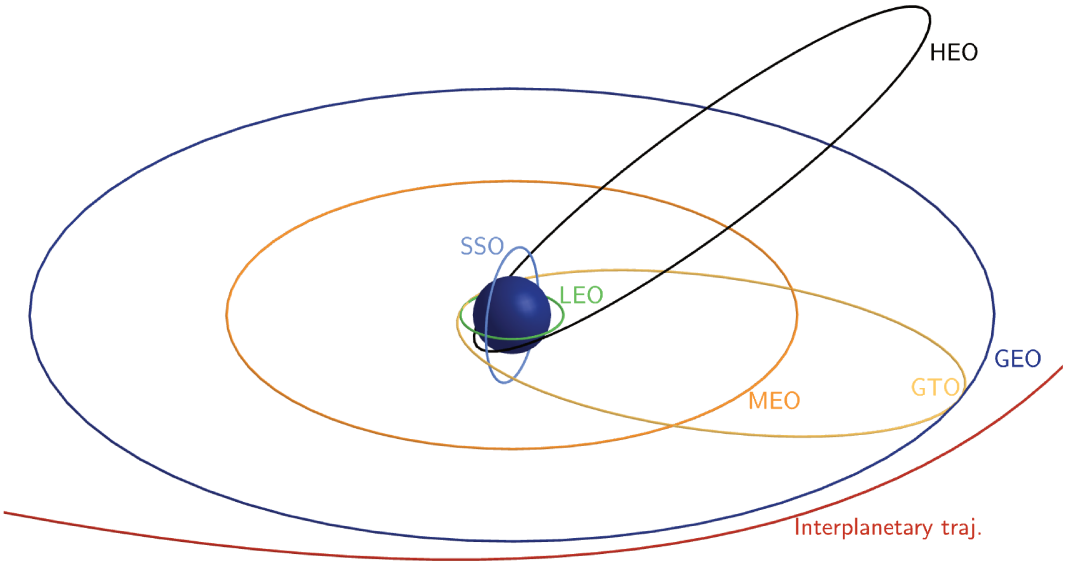

Figure II.1: Scaled drawing of main Earth orbits. A low Earth orbit (LEO) is in green, a Sun-synchronous orbit (SSO) in light blue, a medium Earth orbit (MEO) in orange, a highly elliptical orbit (HEO) in black, a geostationary orbit (GEO) in dark blue and a geostationary transfer orbit (GTO) in yellow. An example of interplanetary orbit is also plotted in red. Very low Earth orbits do not appear for clarity reasons.

2,000 km, provided that its eccentricity is below 0.25. They are the most populated orbits, allowing Earth observation, telecommunication, remote sensing or scientific missions. As a result, the LEO environment is becoming congested by both operational satellites and debris.

The majority of CubeSats was sent to altitudes lower than 650 km, hence dodging their main limitation: the lack of active deorbiting capabilities. Indeed, the only force that remains to deorbit a propulsion-less spacecraft in a tangible way is the atmospheric drag, which is considered to be too weak at high altitudes to respect the 25-year regulation[1]. At the moment, this regulation is enforced in France under the name "Loi sur les Opérations Spatiales" (LOS) [32], and applicable to all ESA missions[2]. Therefore, CubeSat propulsion enables deorbiting maneuvers from LEO higher than 650 km, ensuring that the decay respects the 25-year regulation, and preventing the growth of debris population. Telecommunication constellations and Earth observation missions may want larger downlink and coverage permitted by higher altitudes [33]. Astronomy constellations may also be interested in such orbits, as evidenced by the two 7 kg nanosatellites of the BRITE (BRIght-star Target Explorer) constellation [34] deployed in 2013 by the Indian Polar Satellite Launch Vehicle (PSLV) (four nanosatellites were deployed in total). Higher orbits have also become a reality, such as Medium Earth Orbit (MEO) or Geostationary Earth Orbit (GEO) [35] (see figure II.1). In figure II.1, I display the principal Earth orbits.

[1] In order to remove mass from densely populated orbits, satellites and orbital stages must reenter Earth's atmosphere within 25 years of mission completion, if their deployment orbit altitude is below 2,000 km (in the LEO region).

[2] ISO 24113:2019 — Space systems — Space debris mitigation requirements.

In addition, the emergence of propulsion systems for CubeSats will open up Very Low Earth Orbits (VLEO) - featuring an altitude between 250 km and 500 km - to nanosatellites requiring relatively long mission duration [25]. Such orbits are of interest because the size and power of optical and radar instruments scale with the orbital altitude for a given instrument performance. Very low altitudes hence offer more performance and lower costs for small platforms like CubeSats. However, spacecrafts in VLEO have to face high levels of atmospheric drag. It results in highly perturbed orbits and even in fast orbital decay. As an example, the 6 kg Dove-1 spacecraft of Planet Labs [36], released on a 250 km orbit, reentered the atmosphere in only six days. The emergence of propulsion systems will enable drag compensation, hence granting CubeSats access to VLEO for mission requiring longer duration. For instance, it is expected that the PPTCUP propulsion system developed by Clyde Space Ltd [37] increases the lifetime of a 3U CubeSat on a 250 km altitude orbit by 66 % (and 50 % at 350 km).

Furthermore, CubeSats and nanosatellites in general are attractive solutions for constellations of satellites flying in formation. A review focused on nanosatellites is available in [38]. Satellites flying in formation are characterized by at least one satellite which must track the state of another satellite. The CanX-4&5 performed formation flying from 1,000 m to 50 m separation using cold gas propulsion [28]. With regard to constellations, satellites in actively controlled ones must ensure that they follow a pre-defined trajectory. A good example is the Flock constellation from Planet Labs dedicated to Earth imagery [39]. The case of uncontrolled constellation missions is not relevant to this work, because no active orbital control is required. Constellations increase the temporal frequency of revisiting for Earth observation or remote sensing applications.

Scientists are also interested in distributed architecture, enabling new concepts of instruments. One example using traditional spacecrafts is the LISA mission for gravitational wave detection developed by ESA [40]. NOIRE is an undergoing study focused on the use of a low-frequency radio interferometer made of a swarm of nanosatellites [41]. Such applications will require to maintain a relative positioning between all the members of the constellation, hence necessitating propulsion. In order to reduce the deployment cost, orbital capabilities may also be used to deploy a constellation from the same shared launch [42].

Interestingly, some interplanetary spacecrafts are among the constellations and formation-flying satellite missions that we have mentioned. In fact, interplanetary CubeSats are on the rise. The two MarCO CubeSats [1], launched in 2018 with Insight, successfully performed their Mars fly-by using Cold Gas Thruster (CGT). The Inspire mission [43], aiming to place nanosatellites in Earth-escape orbit, is still waiting for a launch date. The Exploration Mission 1 (EM-1), first flight of the Space Launch System scheduled for 2020, will carry 13 nanosatellites and release them on a trajectory to the moon (we can cite EQUULEUS [44], Lunar Flashlight [45] and NEAScout [46]. Although some interplanetary launch opportunities exist, such as Insight or AIDA [47], most common CubeSat rideshares are in LEO. However, reaching interplanetary orbits from LEO with current propulsion systems for nanosatellites looks very unlikely [30]. With the numerous launchers providing Geostationary Transfer Orbits (GTOs), one can assume that rideshares to such orbits will become more common for CubeSats planning to go to interplanetary orbits [48].

Table II.1: Typical ΔV requirements associated with space maneuvers. Inspired by Erichsen [49].

Maneuver	$\Delta V\,[\mathrm{m\,s^{-1}}]$	Remarks
Kourou (French Guyana) → LEO	9,300	Equatorial
Kourou (French Guyana) → GEO	11,400	
Cape Canaveral (USA) → LEO	9,500	Equatorial
Cape Canaveral (USA) → GEO	13,600	
LEO → GEO	4,300	Equatorial
LEO → Moon	5,900	Equatorial
Drag compensation 400 km to 500 km LEO	25	ΔV per year
Drag compensation 500 km to 600 km LEO	5	ΔV per year
Station keeping in GEO	50	ΔV per year

We list the velocity increments required to perform several space maneuvers in table II.1. Orbital maneuvers necessitating several kilometers of ΔV are most likely unfeasible with CubeSats, although some electric propulsion developments are trying to bridge the gap between orbital maintenance and orbit transfers (see section II.3).

II.2 - Conventional Approach to Propulsion Systems

In this section, I review the common approach to propulsion systems. Actually, it is important to note that two main types of orbital actuators must be distinguished: reaction jets, which produce a control force by the expenditure of mass, and propellant-less devices, among which are solar sails and electrodynamic tethers - although the tethers are abusively considered as propellant-less, as we will see. Regarding these last two techniques, we will limit ourselves to a light introduction because they are still in their early phases of demonstration. Then, this work mainly focuses on the challenges associated with the use of reaction jets.

II.2.1 - Propellant-less Propulsion Systems

Electrodynamic Tethers

Electrodynamic tethers generate thrust through Lorentz force interaction with an ambient magnetic field. These are conductive wires, extending from a spacecraft, that carry a current to generate either thrust or drag, using the planetary magnetic field. The abusive thought that electrodynamic tethers are propellant-less resides in the way electrons collected passively at one extremity of the tether are actively emitted at the other extremity. This active emission is indeed required to obtain

an efficient propulsion [50], and most of the time it relies on hollow cathodes fueled with Xenon or Argon (about 1 kg/A/yr).

The gravity gradient (see section IV.1.4.1) tends to direct the tether along the vertical direction (nadir). The motion of the orbiting conductor across the ambient magnetic field induces an electromotive force called EMF along the tether. The Faradays' law of induction describes this phenomenon:

$$V_{EMF} = \int_0^L \mathbf{v}_{orb} \times \mathbf{B}\ d\mathbf{L}\ [\mathrm{V}]. \tag{II.1}$$

This voltage can be up to several hundred volts per kilometer within the Earth magnetic field. The motional EMF will drive a current along the tether. In accordance with the Lorentz force equation, a force can be generated if a current flows in the tether element:

$$\mathbf{F} = \int_0^L I\ d\mathbf{L} \times \mathbf{B}\ [\mathrm{N}]. \tag{II.2}$$

The tether can be used in two modes:

- In self-powered mode, the tether can be used to reduce the orbit of the spacecraft to which it is attached (de-boost). The system will collect electrons from the conducting ionospheric plasma at one end of the tether, and expel them back into the plasma at the other end. A Lorentz force is thereby created, opposing the motion of the tether-satellite system.
- In boost mode, on-board power supplies must overcome the motional EMF to drive current in the opposite direction, inducing a force in the same direction as the motion of the tether-satellite system.

Tethers Limited[3] developed the µPET, an electromagnetic tether capable of raising the orbit of a 125 kg spacecraft from 350 km to 700 km in 50 days.

Solar Sails

Solar sails are another growing alternative to reaction jets. They use the pressure exerted by the solar radiation on a sail due to reflection and a small fraction of absorption. An overall efficiency of 90 % can be found in the literature [51], leading to about 8.17 µN/m^2 in the direction normal to the surface and at a distance of 1 au from the Sun. For an ideal sail, the expression of the force is

$$F = \frac{F_0 \cos^2 \theta}{R^2}\ [\mathrm{N/m^2}], \tag{II.3}$$

where R is the distance from the Sun in astronomical unit (au), θ is the angle of incidence and F_0 is the reference at 1 au. CubeSats have already been launched with solar sails, which employ a thin reflective sheet that can be folded into a cube unit before being spread out in orbit. The Planetary Society's LightSail-1 [52], a 3U CubeSat, was launched from Florida. Its four sails, made of very thin Mylar, have a total area of 32 m^2.

[3] http://www.tethers.com/microPET.html

II.2.2 - Focus on Reaction Jets

Going back to our central focus, we now define the main performance parameters that are used for any reaction jet.

Let us begin with the thrust vector. Contrary to propulsion systems on-board aircraft, pressure effects do not come into play for space propulsion. As a result, the thrust vector directly relates to the expelled propellant by

$$\mathbf{F} = -\dot{m}_p \mathbf{v}_e \ [\mathrm{N}], \tag{II.4}$$

where $\dot{m}_p$ is the ejected propellant mass flow and $\mathbf{v}_e$ is the exhaust velocity vector. The thrust level F governs the duration of a maneuver and its precision: the higher the thrust is, the shorter the maneuver duration is and the less accurate it is. Another essential characteristic of reaction jets is the incremental velocity budget (ΔV), which conveys the amount of maneuver the propulsion system can provide. It is expressed by the Tsiolkovski equation

$$\Delta V = -v_e \ln\left(\frac{m_f}{m_0}\right) \ [\mathrm{m\,s^{-1}}], \tag{II.5}$$

where m_0 is the initial mass of the spacecraft, $m_f = m_0 - m_p$ is the mass of the spacecraft at the end of the maneuver and m_p is the propellant mass consumed. The ΔV depends both on the performance of the propulsion device (exhaust velocity) and the quantity of propellant on-board, but also on the spacecraft mass ratio.

The total impulse (I_{tot}) is introduced to allow propulsion devices comparison without considering the satellite. It is defined as the impulse that a thruster can provide during its operational lifetime τ, which is equivalent to consuming all the propellant available on-board the spacecraft $m_{p,max}$:

$$I_{tot} = \int_0^\tau F dt = v_e m_{p,max} \ [\mathrm{N\,s}]. \tag{II.6}$$

The total impulse relates to the operational lifetime of a propulsion system.

Thrust and total impulse are intrinsic parameters describing the performance of a propulsion system. For the same thruster, there may be several sets of (F, I_{tot}) at which it can operate. Such sets are called operating points. However, we are still lacking a relevant criterion to discriminate between propulsion systems, since the total impulse varies linearly with the total mass of propellant on-board.

Therefore, propulsion designers work with a more intrinsic parameter called the specific impulse (I_{sp})

$$I_{sp} = \frac{I_{tot}}{m_{p,max} g_0} = \frac{F}{\dot{m}_p g_0} \ [\mathrm{s}], \tag{II.7}$$

where $g_0 = 9.80665 \ \mathrm{m\,s^{-2}}$ is the standard gravity field. Thus defined, the specific impulse corresponds to the impulse delivered per unit weight of propellant at sea level[4]. A high I_{sp} means that the propulsion system has a good efficiency in terms

[4] Another definition of the specific impulse is available in the literature: $I_{sp} = \frac{I_{tot}}{m_{p,max}} = \frac{F}{\dot{m}_p}$ $[\mathrm{N\,s\,kg^{-1}}]$

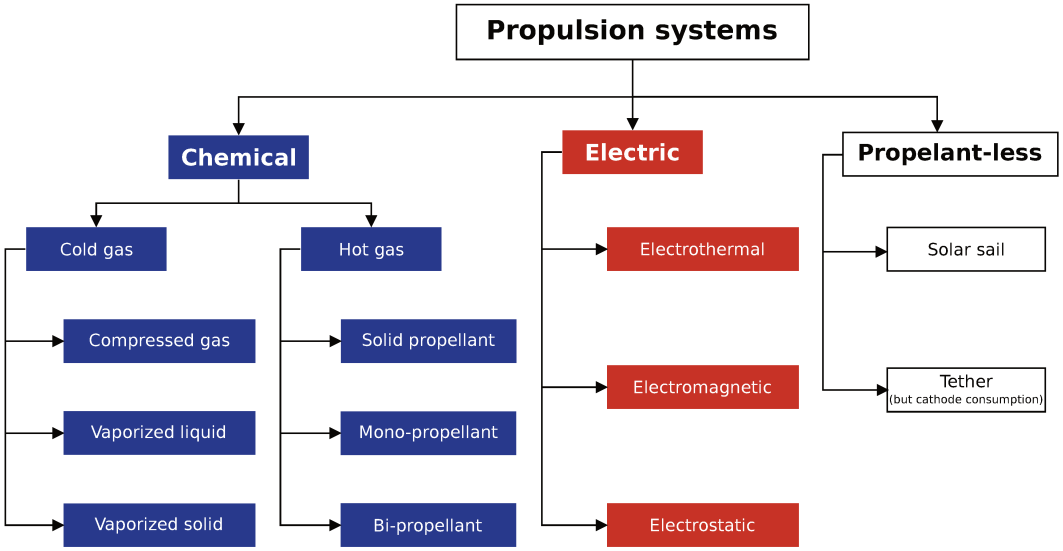

Figure II.2: Types of spacecraft propulsion systems.

of propellant consumption. At similar fuel mass, a system with a higher I_{sp} will provide the satellite with more ΔV.

Rewriting the Tsiolkovsky equation, one can now compute the amount of propellant required to perform a certain maneuver with a propulsion device of given I_{sp}

$$m_p = m_0 \left(1 - e^{-\frac{\Delta V}{I_{sp} g_0}}\right). \tag{II.8}$$

At thruster level, the thrust along with the mass flow rate are the main data for evaluating its performance, because most of the time they can both be measured experimentally. In the traditional approach, the specific impulse (ratio of the two previous measured data) is the most popularly used criterion.

II.3 - State of the Art of Reaction Jets for CubeSats

The most common way of classifying reaction jets is from their source of energy, specifically their dependence on the on-board power. Hence, the two main categories are electric and chemical (non-electric) systems, as depicted in figure II.2. In this section, we present the principles of the different propulsion techniques and we identify thrusters compatible with CubeSats.

At this point, it is important that we introduce a concept central in the rest of this work: the Unified Propulsion System (UPS). A UPS is defined as a system compatible with the use of a common tank to feed several thrusters. Because accommodating several actuators is often very tricky at the nanosatellite scale, a thruster capable of providing both attitude and orbit control is promising. To do so,

it requires a certain number of thrust directions. Specifically, $n + 1$ thrust vectors are necessary to control n degrees of freedom [53]. This immediately translates into the same number of thruster nozzles, which can be either fed separately (one independent propulsion device per thrust vector), or by a common tank, thus reducing drastically the required mass. As we will see in this section, many propellants prevent from using a single tank when multiple thrusters are required, which is a major drawback.

II.3.1 - Chemical Propulsion

Chemical propulsion uses gases at high pressure and/or temperature that are accelerated through a nozzle at high velocity to produce thrust force. Chemical propulsion systems are usually associated with lower specific impulse than electric propulsion systems, but higher thrust to power ratios.

II.3.1.1 - Cold Gas Thrusters

Cold Gas Thruster (CGT) is a type of propulsion system in which the propellant does not undergo combustion or electromagnetic acceleration. Different variants exist.

Compressed Gas

Compressed gas thrusters are the simplest CGTs. The propellant is held under pressure in the thruster and released through a nozzle to generate thrust. Although such thrusters have a very straightforward and reliable design, they suffer from very poor performances. Because the produced thrust depends on the pressure of the propellant, it decreases during the thruster lifetime. The MEMS propulsion module from NanoSpace was designed to perform the orbit control of the 2U Estelle CubeSat from the QB50 project[5] using butane [54].

Vaporizing Liquid

Vaporizing liquid thrusters utilize the high vapor pressure of liquid propellants. Expansion causes their phase transfer into gas. More propellant can be stored in the same volume compared to compressed gas, but it comes at the cost of an increased complexity with the use of a vaporizer. The JPL MarCO Micro Propulsion System from VACCO (see figure II.3), fueled with a two-phase propellant, was used on-board the twin-communication-relay CubeSats on their way to Mars [55, 8]. It must be said that the system from VACCO requires a warm-up phase that highly increases the power consumption (50 W), which is usually below 10 W for CGTs.

Vaporizing Solid

Vaporizing solid thrusters push the logic even further with the use of gas produced from a solid charge by ignition. The gas is then stored and released the same way as for compressed gas thrusters.

[5] https://www.qb50.eu/

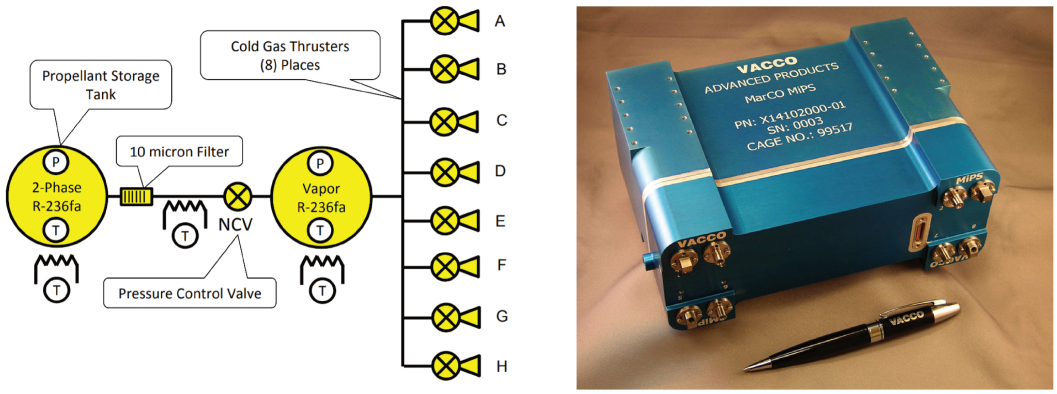

Figure II.3: JPL-MarCO MiPS schematic (left) and system (right). Credit: VACCO [55].

Table II.2: Performance of identified Cold Gas Thrusters (CGTs).

Model	Mass [kg]	Power [W]	Thrust [mN]	I_{tot} [N s]	I_{sp} [s]
MEMS [54, 56]	0.280	2	1	40	68
NanoProp 3U [57]	0.350	2	1	40	60
NanoProp 6U [57]	0.900	2	5	80	60
JPL MarCO MPS [55, 8]	3.490	55	25	755	40
NEA Scout MiPS [58]	2.543	55	23	500	40
CuSP [59]	0.690	12	25	60	40
ACS [60]	1.090	5.4	60	115	65
CNAPS [61, 28]	1.890	0.3	31.3	115	45
MEPSI MiPS [62, 63]	0.986	1	53	23	44
MiPS Standard [64]	0.542	10	10	44	40
MiPS end-mounted [65]	0.676	10	10	93	40
C-POD [66, 67]	1.244	5	25	186	40
Palomar [68]	1.063	5	35	85	50

CGTs present many benefits for their integration on CubeSats. Because of their straightforward design, a single propellant tank can easily feed several thrusters, thus enabling orbit or attitude control capabilities. For instance, VACCO designed the ACS to provide attitude control to the Interplanetary NanoSpacecraft Pathfinder In Relevant Environment mission (NASA). A more extensive list of CGTs is available in table II.2.

II.3.1.2 - Hot Gas Thrusters

By contrast to CGTs, we will call other types of chemical propulsion "hot gas". Hot gas propulsion systems comprise liquid or solid propellants. An exothermal combustion reaction of the propellant is needed to produce high temperature products that are expelled. Solid rocket propulsion systems provide high density levels of energy essential for rockets. Their main drawback comes from their lack of restartability. Contrary to solid propulsion systems, liquid ones can be restarted, making them more interesting for spacecraft propulsion. Liquid propellants are either mono- or bi-propellant.

Liquid Mono-Propellant

Liquid mono-propellant systems are based on the decomposition, thanks to a catalyst, of their single propellant. They require more power than CGTs because of the engine preheating. Historically, hydrazine has been the conventional rocket fuel for attitude control, resulting in a strong flight heritage interesting for CubeSats. The MPS-120 from Aerojet Rocketdyne is an example of hydrazine propulsion system slightly bigger than 1U that provides attitude and orbit control capabilities for a total ΔV budget of $209\,\mathrm{m\,s^{-1}}$ [69, 70]. However, manipulating hydrazine requires rigorous protocols because of its high toxicity, and it must be kept warm (giving rise to heating cost). Salts derived from nitric acid, such as ADN (ammonium dinitramide, $NH_4N(NO_2)_2$), HAN (hydroxylammonium nitrate, NH_3OHNO_3) or AN (ammonium nitrate, NH_4NO_3)) reduce the toxic handling concern associated with hydrazine. They are also cheaper and somewhat more efficient than hydrazine. Many propulsion designers develop propulsion systems working with these "green" propellants, but they must face technical challenges such as higher power consumption and combustion temperatures. A 1U propulsion system fueled by a green ADN-based propellant, the Green Chemical Propulsion System from NanoAvionics [8], displayed in figure II.4 was demonstrated in-orbit as part of the QB50 project. VACCO is developing several green mono-propellant thrusters for CubeSats that will go to the moon with EM-1.

Liquid Bi-Propellant

A bi-propellant system comprises a fuel and an oxidizer. The two propellants are self-ignited in a combustion chamber before being expelled. Such systems provide rather high ΔV that were historically required for operations such as orbit-rising. Hyperion Technologies developed two bi-propellant systems, the PM400 [71, 72] and PM200 [73] (see figure II.5), for 3U and 6U CubeSats respectively.

Performance of identified liquid mono- and bi-propellant thrusters is displayed in table II.3.

Solid Motor Rocket

Similarly to bi-propellant systems, solid propulsion systems use an oxidizer and a fuel. Here, both fuel and oxidizer are located in the combustion chamber in solid form. Most of the time, all the propellant must be used at once, producing a very high thrust hard to control on small platforms. D-Orbit has developed the D3 Decommissioning device that flew on-board the 3U D-Sat in 2017 [84] (see figure

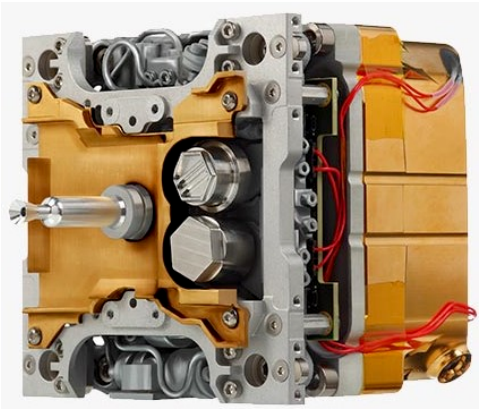

Figure II.4: EPSS — Green Chemical Propulsion System. Credit: NanoAvionics [74].

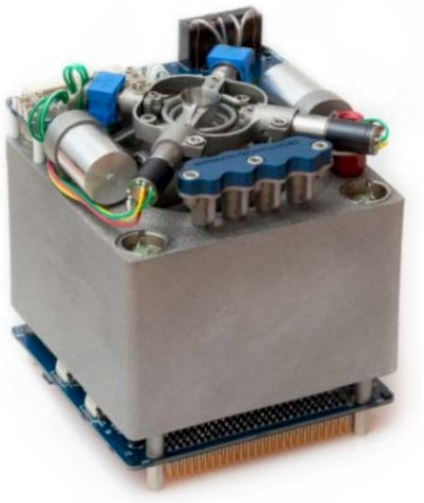

Figure II.5: PM-200 propulsion system. Credit: Hyperion Technologies [73].

Table II.3: Performance of identified mono/bi-propellant thrusters.

Model	Mass [kg]	Power [W]	Thrust [N]	I_{tot} [N s]	I_{sp} [s]
MPS-120 [69, 70]	1.480	10	1	775	210
BGT-X5 [75, 76]	1.5	20	0.5	565	220
ADN MiPS [77]	1.797	15	0.1	1,036	200
ArgoMoon PS [78, 79]	2.065	20	0.1	783	190
Lunar Flashlight PS [80]	5	35	0.15	3,320	169
EPSS [74]	1.2	8	0.1	650	200
MPS-130 [69, 81]	1.660	25	0.75	1,200	244
PM400 [73]	2.025	6	1	1,750	285
PM200 [71, 72]	1.410	6	0.5	850	285
HYDROS-C [82, 83]	2.640	25	1.2	2,252	310

II.6). We will see later on that the demonstration of this propulsion system was a limited success because of a misalignment of the motor. Although sufficient data about this propulsion device was not found, the performance of other identified solid rocket devices is available in table II.4.

II.3.2 - Electric Propulsion

In chemical propulsion, the only way to increase the output power is to increase either the chemical energy or the flow rate of the propellant. Electric propulsion bypasses this fundamental limitation by using electric or electromagnetic energy to eject matter at higher velocities. To be more specific, an external electric power

Figure II.6: D3 Decommissioning device. Credit: D-Orbit [84].

Table II.4: Performance of solid motor rocket systems.

Model	Mass [kg]	Power [W]	Thrust [N]	I_{tot} [N s]	I_{sp} [s]
30 sec. Motor [85]	1.49	N/A	37	997	187
ATK STAR 4G [85]	2.48	N/A	258	2,657	277
CAPS-3 [8]	2.33	2.3	0.3	N/A	300

accelerates the propellant to produce useful thrust. These higher ejection velocities immediately translate into higher efficiency of the propellant (less propellant needed for the same ΔV as a chemical propulsion), but at the cost of the added power supply. Figure II.7 depicts the differences between chemical and electric propulsion. Three main methods of converting the electrical energy exist.

II.3.2.1 - Electrothermal Propulsion

Electrothermal propulsion can be seen as a first step towards the improvement of CGTs. In order to energize a gaseous propellant, the gas passes over an electrically heated surface (resistojets) or through an arc discharge (arcjets), thus increasing the exhaust velocity. Then, the heated gas is accelerated by gas-dynamic expansion, similarly to CGTs. Resistojets are somewhat popular for CubeSat applications (see table II.5). We also include an electrothermal radio frequency thruster designed by Phase Four (see table II.6), where an ambipolar mechanism is used for ion accelerations [86, 87]. Its classification as electrothermal comes from [88].

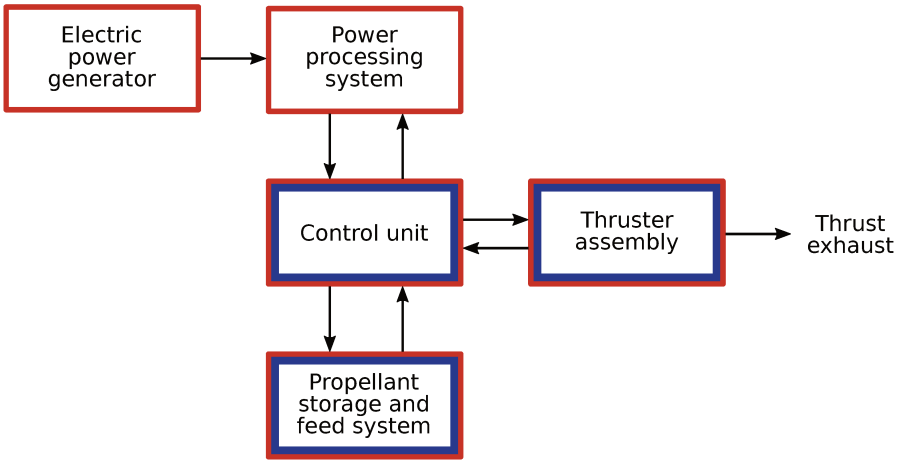

Figure II.7: Schematic of chemical (in blue) and electric propulsion (in red).

Table II.5: Performance of resistojets and arcjets.

Model	Mass [kg]	Power [W]	Thrust [mN]	I_{tot} [N s]	I_{sp} [s]
XR-50-050 [89, 90]	0.470	50	150	120	49
VHTR [25, 91]	0.5	100	100	246	100
MRT [92]	1.250	15	10	404	150
PUC 0.25U [93, 94]	0.718	15	5	184	70
PUC 0.5U [93, 94]	0.980	15	5	320	70
PUC 1U [93, 94]	1.5	15	5	593	70
MVP [95]	1.2	35	6.7	540	83

Table II.6: Performance of electrothermal Radio Frequency (RF) thrusters.

Model	Mass [kg]	Power [W]	Thrust [µN]	I_{tot} [N s]	I_{sp} [s]
RFT [86, 87]	1.5	50	640	120	589

II.3.2.2 - Electromagnetic Propulsion

Electromagnetic propulsion systems convert gas into plasma, an ionized state of matter made of neutral particles, positive ions and negative electrons, and which can be considered globally neutral. The resulting plasma is then expelled at high velocity by the interaction of the discharge current with the electromagnetic field. If the acceleration is either caused by the Lorentz force or by the effect of an electromagnetic field where the electric field is not in the direction of the acceleration, the device is considered electromagnetic. At the difference of many electrostatic thrusters, the neutral plume of electromagnetic systems has the advantage of not requiring a neutralizer (see section II.3.2.3). Hereafter, I introduce Pulsed Plasma Thrusters (PPTs) and Vacuum Arc Thrusters (VATs) (see data in table II.7).

Table II.7: Performance of Pulsed Plasma and Vacuum Arc Thrusters (Pulsed Plasma Thrusters (PPTs) and Vacuum Arc Thrusters (VATs)).

Model	Mass [kg]	Power [W]	Thrust [µN]	I_{tot} [N s]	I_{sp} [s]
PPTCUP [37, 96]	0.286	2	40	40	670
NanoPPT [97]	0.350	5	90	190	640
BmP-220 [98]	0.5	7.5	20	220	536
L-µPPT [99, 100]	0.750	3	120	785	1,000
µCAT [101, 102]	0.240	2.5	50	1,180	3,000
Plasma Jet Pack [103]	0.800	30	45	4,000	5,000

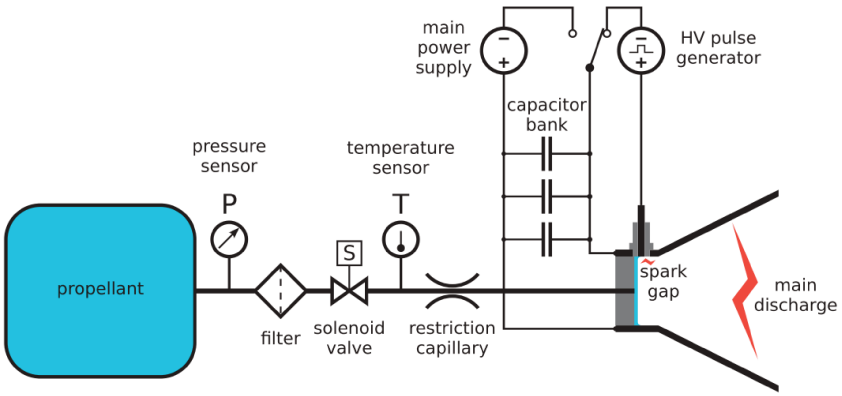

Figure II.8: Schematic of the L-µPPT [100].

Pulsed Plasma Thrusters

In a Pulsed Plasma Thruster (PPT), a pulsed, high current discharge ionizes a propellant. The resulting plasma is accelerated through a Lorenz force created by the interaction between the discharge current and the self-induced magnetic field. The propellant is usually a solid bar of teflon (PTFE) fed between two electrodes. The Pulsed Plasma Thruster for CubeSat Propulsion (PPTCUP) from Mars Space Ltd. and Clyde Space was successfully qualified up to Technology Readiness Level (TRL) 8. Although solid PPTs are robust electric systems, they suffer from low propellant utilization because of their self-regulated feeding system and inconsistent thrust levels due to the inhomogeneous ablation of the teflon bar. PPTs working with liquid or gaseous propellant have been considered, and the L-µPPT system (TRL 3) is an example of the benefits coming from using a liquid teflon oil [99, 100] (see figure II.8).

Vacuum Arc Thrusters

Vacuum Arc Thruster (VAT) is another type of plasma-based propulsion device that produces thrust by propellant ionization. This technology consists of two metallic electrodes separated by a dielectric insulator. One of them is used as solid metallic propellant and is consumed as the thruster operates. Compared to PPTs, VATs present some advantages such as a simpler design, a lower mass, or a higher

Table II.8: Performance of ion thrusters.

Model	Mass [kg]	Power [W]	Thrust [mN]	I_{tot} [N s]	I_{sp} [s]
RIT-µX [108, 109]	0.540	50	0.3	1,964	2,000
BIT-3 [105, 106, 107]	2.9	56	1.2	33,879	2,300

efficiency, but also some major drawbacks as a non-adjustable thrust level and a strong dependency on the thruster electrodes. George Washington University is developing the µCAT [101, 102], a VAT selected by NASA AIMS Research Center in December 2012 that flew in May 2015 on-board the Ballistically Reinforced Communication Satellite (BRICSat-P) [104]. By detumbling the CubeSat (from $30\,^\circ\,s^{-1}$ to $1.5\,^\circ\,s^{-1}$) and providing the target rotation rate of $1\,^\circ\,s^{-1}$, the system has reached TRL 7.

II.3.2.3 - Electrostatic Propulsion

Electrostatic propulsion devices work with a high molecular density propellant that can be ionized in different ways (by electron bombardment, in a high frequency electromagnetic field or by extracting ions from the surface of a liquid metal under the effect of a strong electrostatic field). If the acceleration is caused mainly by the application of a static electric field in the direction of the acceleration (Coulomb force), the device is considered electrostatic. Such systems often require a cathode to emit electrons that will neutralize the exhaust plume, hence preventing the accumulation of charged particles on the external surface of the satellite. This complicates the scale down for CubeSats.

Ion Thrusters

In an ion thruster, the propellant is ionized by using various plasma generation techniques. Usually, a propellant, such as xenon gas, is ionized by electron bombardment (Kaufman) or in a high-frequency electromagnetic field (Radio Frequency (RF)). The ions are then accelerated at very high exhaust velocities by electrostatic grids. The acceleration voltage is applied between a set of consecutive grids terminating the plasma source. These devices have a high efficiency when compared to other electric propulsion systems. In addition, the absence of electrodes in RF thrusters avoids potential threats to thruster lifetime which is only limited by grid erosion. A main drawback is related to the ionized propellant (the plume) that is expelled by ion thrusters. An external cathode emits electrons to neutralize the plume. Busek develops the iodine-fueled BIT-3 [105, 106] that is scheduled for launch on two deep space 6U CubeSats in 2020 [107]. The 3 kg wet mass and the 56 W to 80 W of power required will impose drastic constraints to the two CubeSats. I gather identified ion thrusters in table II.8.

Table II.9: Performance of Hall Effect Thrusters (HETs).

Model	Mass [kg]	Power [W]	Thrust [mN]	I_{tot} [N s]	I_{sp} [s]
HT-100 [113]	0.7	120	6	2,455	1,000
BHT-200 [114]	1.450	200	13	3,376	1,375
HET-70 [25]	> 0.9	77	3.5	N/A	1,000
ExoMG-nano [115, 33]	1.287	40	1.5	3,382	1,200

Hall Effect Thrusters

Based on the Hall Effect [110], a Hall Effect Thruster (HET) utilizes mutually perpendicular electric and magnetic fields to accelerate the previously ionized propellant. The grids used in ion thrusters to accelerate the ions are here replaced by a strong magnetic field perpendicular to the ion flow. The cathode of the discharge (also acting as the neutralizer) is an external cathode. HETs usually have specific impulses slightly lower than ion engines, but higher thrusts and simpler designs (see table II.9). Yet, they suffer from low efficiency, especially at low power. Exotrail is developing a fully integrated miniaturized HET named ExoMG-nano. The thruster is expected to provide an I_{sp} of 1,000 s and a thrust of 1.5 mN when powered with 40 W [111, 112].

Field Emission Electric Thrusters and Electrospray Thrusters

Field Emission Electric Propulsion (FEEP) and electrospray thrusters rely on the utilization of a strong electric field to produce a spray of charged ions and/or droplets. More precisely, a potential difference is applied between an electrode and a conductive liquid surface. The compensation of this electric field by the surface tension generates Taylor cones on the liquid surface. When the field is strong enough, ions and droplets are extracted from the tip of the cone. Electrospray thrusters use ionic liquids that have a low vapor pressure as propellant, which releases the constraint on pressurized tanks. With some propellants, they also allow the generation of both positive and negative ions. In order to accelerate both ions at once, alternating electric fields are required. As a result, there is no need for an external bulky cathode to neutralize the ejected ions, unlike in ion and Hall thrusters. By contrast, Field Emission Electric Propulsion (FEEP) thrusters use liquid metal propellants, usually indium or cesium, which require a neutralizer. Generally, FEEP and electrospray thrusters provide high specific impulse and very low total thrust (as displayed in table II.10). Hence, they enable very fine attitude control or efficient acceleration of small spacecraft over long periods of time. However, they are very complex. In 2018, Enpulsion performed a qualification mission of the IFM Nano Thruster [116] (see figure II.9), a thruster of 750 g that consumes 40 W and claims an I_{sp} of 3,770 s [111, 112].

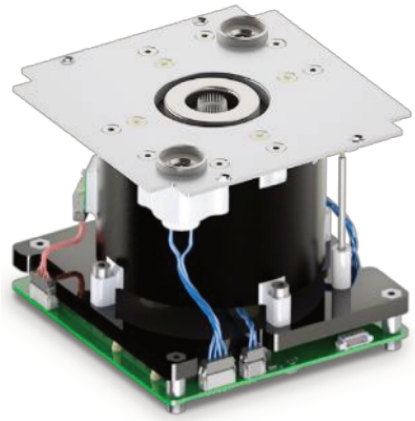

Figure II.9: IFM Nano Thruster. Credit: Enpulsion [112].

Table II.10: Performance of Field Emission Electric Propulsion (FEEP) and electrospray thrusters.

Model	Mass [kg]	Power [W]	Thrust [µN]	I_{tot} [N s]	I_{sp} [s]
IFM Nano [111, 112]	1	40	350	7,800	3,770
S-iEPS [117, 118, 119]	0.123	1.5	74	319	1,160
TILE-50 [120, 121]	0.055	1.5	50	60	1,250
TILE-500 [120, 121]	0.844	8	400	3,000	1,250
TILE-5000 [120, 121]	1.426	30	1,500	4,800	1,500
BET-100 [122]	0.550	5.5	100	175	2,104
BET-1mN [123]	1.150	15	700	605	800

II.3.3 - Comparison of CubeSat Compatible Thrusters

In figures II.10 to II.12, I compare the performance of identified CubeSat propulsion devices by means of the classical parameters that we have defined in section II.2. Propulsion devices are regrouped by categories: for a given category, the performance is represented by an ellipse centered at the average performance and for which minor and major axes are proportional to the spread in thrust and specific impulse.

Regarding the thrust and the specific impulse, we can observe in figure II.10 three main categories of propulsion systems:

- CGTs and electrothermal propulsion systems deliver very low performances, especially specific impulse, that are compensated by their simplicity and reliability.

- Mono and bi-propellant systems, together with solid motor rocket systems, provide high thrust levels recommended for missions requiring fast and low-precision orbital maneuvers, such as debris removal.

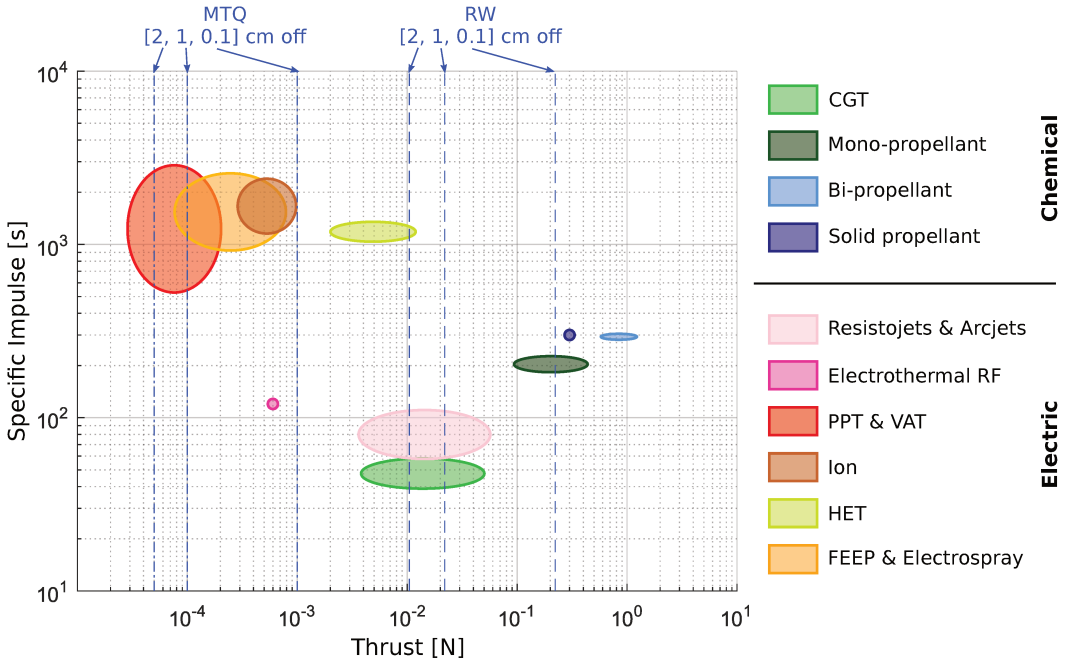

Figure II.10: Specific impulse and thrust of identified propulsion systems (when data are available). Ellipses are centered at the average value and their minor and major axes are representative of the spread in thrust and specific impulse. Blue dashed lines represent the level of thrust that conventional magnetorquers and reaction wheels for 3U CubeSats can compensate (see identified actuators in sections IV.1.5). Three values of offset between the center of mass and the center of gravity are considered to compute the corresponding thrust: 0.1 cm, 1 cm and 2 cm.

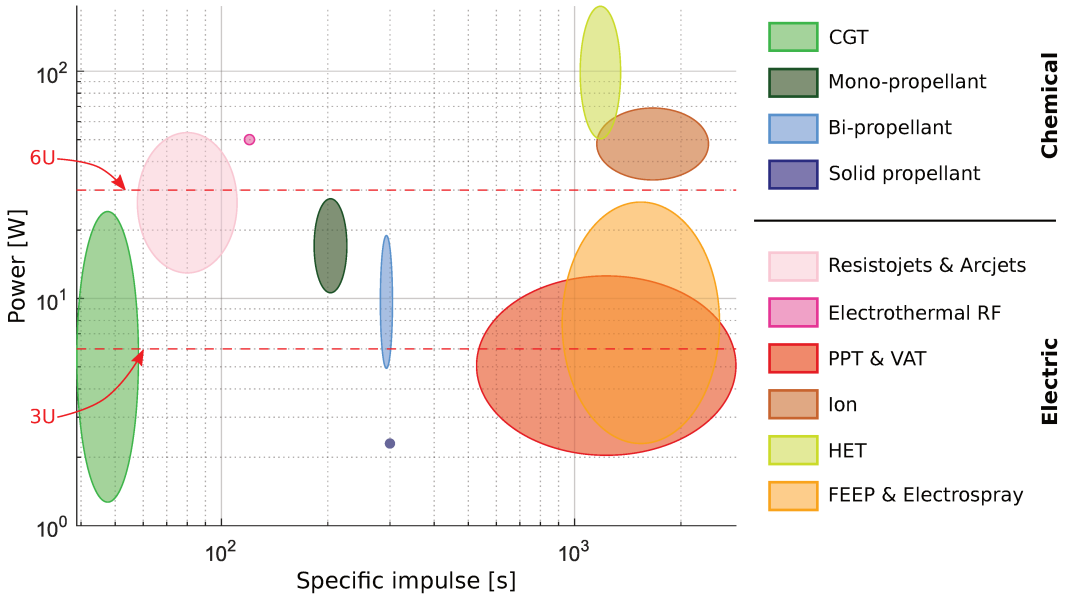

Figure II.11: Power and thrust of identified propulsion systems (when data are available). Ellipses are centered at the average value and their minor and major axes are representative of the spread in specific impulse and power. Red dashed lines represent the amount of power that can be produced by 3U and 6U CubeSats at 1 au from the Sun and without deployable solar panels (such considerations are detailed later on in section III.2.1.3).

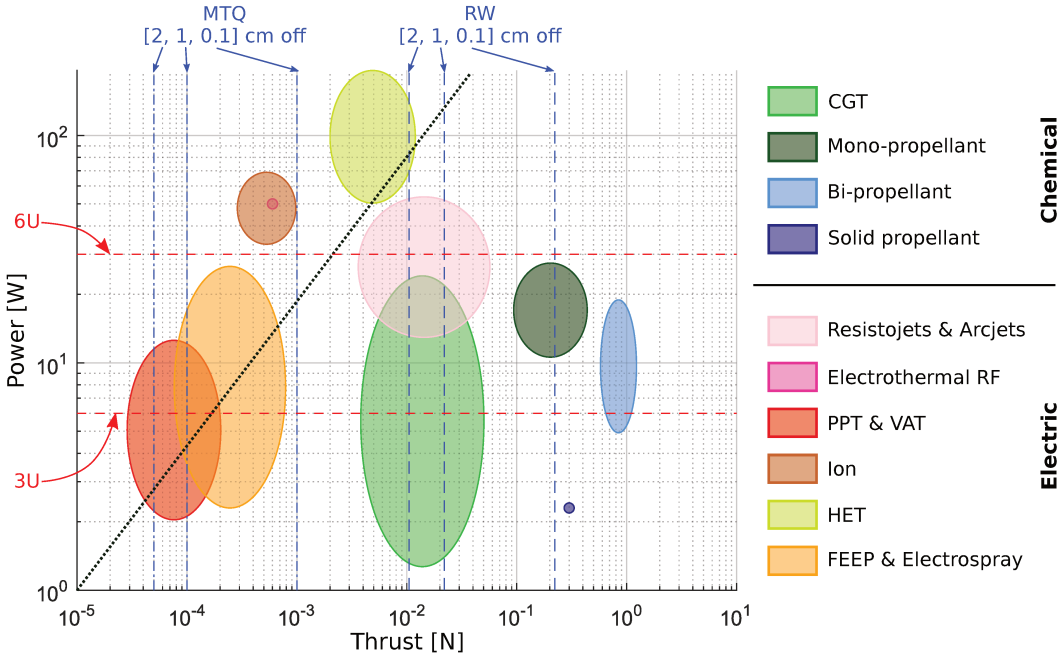

Figure II.12: Same as figures II.10 and II.11 but with power as a function of thrust. The black dotted line represents the link between power consumption and thrust for electric propulsion systems.

- Electromagnetic and electrostatic systems provide the highest I_{sp}, especially VATs, ionic and electrospray thrusters. When combined to their low thrust levels, it makes them ideal for low thrust orbit transfers and attitude control. One can also notice that HETs are an excellent compromise between thrust and I_{sp}.

The action of any thruster also has to be considered inside a larger system: the more efficient the thruster, the more drastic the cost of its use. It is possible to set a maximum boundary to the thrust, evaluating the maximum disturbances that attitude actuators can overcome to ensure that the spacecraft will not be lost tumbling. As a matter of fact, a misalignment of the thrust vector and the Center Of Mass (COM) of the spacecraft will result in a torque. The CubeSat Design Specification (CDS) provides requirements for the location of the COM with regard to the Center Of Geometry (COG) of the spacecraft [6]. For a 3U CubeSat, the COM shall be located within 7 cm from its geometric center in its length, and 2 cm in its height and width. Orbital propulsion system will most likely be thrusting along the largest direction, hence it is reasonable to assume that a misalignment of 2 cm shall be controlled if the CubeSat complies with the CDS. For the performance of attitude actuators, I choose the CubeWheel Small from CubeSpace which produces torques up to 0.23 mN m representative of available Reaction Wheels (RWs) for 3U CubeSats [124], and the Magnetorquer board from ISIS delivering 0.2 Am^2 of magnetic moment [125]. In order to evaluate the maximum torque that this Magnetic TorQuer (MTQ) can produce, one needs to know the local magnetic field. In LEO, I estimate that it represents $\sim 1\,\mu N\,m$. The maximum thrusts computed following this logic are displayed in figures II.10 and II.12.

When considering the power requirements of identified propulsion systems, let us first perform a rough evaluation of what can usually be produced by a CubeSat in Earth orbit (see a more detailed approach in section III.2.1.3). Omitting shadow periods, CubeSats can typically produce 2 W per unit in LEO when covered with current solar cells. For 3U and 6U CubeSats, this means that they produce up to 6 W and 12 W respectively. One must keep in mind that more power can be produced if the spacecraft carries deployable solar panels. From figures II.11 and II.12, we can now distinguish three categories:

- CGTs and solid motor rocket devices are very energy efficient. In general, CGTs only need power for valve actuation, although for some concepts, more power is necessary to vaporize the propellant stored in liquid or solid form. Regarding solid motor rockets, only the ignition phase consumes power.
- A rather large group of propulsion systems consumes between several watts and several tens of watts. In this category, we have the rest of chemical propulsion systems, namely mono- and bi-propellant thrusters, whose power demand relates to the need of engine preheating. Electromagnetic thrusters (PPTs and VATs) and electrospray thrusters are also part of this category. Yet, their low thrust usually requires very long firing periods associated with a continuous power demand. Finally, electrothermal thrusters overlap this category and the following.
- Among thrusters requiring too much power for most regular CubeSat platforms, we find the rest of electrothermal thrusters, ionic thrusters, and especially HETs.

Finally, an interesting feature of electric propulsion systems is visible in figure II.12, it is the link between the power consumption and the delivered thrust.

I sum up all the previous considerations about propulsion systems for CubeSats in table II.11.

Although the classic approach allows a first comparison of available thrusters, the specific impulse falls short of capturing many essential system aspects, such as the hardware mass, the electric power supply, the thermal and electromagnetic shielding, when needed, or the attitude control capabilities. These inefficiencies appear obvious when these criteria are applied to nano/micro-satellites such as CubeSats, as we will see in the following sections.

II.4 - Limits of the COTS Approach

The CubeSat approach generally consists in using COTS in order to quickly and easily build platforms. It has been made possible thanks to the standardization of the CubeSat format and has proven to be efficient on many LEO missions. So far, we have seen how propulsion devices compare with each other, using the performance indexes that propulsion designers usually communicate. Despite the fact that some suppliers can provide detailed data packages on request, only incomplete information is freely accessible: typically, thruster manufacturers communicate on a set of

Table II.11: Rough characteristics of main propulsion techniques.

Type	Simplicity - reliability	I_{sp} [s]	Thrust [N]	Power [W]
CGT	High	40–68	0.001–0.06	0.3–55
Mono & bi-propellant	Average	169–310	0.1–1.2	6–35
Solid motor rocket	Average	187–300	0.3–258	> 1
Resistojets & arcjets	Average	49–150	0.005–0.15	15–100
PPT & VAT	Average	536–5,000	0.000,02–0.000,12	2–30
Ion	Low	2,000–2,300	0.000,3–12	50–56
HET	Low	1,000–1,375	0.001,5–0.013	40–200
FEEP & electrospray	Low	800–3,770	0.000,5–0.001,5	1.5–40

standard metrics, namely the thrust, specific impulse and power. Any comparison of thrusters based on these metrics is a first step, but it is far from being sufficient. Although propulsion is the subsystem ultimately dedicated to performing orbital maneuvers, this definition often leads to a low-level approach. As a matter of fact, propulsion needs to be thought as part of a bigger picture called the Attitude & Orbit Control System (AOCS) to deliver the expected performance.

II.4.1 - Importance of the Propellant

As mentioned in the introduction of this section, the nature of the propellant used in thruster concepts, and the way it is used, is a prerequisite of the feasibility of a Unified Propulsion System (UPS). In addition, characteristics such as the propellant storage pressure, toxicity or explosivity are factors that must be considered when selecting a propulsion system, especially for CubeSats.

- Pressurized tanks were forbidden in earlier versions of the CubeSat Design Specification (CDS). Even if this constraint is withdrawn, vessels at high pressure are still a concern for rideshares because they put the main mission at risk. Same goes for explosive propellants.
- Toxic propellants like hydrazine come with many handling restrictions that increase mission costs, in particular during integration.

We gather our main findings in table II.12.

Table II.12: Propellant based comparison of propulsion thrusters. UPS means Unified Propulsion System.

Type	Compatibility with UPS	Storage pressure	Toxicity	Explositivy
Compressed gas	Yes	Generally high	No	No
Vaporizing liquid	Depends on the liquid	Generally low	No	No
Liquid mono-propellant	Yes	Average	Yes (hydra.) No (green)	No
Liquid Bi-Propellant	Yes	Average	Yes	No
Solid motor rocket	No	No	Generally yes	Flammable
PPT	No (solid) Yes (liquid)	No (solid) Low (liquid)	No	No
VAT	No	No	No	No
Resistojets	Yes	No	No	No
Ionic thruster	Yes (gas) No (iodine)	High (gas) Low (iodine)	No	No
HET	Yes (gas) No (iodine)	High	No	No
Electrospray	No	Low	No	No

II.4.2 - Propulsion as Part of the Attitude & Orbit Control System

Historically, CubeSat missions were flying without any Attitude Determination & Control System (ADCS) or with basic ones, but recent developments and bigger platforms have enabled three-axis attitude control in LEOs, and the current performances of CubeSat attitude control enable applications necessitating precise pointing. For instance, the XACT-15 designed by Blue Canyon Technologies [126] is an all-in-one ADCS for LEOs claiming $\pm 0.003^\circ$ (1-sigma) for two axes and $\pm 0.7^\circ$ (1-sigma) for the third axis within only half a CubeSat unit. It is important to acknowledge that, at the moment, all-in-one ADCS available on the shelf are dedicated to low Earth orbiting CubeSats. Indeed, they are based on technologies that cannot operate in deep space, such as magnetometers and MTQs. Because attitude actuators are rather limited in numbers, precise pointing is performed by RWs. Their working principle imposes regular desaturation that must be performed by other actuators on-board the spacecraft: this is where MTQs come into play. As soon as CubeSats leave the Earth magnetic field, the only techniques left to desaturate RWs are via passive interactions with the solar wind or with reaction jets. The latter being far more efficient, it is the most common solution. Since thrusters can be used

to produce control torques, some missions also decide to only carry Attitude Control Thrusters (ACTs) and get rid of RWs. Two interplanetary CubeSat missions from NASA embark CGTs to perform the attitude control, namely Inspire [43] and MarCO [1]. If the former is still waiting for a launch date, the latter successfully completed its Mars fly-by, providing a data relay to Insight.

Nowadays, another level of complexity is introduced by orbit control, especially when considered as part of the AOCS. For instance, the thrust vector needs to be nominal for the completion of the expected orbital maneuver, yet its dispersion about the average performance is rarely provided in high-level data sheets (although specifications for most thrusters include requirements on the thrust vector). For mission designers in general, as will be shown in this thesis, system-level considerations are more important than pure subsystem performance. This is where the classic approach is flawed, omitting the other subsystems required to perform the expected orbital control.

Tardivel et al. [30] propose an extensive study of technology enabling interplanetary trajectories. Of the various results of their work, one can cite relations between launch opportunities and electric transfers, and the necessity for propulsion systems with high I_{sp} to also deliver at least few millinewtons of thrust for interplanetary travels to remain feasible with CubeSats in terms of duration. However, they do not address at all the challenges in terms of attitude control, despite their impact being far from negligible as we will see later on. Xia et al. [127] insist on the necessity to perfectly control their CubeSat attitude during formation-flying maneuvers. They design an attitude and orbit coupling control algorithm resulting in orbit maneuver effectiveness above 95 %. Hudson et al. [35] also develop attitude and trajectory control strategies, except it is for a CubeSat equipped with electric propulsion. Thrust vectoring capabilities are assumed (ability to adjust the thrust vector with a mechanism without having to modify the attitude of the spacecraft) for small angles, but this technique is complex and tends to lower reliability. In another study, Hudson et al. [128] investigate the efficiency of low-thrust spiral arcs with various micropropulsion systems, considering constraints such as power, fuel mass or mission duration. However, attitude control is only briefly mentioned and it is expected to ideally support control strategies.

From the literature, we can also see that disturbance torques caused by propulsion systems are mainly left out. This concern is not relevant in Xia et al. [127], because their solution comes with several thrusters, hence enabling disturbance torque compensation by alternating between thrusters. When only one thrust vector is provided by a propulsion system, which is generally the case for electric systems, disturbance torques become a major concern. Spangelo and Longmier [129] make an optimization of the system-level design of an Earth-escape CubeSat using the CubeSat Ambipolar Thruster. Power, thrusting intervals and attitude control inputs are variables of this optimization, and a sensitivity study of attitude pointing errors on the orbital maneuver duration is presented. Yet, they omit the impact of disturbance torques caused by the propulsion system. They also suggest to desaturate RWs by carefully controlling the solar panels orientation once the Earth magnetic field becomes too weak, which is likely to be incompatible with the maneuver duration that they obtain. Edlerman and Kronhaus [27] study electric propulsion capabilities for a formation flying mission considering a realistic attitude control strategy, yet they

do not refer to undesired torques.

The problem of inherent disturbance torques is especially critical for very small satellites. Although classical satellites are also limited by attitude actuators (higher propulsion capabilities result in higher disturbance torques), they usually benefit from having multiple thrusters to provide both attitude and orbit control through "on-off modulation" [130]. On the contrary, propulsion systems developed for CubeSats tend to provide only one axis of thrust, thus preventing from performing attitude control. Two recent missions highlight the importance of attitude control during the design of propulsion for CubeSats. In the D-SAT demonstration mission [84], dedicated to qualifying a solid motor rocket for enabling fast deorbiting capabilities to nanosatellites, the 3U CubeSat was lost when the orbital maneuver was performed, despite a requirement of a maximum error of 1.5 mm in the alignment of the thrust vector during integration. Investigations have shown that this requirement was not satisfied, although extensive testing was performed prior to launch. Similarly, the qualification mission of the IFM Nano Thruster experienced a loss of attitude control that led to a less effective maneuver [116]. It goes to show that the disturbance torque produced by the misalignment of the propulsion system is bounded by the performance of the ADCS, whose design must be performed for the worst case (see figures II.10, II.11 and II.12).

Finally, the identified limits of the COTS approach can be summarized in two points:

- low-level performance assessment instead of system-level metrics,
- omission of attitude actuators and disturbance torques due to propulsion.

They will be investigated in the following sections, through the proposition of a new system performance metric for propulsion systems and an AOCS simulation environment.

CHAPTER III

Functional Analysis

In the previous section, we have investigated the classic approach to propulsion systems and how thruster designers communicate about the performance of their systems. Going back to the two scientific concepts motivating this thesis (sections I.2 and I.3), we see that they require both attitude and orbit control in deep space. To fill the gaps identified in section II.4, I perform a functional analysis and identify high-level requirements relating to the Attitude & Orbit Control System (AOCS) for the cruise and the proximity operation contexts. It appears crucial that we remain flexible regarding hardware and strategies, which are likely to evolve until we find the best combination. As a consequence, we will perform an analysis as modular as possible. The functional analysis will also allow simulation and testing early in the process.

An investigation of propulsive strategies, in particular in the more demanding case of proximity operations, is also part of this analysis. As we will see, it is essential to take the orbit control in account since it strongly constrains some of our requirements.

III.1 - Mission Modes

Every mission cycles through several phases, some of them being more common than others. For a specific project, identifying the various phases is essential in order to propose modes of operation for the spacecraft. To each mode, one can associate actions that can be sized. In this section, we identify AOCS modes in the scientific scenarios of BIRDY-T.

Orbit Insertion

The first mission phase for the CubeSats is the orbit insertion. It is the period during and after boost while spacecraft is brought to the final orbit. It is provided either by the host mission that will jettison the CubeSat on the Earth-Mars trajectory, or by the mother craft for the proximity operation mission. During this phase, the AOCS, like the rest of the CubeSat, will be turned off. Therefore, only limitations imposed by the deployer or the host mission may concern the AOCS,

particularly the propulsion system. For instance, previous versions of the CubeSat Design Specification (CDS) used to specify a maximum pressure on-board CubeSats for safety concerns, thus making compressed gas thrusters unfit to rideshares.

Acquisition

Once deployed, the spacecraft will enter the acquisition phase. It corresponds to the initial determination of attitude and stabilization (detumbling mode) of the vehicle. From common CubeSat regulation, a 30 min delay is imposed after the CubeSat has been jettisoned, which means that no action can be performed by the CubeSat during this lapse of time. Once this delay is over, the CubeSat may start canceling the angular velocity induced by the deployer. The location of the satellite COM is key regarding initial angular velocities, which is the reason why it is specified in the CDS. Another source of attitude perturbation at this stage is the deployment of solar panels if such a solution is chosen. Thus, they should be deployed before the CubeSat starts detumbling, but after the 30 min regulation. In the literature, many CubeSat missions consider $10\,^\circ\,s^{-1}$ initial angular velocity on each axis [131]. In some cases, much higher velocities have been observed, as for DeorbitSail[1]. Therefore, an angular speed of $50\,^\circ\,s^{-1}$ affecting the three axes of the satellite is considered as our worst-case. It may also be necessary to cancel the initial relative velocity, usually of the order of $1\,m\,s^{-1}$, in order to stay on the initial trajectory, especially in the cruise context. This would be a first Trajectory Correction Maneuver (TCM).

In-flight Orbit Determination

The In-Flight Orbit Determination (IFOD) is a cornerstone of BIRDY-T. Indeed, the success of both scientific cases depends on a high level of autonomy, which is challenging in particular for the orbit determination. In the cruise context, the IFOD shall produce several estimates of the position during the Hohmann transfer orbit without assistance from the ground segment. This estimate shall be compatible with the agility of the AOCS. The optical data necessary for the IFOD shall come from a slow scan of the ecliptic plane, so as not to interrupt scientific measurements. If more data are required, the interruption of the scientific measurements and the use of Attitude Determination & Control System (ADCS) shall be minimal. For proximity operations, the precision of the IFOD shall be better than the altitude of the overflight. It shall also execute fast enough to be compatible with multiple overflights at approximately $1\,m\,s^{-1}$. The main IFOD sensor is expected to be a star tracker-like or a navigation camera.

Navigation

The major phase in sizing the AOCS for the two CubeSat missions is the navigation. It is a key part in the success of both missions.

In the cruise context, TCMs are required to reach Mars and communicate with an orbiter, and hence ensure the minimal success of the mission. Complete success requires catching the free return trajectory to the Earth, allowing a second science phase. The CubeSat should intersect the exact region of the Mars fly-by B-plane that allows a free-return trajectory to the Earth. Initial studies have shown that

[1] https://amsat-uk.org/2015/11/13/deorbitsail-update-and-initial-camera-image/

a $2\,\mathrm{m\,s^{-1}}$ ΔV is sufficient to change the aphelion by more than 30.000 km along the ellipse axis and 180.000 km if applied at a true anomaly of 90 deg during the Hohmann transfer from Earth [15]. Thus, the ΔV budget is not a concern.

In the proximity operation concept, the CubeSat is meant to explore the gravity field of the system of asteroids. For the AOCS, it means that regular autonomous TCMs will be performed. This translates into robust maneuvers that should not endanger the spacecraft despite operating in close proximity of the system of asteroids and relying on an imprecise orbital knowledge. As a first optimistic approximation, we assume that each TCM represents a ΔV of $2\,\mathrm{m\,s^{-1}}$. For a three-month mission, approximately 40 hyperbolic arcs are performed, and the same amount of TCMs is required, which represents a total ΔV budget of $80\,\mathrm{m\,s^{-1}}$. This rough evaluation is refined in section III.3.

Science

In the science case, the measurements consist in a slow spin in the ecliptic plane to detect incoming cosmic rays on a Hohmann trajectory to Mars. In the other case, radio-science will be performed during overflights of the system of asteroids at close proximity and low relative velocity ($\sim 1\,\mathrm{m\,s^{-1}}$). Science measurements should last approximately one day. One-way or two-way signals between the CubeSat and the mother craft/ground antennas in X and S-bands are required. Endurosat[2] designed an S-band antenna with 71° half-power beam width, while an X-band from Anywaves[3] with 40° half-power beam width is also available. Pointing requirements will therefore be several tenths of degrees, well above the performance of any CubeSat actuator.

Telecommunication

Two telecommunication slots exist in the cruise context: the first one with a Martian orbiter and the second one with a VLBI ground station on Earth. The system is sized for communications in UHF/VHF and S-band (very low pointing requirements). During the transfer orbit, only a regular beacon will inform the ground station of the CubeSat status, which does not impose any requirement to the AOCS. When it comes to the second concept, the telecommunication will be performed by the scientific payload (see science mode).

Safe Mode

The safe mode is used in case of emergencies if a regular mode fails or is disabled. It should sacrifice normal operations to meet power or thermal constraints and be able to receive commands from mother craft or Earth. In safe mode, the satellite usually roughly points in a certain direction, for instance to the Sun in order to recharge its batteries.

[2] https://www.endurosat.com/cubesat-store/all-cubesat-modules/s-band-patch-antenna/
[3] https://newspace-factory.com/product/cubesat-x-band-antenna/

III.2 - AOCS Environment

The CubeSats will perform their missions in conditions very different from common Low Earth Orbits (LEOs). The AOCS has to accommodate to this new environment like the rest of the spacecraft. Moreover, it must be compatible with other subsystems.

III.2.1 - External Environment

Space is a very complex and dynamic environment, filled with gravitational fields, electromagnetic radiation, highly energetic particles or magnetic fields. Every spacecraft is submitted to all these phenomenons and must be designed accordingly.

III.2.1.1 - Radiative Environment

In terms of radiation, for a satellite on a LEO, the main issue comes from geomagnetically trapped protons and electrons [132]. Such radiation is a concern for any spacecraft, and especially CubeSats constructed with non-radiation-tolerant Commercial Off-The-Shelf (COTS) equipment. Their long-term accumulation is measured by the Total Ionizing Dose (TID). The TID causes slow gradual degradation of equipment's performance. While first anticipations from the community were very pessimistic, COTS have proved to be surprisingly resistant, and some CubeSats operated in LEOs for years. In [133], it is shown that the TID in Geostationary Earth Orbit (GEO) is five orders of magnitude higher than in LEO, and that less than 1 mm of aluminum shielding can reduce the difference to one order of magnitude. But the GEO is still within the radiation belts, and the TID in deep space is significantly lower. However, once spacecrafts leave the protection of the Earth's magnetosphere, they still have to face a harsh environment. They are submitted to the continuous solar wind, made of protons and positive ions traveling at approximately $400\,\mathrm{km\,s^{-1}}$, cosmic rays and random Solar Particle Events (SPEs) (proton storms). Apart from the long-term effect related to TID, highly energetic particles such as the neutrons cause Single Event Effects (SEEs) that may result in permanent damage. Although both hardware (shielding, redundancy) and software (watchdog) mitigation techniques are generally present on large satellites, they come at the cost of mass, complexity and budget, and will be harder to implement on-board CubeSats. All these radiation constraints will impact the AOCS.

III.2.1.2 - External Disruptive Forces

Every spacecraft is also affected by external forces, or disturbances, that are known for altering both its attitude and its orbit. External disturbances have four main sources:

- the Solar Radiation Pressure (SRP), mainly due to energetic particles coming from the Sun,

- the atmospheric drag, resulting from the friction between the spacecraft and an atmosphere,
- the magnetic field, due to the interaction of the residual magnetic field of the spacecraft and an ambient magnetic field,
- the gravity, related to massive bodies.

First, I evaluate their impact on the attitude of the spacecraft. Those external disturbances are presented in more detail in IV.1.4, together with their simulation. A schematic of their evolution as a function of the location in space is displayed in figure III.1. One can see that depending on the mission, a satellite will encounter different levels of external disturbances.

For now, we are interested in evaluating the maximum impact that those four perturbations may have in our two contexts. Hence, they are plotted as a function of the altitude from the bodies of interest (Earth and Mars in the first case, Didymos in the second) in figures III.2 and III.3. It should be noted that, when sizing the environmental perturbations, I consider a 3U CubeSat with no deployable solar panels for simplification. Hence, real disturbance torques may be higher than those computed here, but still in the same order of magnitude. Moreover, torques due to the magnetic field and the atmospheric drag are not computed at Mars because of the absence of a dense atmosphere and strong magnetosphere on the planet.

From this worst-case analysis, one can see that the SRP will dominate on an Earth-Mars-Earth trajectory, and that external torques should always be lower than $1 \times 10^{-8}\,\mathrm{N\,m}$. This value will be a minimum for the selection of our actuators' performance. Although the radio science of Didymos differs greatly from the cruise context, the same level of external perturbations may be expected. This is due to the highly eccentric orbit of Didymos and its very low gravity field.

Let us now focus on the orbital impact that those external perturbations will have on the CubeSats trajectory. In the interplanetary scenarios, the main undesired perturbation is the SRP. Indeed, the gravity attraction of Mars is responsible for the expected gravitational slingshot that will bring back the CubeSat to Earth. In the case of the radio-science experiment at Didymos, the gravity of the asteroids is what we want to study. Hence, we are interested in the level of the undesired SRP effect. At 1 au, the SRP is $\sim 1 \times 10^{-6}\,\mathrm{Pa}$, equivalent to a variable force of $0.03\,\mu\mathrm{N}$. This is two orders of magnitude lower than the gravity force from Didymos for an object at 10 km. Because the SRP decreases with the square distance to the Sun, it is safe to say that its orbital impact can be neglected as a first approximation.

III.2.1.3 - Incoming Power

The power available is a crucial parameter for the selection of hardware. In what follows, I perform a quick evaluation considering ISIS solar cells [135]. At Beginning Of Life (BOL), they deliver 6.9 W of peak power at 1 au. We are interested in knowing the Orbit Average Power (OAP), which defines how much power is available per orbit. For a LEO 3U CubeSat covered with solar panels on its largest faces, a rule of thumb tells us that OAP is 60 % of the power from one panel [136]. It means

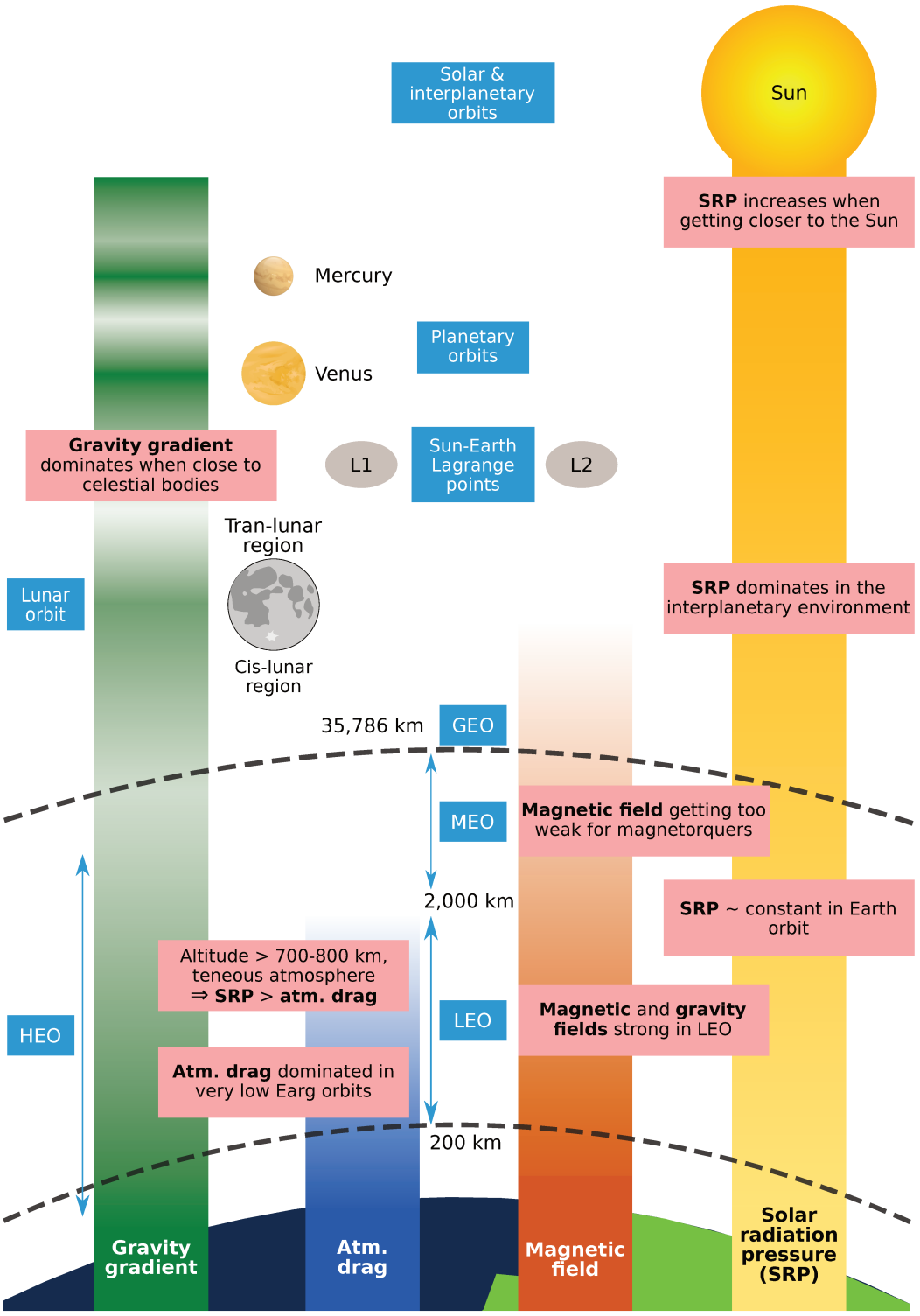

Figure III.1: External disturbances acting on a spacecraft [134]. The intensity of the color depicts the intensity of the disturbance.

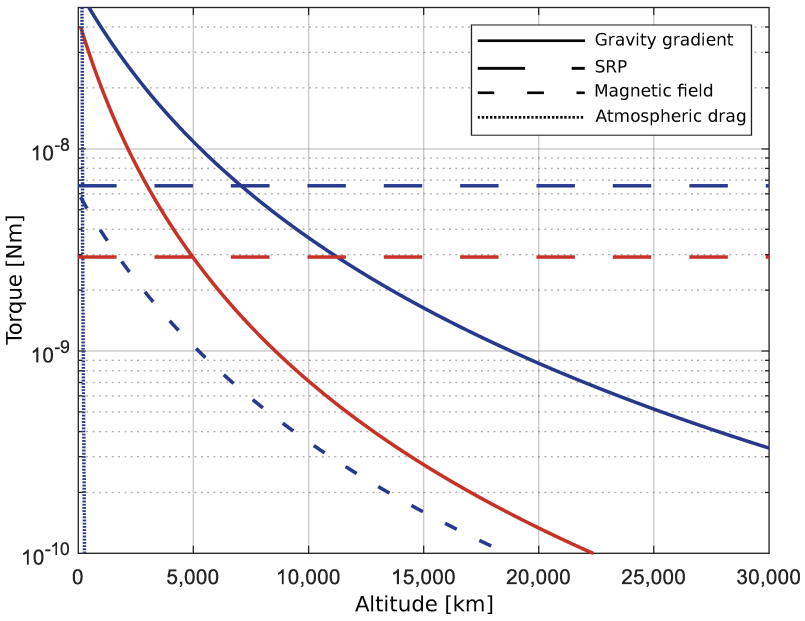

Figure III.2: Maximum disruptive torques induced by the external forces acting on a 3U CubeSat in the cruise context. Blue curves represent disturbances around the Earth while red curves represent disturbances around Mars. The Solar Radiation Pressure (SRP) at Mars is computed for a distance of 1.5 au. Magnetic and atmospheric torques at Mars are not computed for obvious reasons.

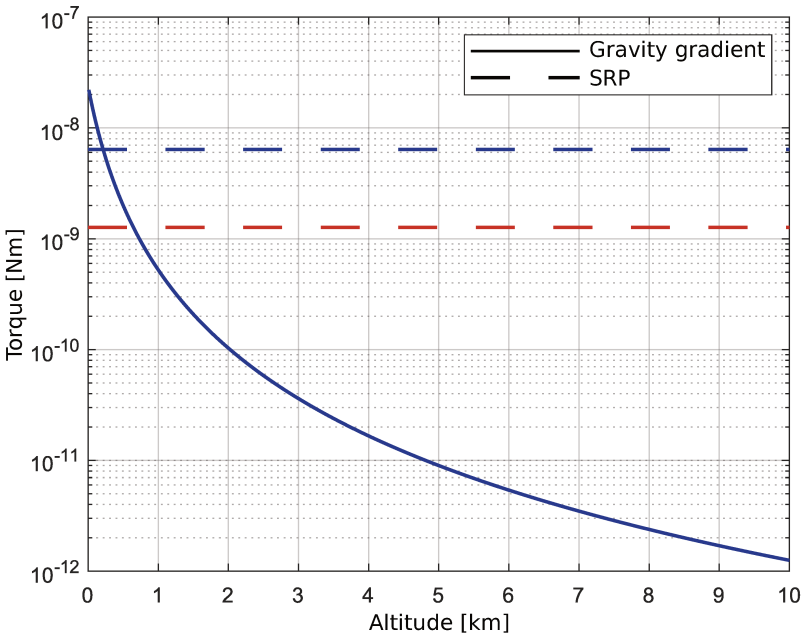

Figure III.3: Similar to figure III.2 but for the proximity operation context. The Solar Radiation Pressure (SRP) is represented at the perihelion (1.013,5 au) in blue and at the aphelion (2.275,5 au) in red.

Table III.1: Orbit Average Power (OAP) for a 3U CubeSat covered with solar panels on its largest faces [135].

Context	Peak power [W]	OAP at BOL [W]
LEO	9.8	4.1
Mars at perihelion	5.1	4.6
Mars at aphelion	3.5	3.2
Didymos at perihelion	9.4	8.4
Didymos at aphelion	2.4	2.2

that, at BOL, the OAP is 4.1 W. One must be aware that those 4.1 W represent 15 % of the total capacity of the satellite (four solar panels, one on each face).

When it comes to our scientific cases, the power collection will not be altered by eclipses. Even if the proximity operation implies that the CubeSat will sometimes be shadowed by Didymain or Didymoon, this will happen very rarely considering the size of the bodies and the fact that we are not orbiting around it. In addition, when the CubeSat is in close proximity, it performs radio-science measurements, which means that the propulsion is turned off - only attitude control is required to ensure the minimal pointing. The OAP in our scenarios for the proposed CubeSat configuration are summed up in table III.1.

III.2.2 - Internal Environment

A CubeSat, much like larger satellites, is made of a collection of subsystems ensuring that it performs its missions. An example of the interactions of the AOCS with other subsystems is displayed in figure III.4, as well as the decomposition of the AOCS in its major on-board parts, namely the attitude sensors and actuators, the IFOD and the orbital propulsion.

All the interactions prior to deployment are taken care of by the deployer and designers need to ensure their CubeSat complies with the deployer's requirements. As a baseline, the CDS will be used.

Similarly to what happens with the external environment, there are internal sources of charged particles that tend to accumulate on the satellite. Electric propulsion systems are a major concern in that regard. For instance, ionic thrusters and HETs use an external cathode to neutralize the expelled propellant and avoid charged back flows. PPTs, VATs or electrospray thrusters (when both positively and negatively charged particles are extracted at once by an alternating potential) are exempt from external cathode because their plume is plasma. Yet, all those electric thrusters emit a certain quantity of ions and slowly charge the satellite surfaces that are within reach, especially when deployable mechanisms are present (for instance solar panels). When the potential difference between two parts of the satellite becomes too big, a sudden flow of electricity occurs named ElectroStatic Discharge (ESD). Another concern with thrusters' exhaust is the refraction of electromagnetic waves emitted by telecommunication antennas if the dense plasma plume is in their line-of-sight.

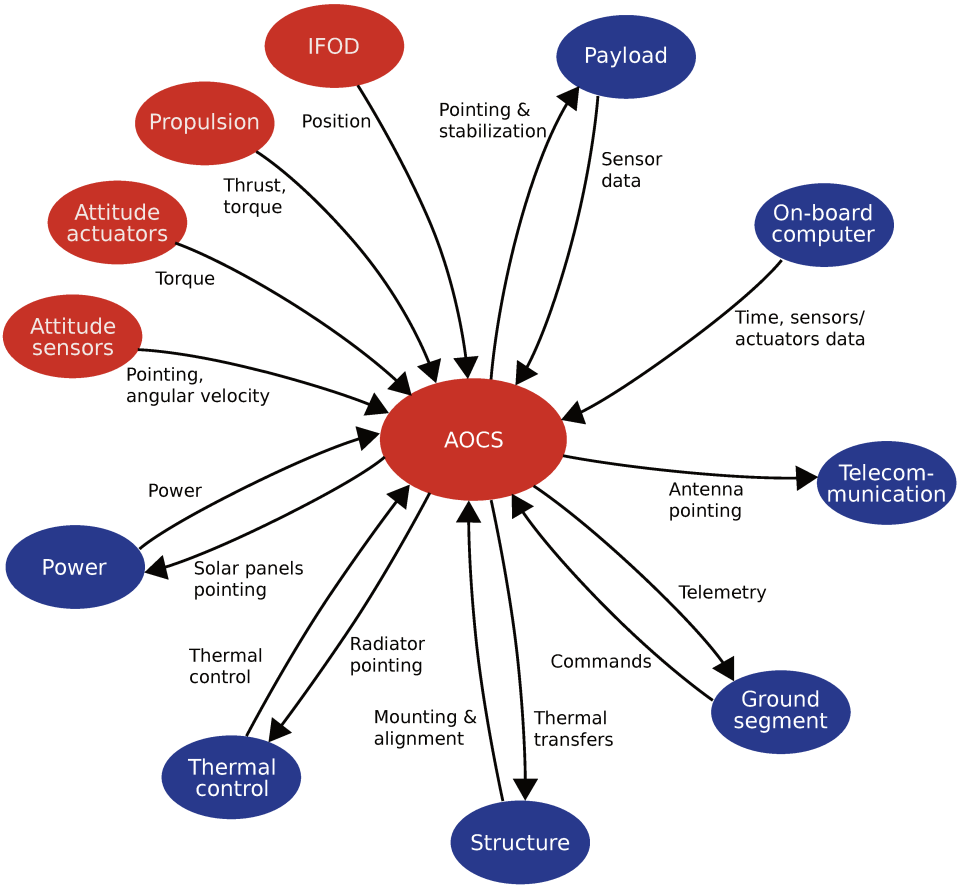

Figure III.4: Functional relationships between the Attitude & Orbit Control System (AOCS) and the other subsystems of a spacecraft. The AOCS is decomposed into its main components in red, while other subsystems are in blue.

Last but not least, the impact of energetic particles in the plume erodes spacecraft surfaces (e.g., solar panels). A careful integration and geometrical configuration are thus recommended. Electromagnetic energy is also released by CubeSat equipment, especially when systems requiring high voltages are present. Once again, this is the case of many electric propulsion systems. Consequently, ElectroMagnetic Compatibility (EMC) should be considered from the early phases of spacecraft specification. Finally, thermal loads are present on-board spacecrafts that must be radiated to space without impacting nearby components.

Previously, we have estimated the impact of external perturbations on the attitude of a 3U CubeSat. In comparison, internal perturbations, caused by equipment on-board the satellite, are usually weaker. Indeed, for simplicity and reliability reasons, CubeSat designers avoid mobile parts on-board. However, this situation is changing with the democratization of miniaturized deployable structures and propulsion systems for this category of satellites. Although some internal torques are used to control the satellite, for instance with RWs, most of them create disturbances.

- Actuators misalignment and quantification are the major source of internal disturbances in our contexts, especially propulsion misalignment. As a matter of fact, any misalignment between the COM and the thrust vector will result

in a torque. Torque levels depend on this offset and the selected propulsion system. In section II.3.3, we have evaluated the maximum thrust that common 3U CubeSat actuators can compensate for different offsets. If one can reasonably assume that a careful integration of the propulsion system will prevent large misalignment errors, vibrations during the launch and more importantly uncertainties regarding the COM location can hardly be eliminated. The CDS provides low requirements in that regard, as they only relate to the constraints of the deployer.

- Propellant sloshing, or any other liquid, may be a non-negligible source of perturbation. Sloshing modifies the mass distribution inside a spacecraft, and the inertia matrix can be greatly altered if big tanks are used. In the longer term, the inertia matrix is modified by the propellant consumption. As a result, actuators sized for the BOL, together with control laws, will be less efficient.

- Release mechanisms, such as for deployable solar panels or antennas, would most likely be activated only once in a CubeSat lifetime, probably during the acquisition phase (see section III.1).

- Moving instruments are also a source of disturbances, but they are not common on-board CubeSats and not present in our missions.

- When RWs are used for attitude control, they also produce disturbances through friction.

III.3 - Focus on Propulsive Strategies for Proximity Operations

The concept for the proximity operations requires regular TCMs that will constrain not only the ΔV budget of our mission, but the selection of the propulsion system. Therefore, it is necessary to investigate further those TCMs.

III.3.1 - Concept of Operations Based on the TCM Loop

Investigating the use of a CubeSat to study an asteroid like the Didymos system of asteroids requires propulsive strategies. As already mentioned, a radio link between the mother craft/VLBI ground stations and the spacecraft is used for Doppler and range measurements during hyperbolic arcs in the close proximity of the asteroids. A relative velocity of $\sim 1\,\mathrm{m\,s^{-1}}$ is considered at this stage. It is essential that no orbital perturbation due to the on-board propulsion occurs during those hyperbolic arcs so as not to compromise scientific measurements. Indeed, the radio science concept relies on the precise reconstruction of the trajectory, including all known perturbations, in order to infer unknown contributions, such as the local gravity

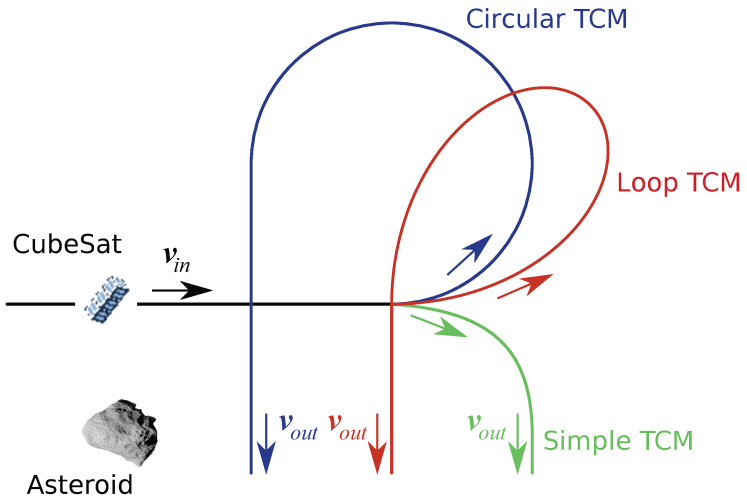

Figure III.5: Illustration of Trajectory Correction Maneuver (TCM) concepts in a reference frame moving with Didymos.

field. The variability of the acceleration due to the thrust would prevent from modeling the other perturbations correctly. After the scientific phase, the CubeSat must perform a TCM to return in the vicinity of the asteroids.

The propulsive strategy consists of a succession of hyperbolic arcs and TCM loops. Different TCMs will have different system impacts. Some of them may not be feasible with autonomous AOCS and already identified small propulsion systems for CubeSats. Moreover, TCMs cannot be considered instantaneous because of the low-thrust propulsion available for CubeSats and compatible with the relatively high ΔV demand ($2\,\mathrm{m\,s^{-1}}$ of ΔV per TCM was assumed in section I.3). The main requirements governing the selection of the TCMs are:

- to be compatible with IFOD used in BIRDY-T,
- to be robust and simple to meet with the high level of autonomy required,
- to be safe.

Therefore, three possible TCMs are presented in figure III.5, considering a continuous (or quasi-continuous) thrust all along the maneuver. They have in common easy control laws because we aim at facilitating the autonomy of the spacecraft. The idea here is to alternate hyperbolic orbits, or hyperbolic arcs, and trajectory correction maneuvers TCM.

In this figure, all the maneuvers must rotate the initial velocity vector by 90°, without modifying its norm. The most basic maneuver is displayed in green. It is obtained with a thrust of fixed direction and constant intensity, but it has the disadvantage of "missing" an important zone during the maneuver, as shown in table III.2. Such a shift (distance between the location where the maneuver starts and where it ends) means that portions of the gravity field of Didymos will not be studied, unless a more complex TCM is performed on a case-by-case basis, which is incompatible with the level of autonomy desired. Loops may be a good way of avoiding the important shift between the starting and finishing locations. Therefore,

Table III.2: Comparison of the performance of proposed Trajectory Correction Maneuvers (TCMs).

	Simple TCM	Circular TCM	Loop TCM
Duration [day]	1	1	1
Distance [km]	85.5	86.4	66.8
ΔV [$\mathrm{m\,s^{-1}}$]	1.41	4.71	3.55
Average thrust [µN]	650	220	160
Horizontal shift [km]	43.6	−18.5	0
Vertical shift [km]	−42.8	18.5	0

a circular maneuver is displayed in figure III.5 (in blue). It is obtained with a thrust orthogonal to the velocity and of constant intensity. The shift has been reduced with this maneuver, yet it is still relatively large. In addition, such a maneuver consumes 330 % more ΔV than the first proposed TCM.

Although the first two proposed maneuvers are very easy to implement, they do not facilitate mission planning. In order to remedy this problem, B. Segret proposed a TCM concept based on a well-known parametric curve: the rosette. This loop will be named TCM loop hereafter. I studied its possible implementation for the proximity operations. The mathematical approach to the TCM loop is provided in appendix D.

If we consider only one branch of a 4-leaf rosette, we notice that the outgoing velocity has the same norm as the incoming one, but has been rotated by 90° in the maneuver plan (see the red curve in figure III.5). One can also see that such a maneuver, if ideally performed, does not result in a shift, since the maneuver exactly ends where it started. The ΔV required is $3.55\,\mathrm{m\,s^{-1}}$ (to be compared with the $1.41\,\mathrm{m\,s^{-1}}$ of the simple TCM), yet the fact that no interesting areas for the scientific measurements are lost means that less TCMs will be required in the end. The total required ΔV can now be assessed, recalling that 40 TCMs are expected: $\Delta V_{mission} = 142\,\mathrm{m\,s^{-1}}$. This value should be compared to the $80\,\mathrm{m\,s^{-1}}$ proposed in the first place.

III.3.2 - TCM Loop Evaluation

To investigate the feasibility of the TCM loop with available actuators, the direction and level of thrust are computed and displayed in figure III.6. In the mobile frame (one axis oriented in the velocity direction, the second one in the trajectory plane toward the interior, and the last one completing the trihedron) the angle of acceleration only varies from 65° to 115°. The thrust value is not constant during the maneuver, which is different from the two maneuvers proposed previously. It ranges from 145 µN to 182 µN. In terms of thrust modulation, it means the thruster shall be able to perform a 25 % modulation. This value is quite common for electric propulsion systems. If no thrust modulation is possible, then it is still possible to modify the pulse frequency. The control of the thrust direction is way below the

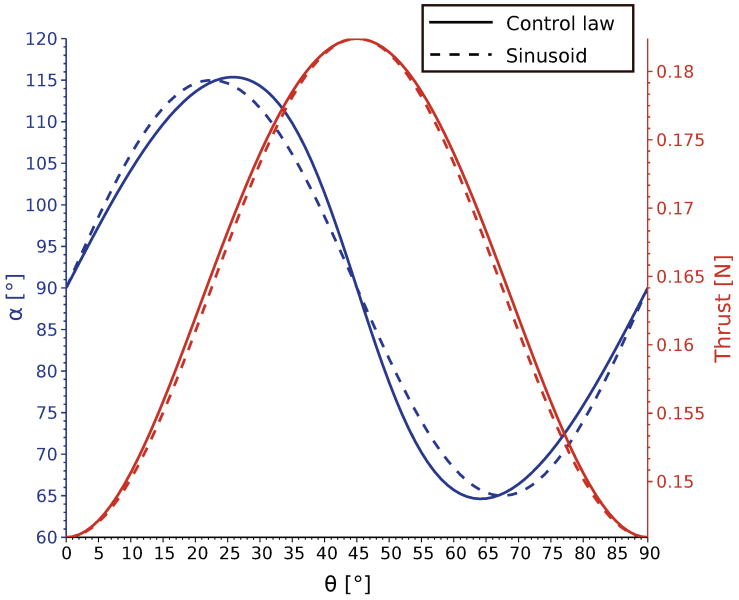

Figure III.6: Reference thrust value and direction for a one-day maneuver with the Trajectory Correction Maneuver (TCM) loop.

limitations of RWs available for CubeSats. In figure III.6, control laws are compared to pure sinusoids.

Another main benefit of the proposed TCM loop is that one can stop thrusting at any moment to obtain an outgoing velocity rotated by more or less than 90°. This indicates that the same control law can be used all along the mission, hence increasing the CubeSat autonomy.

The performance of several thrusters identified in section II.2.2, all weighing less than 1.5 kg and consuming less than 15 W, are compared when performing the TCM loop. The result is displayed in figure III.7. A zone of interest is proposed:

- maneuvers should last less than two days,
- at least 40 maneuvers should be possible.

The mass of propellant proposed by propulsion designers in their data sheet was taken.

It appears that still a large selection of the identified propulsion systems meet the initial requirements of the proposed concept of radio science. It also shows that the propulsion system will obviously be the limiting factor for the scientific mission, and the science case must make sure that a limited number of hyperbolic arcs is sufficient to provide the required information.

This evaluation allows a comparison of thrusters on criteria more important to the mission designer than the classical I_{sp}-Vs.-F chart, because the duration and number of maneuvers are mission-relevant. Yet, such an approach still omits important parameters that will be investigated in sections V and VI.

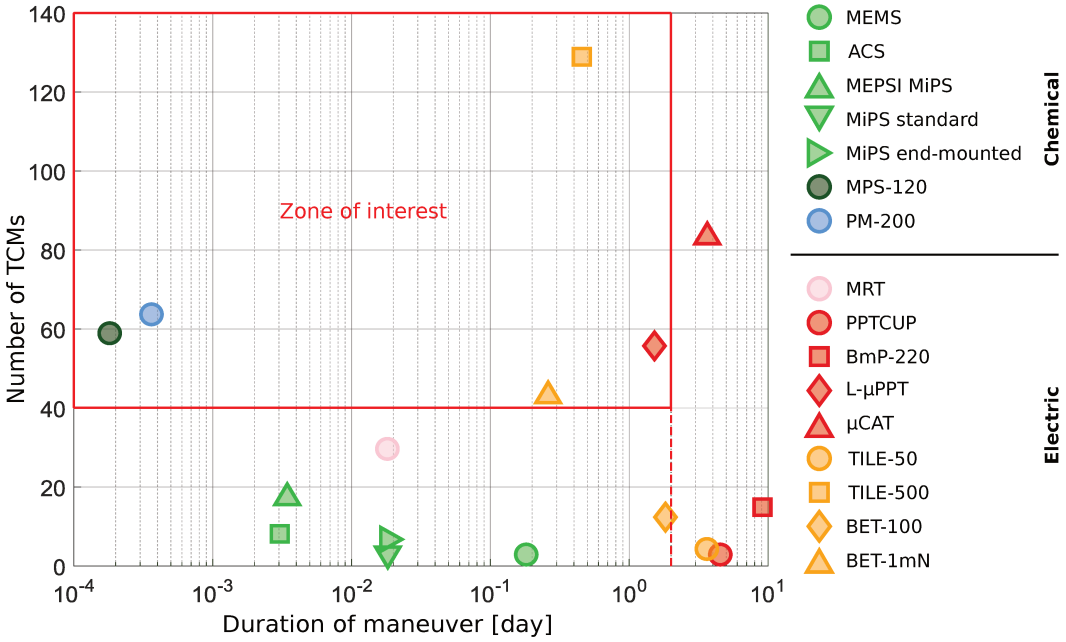

Figure III.7: Performance of small spacecraft propulsion systems for a 3U CubeSat performing the Trajectory Correction Maneuver (TCM) loop. Number and duration of maneuvers are displayed.

III.4 - Functional Requirements and Constraints

Functional requirements and constraints for the AOCS come from mission requirements and from the interactions with the environment and other subsystems, both presented in previous sections III.1 and III.2. They are listed in tables III.3 and III.4.

From the functional analysis it appears that, except for the IFOD, the orbital control is a key point in the success of our missions. Below is a list of the main difficulties related to the AOCS:

- The inherent disruptive torque caused by orbital thrust is several orders of magnitude higher than any other disturbance acting on the CubeSat. Depending on the level of thrust and the errors of alignment, it may be higher than attitude actuators.
- Conversely, pointing errors during TCMs prevent from performing the expected maneuver, resulting in increases of maneuver duration and propellant consumption.
- The limited choice in terms of attitude actuators for deep space CubeSats may require a second propulsion system, only dedicated to attitude control, either to provide active control during orbital maneuvers or to desaturate RWs.
- Having two separate propulsion systems, one for orbit control and the other one for attitude control, induces a worst-case design. A Unified Propulsion System (UPS) would be much more beneficial.

Table III.3: Attitude & Orbit Control System (AOCS) requirements in the interplanetary space weather scenario.

Requirement	Description
CRUISE-1	The AOCS shall be compliant with CDS or with main mission specifications if they are different.
CRUISE-2	The AOCS shall be able to cancel angular velocities up to $50\,^\circ\,\mathrm{s}^{-1}$ in all three axes.
CRUISE-3	The AOCS shall provide more than $10\,\mathrm{m\,s}^{-1}$ of orbital ΔV to ensure a successful Martian fly-by (500 % margin because of the high level of uncertainty at this stage and the low requirement).
CRUISE-4	The AOCS shall provide sufficient pointing to perform TCMs.
CRUISE-5	The AOCS shall enable a slow spin in the ecliptic plane and accurate attitude knowledge for the payload.
CRUISE-6	The AOCS shall tolerate the radiative environment of an Earth-Mars-Earth mission.
CRUISE-7	The AOCS shall compensate external torques up to $1 \times 10^{-8}\,\mathrm{N\,m}$.
CRUISE-8	The AOCS shall consume much less than the minimum OAP, although planned peaks of power can be handled by batteries.
CRUISE-9	The AOCS shall not contaminate nearby surfaces.
CRUISE-10	The AOCS shall ensure EMC.

- The power available on 3U CubeSats is incompatible with many propulsion solutions. It may be necessary to either consider a bigger platform or deployable solar panels. The second solution is favored because the smaller a CubeSat is, the more rideshares it accommodates to.
- If deployable structures are considered, their contamination from thrusters' plume is a concern.
- Thermal and electromagnetic perturbations from the propulsion may require additional equipment for regulation, hence increasing the mass, cost and complexity.

In what follows, I present the AOCS simulation environment that I developed in order to investigate the mutual impacts between attitude and orbit control. The numerous other impacts of the integration of a propulsion system on-board CubeSats are discussed in section VI in the light of the performance indexes. Eventually, the specific impulse introduced in section II.2 fails short in covering the numerous needs that we have highlighted and we propose a new approach.

Table III.4: Attitude & Orbit Control System (AOCS) requirements in the radio science scenario.

Requirement	Description
PROX-OPS-1	The AOCS shall be compliant with CDS or with main mission specifications if they are different.
PROX-OPS-2	The AOCS shall be able to cancel angular velocities up to $50\,^\circ\,\mathrm{s}^{-1}$ in all three axes.
PROX-OPS-3	The AOCS shall provide $142\,\mathrm{m\,s}^{-1}$ of orbital ΔV for three months of operation to be compliant with the concept of operations.
PROX-OPS-4	The AOCS shall provide sufficient pointing to perform TCMs safely.
PROX-OPS-5	The AOCS shall provide sufficient pointing for the radio science experience without disrupting the hyperbolic arcs.
PROX-OPS-6	The AOCS shall tolerate the radiative environment of Didymos.
PROX-OPS-7	The AOCS shall compensate external torques up to $1 \times 10^{-8}\,\mathrm{N\,m}$.
PROX-OPS-8	The AOCS shall consume less than the minimum OAP.
PROX-OPS-9	The AOCS shall not contaminate nearby surfaces.
PROX-OPS-10	The AOCS shall ensure EMC.

III.5 - Two Case Studies in Earth Orbit

The functional analysis that we have conducted highlighted several key aspects of the design of an interplanetary AOCS for CubeSats, among others the coupling between ADCS and GNC. This aspect being expected to be a major issue for any CubeSat mission relying on propulsive maneuvers, I decided to focus on hypothetical case studies also representative of the needs identified in section II.1.

Therefore, before we move to the simulation environment, I make up two case studies in Earth orbits. The fact that those mission scenarios are in Earth orbit allows simplifying the trajectory solver required to simulate orbital maneuvers, as explained in section IV.2.1. They are essential to open up the field of AOCS for CubeSats, and lessons learned will assist us on our two scientific missions.

III.5.1 - Deorbiting From Low Earth Orbits

We will start with a case study based on the BRITE nanosatellites [34]. The two 7 kg nanosatellites were deployed on a 780 km Sun Synchronous Orbit (SSO) in 2013 without carrying a propulsion system. As a result, they will not comply with the regulation stating that a satellite must deorbit within 25 years. At the time of

the launch, fewer satellites were concerned by this regulation, but with the growth of the debris population, especially in LEOs, the regulation law should be strictly applied now.

Hence, our case study considers that a 3U CubeSat is deployed on a 780 km SSO to perform its mission. At the end of the operation phase, the satellite shall deorbit to comply with the 25-year regulation. An orbital maneuver is thus performed to decrease the perigee to an altitude of 400 km, from where the CubeSat will naturally decay within 25 years [5]. The velocity budget is estimated to be $\sim$ 130 $\mathrm{m\,s^{-1}}$ if an ideal thrusting is applied [137]. An example of the maneuver is displayed in figure V.2. A precise analysis of the coupling between the orbit and attitude control will be conducted and will show important increases of the maneuver duration and propellant consumption, and even CubeSat loss without respecting the regulation.

Hereafter, this case study will be referred to as "deorbiting case".

III.5.2 - Earth Escape from Geostationary Transfer Orbit

Next, a CubeSat mission targeting to leave the Earth attraction on its own is taken and named "escaping case". As mentioned in section II.1, reaching an interplanetary orbit from an Earth orbit is highly demanding. From table II.1, one can see that ΔV = 5,900 km is necessary to go from a LEO orbit to the Moon. Realistically, CubeSats can only escape from Geostationary Transfer Orbit (GTO) or Geostationary Earth Orbit (GEO) [30]. In his thesis, Shimmin [48] designs a very-low-thrust trajectory to the Moon from GTO. Moreover, numerous launches target GTOs, which makes such orbits a relatively easy starting point for CubeSats.

The limit between Earth and interplanetary orbits is defined as being reached once the semi-major axis equals the distance of the first Lagrangian point of the Earth-Moon system (EML-1). Beyond that point, the Earth is no longer the main attractive body. Consequently, this point is the target of escaping scenario. We gather these considerations in a 6U CubeSat deployed in GTO. Although this case is very different from the deorbiting one, we will see that it yields the same concerns. Because of the intrinsic long duration of such maneuvers, any unplanned maneuver error might result in costly propellant increase, unaffordable for CubeSat missions made of COTS components.

CHAPTER IV

Simulation Environments

In section II.3, we have presented the standard performance parameters of the available propulsion systems we have then identified the limits of this approach. From the interplanetary science cases, we derived requirements for the Attitude & Orbit Control System (AOCS). It results that the main challenge is to appraise the mutual impacts that the Guidance Navigation & Control (GNC) and the Attitude Determination & Control System (ADCS) have on each other.

This section presents the attitude and orbit control simulation environment that I developed to investigate not only the interplanetary science cases, but also the two relevant Earth orbiting scenarios introduced in section III.5. Such case studies will help us understand what is at stake in CubeSat orbit control. Therefore, the simulation environment is introduced for the Earth context. Most of the time, only minor modifications are sufficient to adapt the simulation to interplanetary scenarios. The aim is to produce mission relevant performance indexes for identified Trajectory Correction Maneuvers (TCMs), such as duration, mass of propellant, and duty cycle.

IV.1 - Attitude Determination & Control System

In this section, we focus on the spacecraft attitude. The external disturbances introduced in section IV.1.4 affect both the attitude and the orbit of spacecrafts. Yet, I only consider their impact on the movement of the satellite around its center of inertia, hence the attitude. Considerations about the trajectory will be dealt with in section IV.2.

We are especially interested in the capacity of the ADCS to provide the expected pointing during orbital maneuvers. Therefore, I will only study the attitude control section of a typical ADCS loop, which is displayed in figure IV.1. That is to say that the attitude determination part of the ADCS is supposed to be ideal.

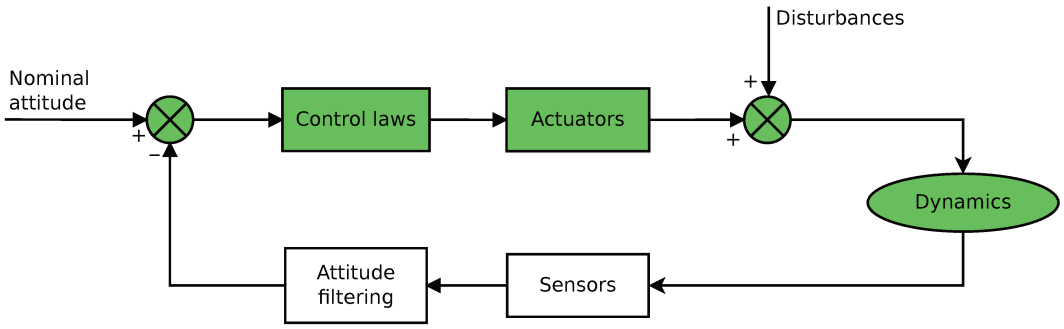

Figure IV.1: Attitude Determination & Control System (ADCS) loop. This work focuses on colored blocks, assuming that the attitude determination part is ideal.

IV.1.1 - Attitude Representation

Attitude representation is the first step in the development of an attitude control simulator. An introduction to two classical ways of defining frame orientation, namely the Direction Cosine Matrix (DCM) and Euler angles, is available in appendix A. In this thesis, I use quaternions instead. Although their mathematical approach is less intuitive, they convey the same information as DCM while avoiding ambiguities. Moreover, they do not suffer from singularities, contrary to Euler angles.

Quaternions, also called Euler parameters, are a popular and practical set of attitude coordinates [138]. They are based on the Euler theorem, which states that any displacement of a rigid body such that a point on the rigid body remains fixed is equivalent to a single rotation about some axis that runs through the fixed point. A quaternion is an element in $\mathbb{R}^4$ that is written

$$q = \begin{pmatrix} q_0 \\ q_1 \\ q_2 \\ q_3 \end{pmatrix} = \begin{pmatrix} \cos\frac{\theta}{2} \\ i\sin\frac{\theta}{2} \\ j\sin\frac{\theta}{2} \\ k\sin\frac{\theta}{2} \end{pmatrix} = \begin{pmatrix} q_0 \\ \mathbf{q}_{1:3} \end{pmatrix}, \tag{IV.1}$$

where (i, j, k) are the coordinates of the eigenvector from Euler's theorem. Hence, q_0 is the scalar part of the quaternion whereas $\mathbf{q}_{1:3}$ is its vector part. The product of basis elements is ruled by the Hamiltonian product

$$i^2 = j^2 = k^2 = ijk = -1. \tag{IV.2}$$

Quaternions are not unique and one can show that q and $-q$ represent the same rotation. Unit quaternions are of particular interest for rotations because their action on a vector will not modify the vector's length:

$$q_0^2 + q_1^2 + q_2^2 + q_3^2 = 1. \tag{IV.3}$$

This constraint describes a four-dimensional unit sphere. Working with quaternions requires to regularly re-normalize them because numerical errors tend to accumulate during computations.

We define two quaternions p and q, whose main properties are:

- Quaternion multiplication

$$pq = p_0 q_0 - \mathbf{p}_{1:3}\mathbf{q}_{1:3} + p_0\mathbf{q}_{1:3} + q_0\mathbf{p}_{1:3} + \mathbf{p}_{1:3} \times \mathbf{q}_{1:3}. \tag{IV.4}$$

  The quaternion multiplication may be written as the second quaternion multiplied by a quaternion in a matrix form

$$pq = \mathbf{Q}(p)q \quad \text{with} \quad \mathbf{Q}(p) = \begin{pmatrix} p_0 & -p_1 & -p_2 & -p_3 \\ p_1 & p_0 & -p_3 & p_2 \\ p_2 & p_3 & p_0 & -p_1 \\ p_3 & -p_2 & p_1 & p_0 \end{pmatrix}. \tag{IV.5}$$

- Complex conjugate of q, denoted $q*$, is defined as

$$q^* = \begin{pmatrix} q_0 \\ -\mathbf{q}_{1:3} \end{pmatrix}. \tag{IV.6}$$

- The norm of a quaternion, denoted $|q|$, is the scalar

$$|q| = \sqrt{q^* q}. \tag{IV.7}$$

- The inverse of a quaternion is

$$q^{-1} = \frac{q^*}{|q|^2}. \tag{IV.8}$$

- The derivative of a quaternion is the derivative of each of its components

$$\dot{q} = \begin{pmatrix} \dot{q}_0 \\ \dot{q}_1 \\ \dot{q}_2 \\ \dot{q}_3 \end{pmatrix}. \tag{IV.9}$$

For any unit quaternion, we now define the quaternion operator that transforms a vector $\mathbf{v}$ in $\mathbb{R}^3$ through an angle θ about an axis of rotation $\mathbf{e}$ (also called the sandwich product) by

$$L_q(\mathbf{v}) = q\mathbf{v}q^*. \tag{IV.10}$$

On the other hand, the operator

$$L_{q^*}(\mathbf{v}) = q^*\mathbf{v}q \tag{IV.11}$$

may be interpreted geometrically as a rotation of the coordinate frame through an angle θ about $\mathbf{e}$ as the axis while $\mathbf{v}$ is not rotated. It is equivalent as saying that the operator $L_{q^*}(\mathbf{v})$ rotates the vector $\mathbf{v}$ with respect to the coordinate frame through an angle $-\theta$ about $\mathbf{e}$. Last but not least, quaternions allow the composition of rotations and two successive rotations will be applied by the product of the corresponding quaternions.

IV.1.2 - Coordinate Systems

Determining the location and the attitude of a spacecraft requires to handle coordinate systems. In astronomy, an inertial coordinate system is a reference frame whose axes point towards distant and well-defined objects such as stars. Among popular celestial coordinate systems, one can mention equatorial coordinate systems, widely used to specify the positions of celestial objects. Such a coordinate system has the Earth equator as the reference plane. The J2000 equatorial system in particular, used in this work, is an equatorial coordinate system whose primary direction is fixed at a standard epoch defined as J2000.

Geocentric Coordinate Systems

Geocentric coordinate systems regroup all reference frames that have their origin at the center of the Earth. They will be used in our Earth orbiting spacecraft scenarios.

Geocentric inertial reference systems are named Earth-Centered Inertial (ECI). Such systems are popular because the equations of motion describing the position and attitude of celestial bodies are simpler in such non-rotating frames. A common set of axes has the z-axis pointing towards the north pole, the x-axis directed to the vernal point and the y-axis following the right-hand convention.

Many applications tend to represent orbital motions around the Earth in Earth-Centered Earth-Fixed (ECEF) reference frames. ECEF coordinate systems rotate relatively to ECI around the z-axis (pointing to the pole), with the x-axis constantly pointing to the Greenwich Meridian. The y-axis completes the orthogonal system. Both ECI and ECEF coordinate systems used in this work are shown in figure IV.2.

Two specific coordinate systems rotating with the Earth, cousins of the ECEF, are introduced to simulate the environment in Low Earth Orbit (LEO). On the one hand, the Latitude Longitude Altitude (LLA) is a spherical coordinate system with the usual definition of geographic latitude, longitude and altitude on a reference geoid. Here, I use the geoid defined by the WGS84 frame [139]. It is used to model the atmosphere of the Earth (see section IV.1.4.4 and appendix B.3). On the other hand, the North East Down (NED) coordinate frame is used to decompose the Earth magnetic field at a point in space (see figure IV.3). Indeed the routine presented in appendix B.1 provides northward, eastward and downward components of the magnetic field.

Orbital coordinate systems

Orbital frames relate to the orbit of the spacecraft. Their origin moves as the satellite orbits around the central body. Although many orbital frames exist, I will only introduce the "qsw" coordinate system, which is defined in such a way that the radial vector $\mathbf{q}$ is collinear to the geocentric position of the satellite, $\mathbf{w}$ is collinear to the orbital kinetic momentum thus normal to the orbit plane and $\mathbf{s}$ completes the right-handed triad of unit vectors (see figure IV.2).

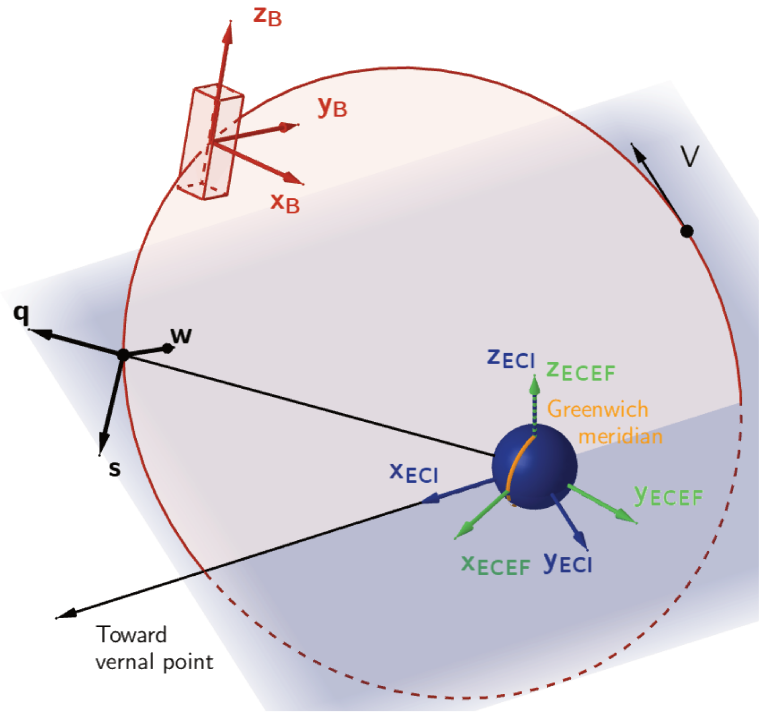

Figure IV.2: Schematic of main reference frames for Earth-orbiting satellites. The Earth-Centered Inertial (ECI), Earth-Centered Earth-Fixed (ECEF), body and "qsw" coordinate frames are in blue, green, red and black respectively. The equatorial plane is represented in blue, while the orbital plane is in red.

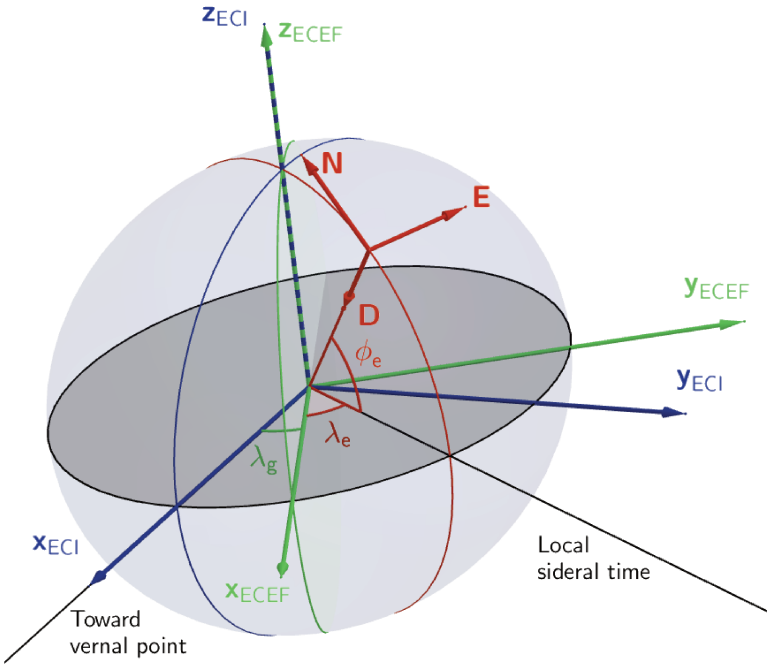

Figure IV.3: Schematic of the Earth-Centered Inertial (ECI) (blue), Earth-Centered Earth-Fixed (ECEF) (green) and North East Down (NED) (red) reference frames.

Body and Instrument-Fixed Coordinate Systems

A common body-fixed reference frame for CubeSats is introduced, with its origin placed at the COG of the satellite and the z-axis along the longitudinal axis (see figure IV.2). This frame is important to describe the attitude of the spacecraft with respect to other frames, such as the ECI coordinate systems. The inertia tensor of the satellite and the position of the various subsystems are usually given in the body-fixed coordinate system. Instrument-fixed coordinate systems are aligned following the characteristics of the instruments. They are generally defined with regard to the body frame.

IV.1.3 - Equations of Motion

The equations of motion, namely kinematic and dynamic equations, are the heart of any simulation of spacecraft attitude. In this section, we derive the mathematical model based on the quaternion as attitude representation, for the reasons mentioned in section IV.1.1.

The mapping from an angular velocity $\boldsymbol{\omega} = (\omega_1, \omega_2, \omega_3)^T$ to the quaternion rates is made feasible by the kinematic differential equation [140]

$$\dot{q} = \begin{pmatrix} \dot{q}_0 \\ \dot{q}_1 \\ \dot{q}_2 \\ \dot{q}_3 \end{pmatrix} = \frac{1}{2} \begin{pmatrix} 0 & -\omega_1 & -\omega_2 & -\omega_3 \\ \omega_1 & 0 & \omega_3 & -\omega_2 \\ \omega_2 & -\omega_3 & 0 & \omega_1 \\ \omega_3 & \omega_2 & -\omega_1 & 0 \end{pmatrix} \begin{pmatrix} q_0 \\ q_1 \\ q_2 \\ q_3 \end{pmatrix}. \tag{IV.12}$$

This equation can be rewritten in a more compact form:

$$\begin{cases} \dot{q}_0 = -\frac{1}{2}\mathbf{q}_{1:3}^T \boldsymbol{\omega}_b^{bi} \\ \dot{\mathbf{q}}_{1:3} = -\frac{1}{2}\boldsymbol{\omega}_b^{bi} \times \mathbf{q}_{1:3} + \frac{1}{2} q_0 \boldsymbol{\omega}_b^{bi}. \end{cases} \tag{IV.13}$$

Let us now focus on the dynamics relating the torques acting on the spacecraft to the rotational acceleration. The fundamental equation of a rotating body links the angular momentum $\mathbf{H}$ to the torques $\mathbf{T}$ applied to the satellite

$$\dot{\mathbf{H}} = \mathbf{T}. \tag{IV.14}$$

The torque vectors include both the disturbance torques and the control torques. Considering the angular velocity vector $\boldsymbol{\omega}$ and the inertia tensor $\mathbf{I}$, the angular momentum expression in the inertial frame is

$$\mathbf{H}_i = \mathbf{I}\boldsymbol{\omega}_i^{bi} + \mathbf{h}_i, \tag{IV.15}$$

where $\boldsymbol{\omega}_i^{bi}$ is the rotational velocity of the body frame with respect to the inertial frame, seen in the inertial frame. $\mathbf{h}$ is the angular momentum stored by any rotating object that is part of the spacecraft (such as internal moment exchange devices) and the inertia tensor is

$$\mathbf{I} = \begin{pmatrix} I_{xx} & -I_{xy} & -I_{xz} \\ -I_{yx} & I_{yy} & -I_{yz} \\ -I_{zx} & -I_{zy} & I_{zz} \end{pmatrix}. \tag{IV.16}$$

where

$$I_{xx} = \int \left(x^2 + y^2\right)\ dm, \qquad I_{yy} = \int \left(x^2 + z^2\right)\ dm, \qquad I_{xx} = \int \left(y^2 + z^2\right)\ dm, \tag{IV.17}$$

and

$$I_{xy} = I_{yx} = \int xy\ dm, \qquad I_{xz} = I_{zx} = \int xz\ dm, \qquad I_{yz} = I_{zy} = \int yz\ dm. \tag{IV.18}$$

Inserting equation IV.15 in equation IV.14 leads to the Euler equation

$$\mathbf{I}_i \dot{\boldsymbol{\omega}}_i^{bi} = \mathbf{T} - \dot{\mathbf{I}}_i \boldsymbol{\omega}_i^{bi} - \dot{\mathbf{h}}_i. \tag{IV.19}$$

From this equation, it is easy to read how satellites' attitude is modified as a function of different terms, herefrom the left to the right of the right-hand side:

- external torques,
- internal torques, due to on-board rotating objects, such as Reaction Wheel (RW),
- changes in the spacecraft moment of inertia, such as the decreasing amount of propellant.

Equation IV.19 is not optimal for solving the motion of the rotating spacecraft, since both the inertia tensor and the angular velocity vector can change during the motion. There are two reasons for the variations of the inertia tensor that we need to discard to facilitate the simulation. The first one is the modification of the mass distribution inside the satellite, for instance because of propellant consumption or sloshing. Hereafter, we consider that the mass distribution is fixed all along the simulation. Still, the tensor of inertia calculated in the inertial frame can change during the motion. Therefore, it is usual to express the Euler equation in the body-fixed reference frame (whose axes are aligned along the principal axes of rotation of the body). In this frame the inertia tensor is now constant.We now rewrite equation IV.14, using the transport theorem and the fact that the instantaneous angular velocity of the body frame with respect to the inertial frame is the same as that of the body:

$$\frac{^i d}{dt}(\mathbf{H}) = \frac{^b d}{dt}(\mathbf{H}) + \boldsymbol{\omega}_b^{bi} \times \mathbf{H}_b = \mathbf{T}, \tag{IV.20}$$

where $\boldsymbol{\omega}_b^{bi}$ is the rotational velocity of the body frame with respect to the inertial frame, seen in the body frame.Combining the angular momentum from equation IV.15 written in the body frame and equation IV.20 we obtain the Euler equation in the body-fixed reference frame

$$\mathbf{T} = \mathbf{I}_b \dot{\boldsymbol{\omega}}_b^{bi} + \boldsymbol{\omega}_b^{bi} \times \mathbf{I}_b \boldsymbol{\omega}_b^{bi} + \dot{\mathbf{h}}_b + \boldsymbol{\omega}_b^{bi} \times \mathbf{h}_b. \tag{IV.21}$$

Equation IV.21 is the nonlinear dynamic equation of motion for a rigid body with constant inertia. It is usual to rewrite this equation to express the rate of change of the angular velocity

$$\dot{\boldsymbol{\omega}} = \mathbf{I}^{-1} \left(-\boldsymbol{\omega} \times \mathbf{I}\boldsymbol{\omega} - \boldsymbol{\omega} \times \mathbf{h} - \dot{\mathbf{h}} + \mathbf{T}_c + \mathbf{T}_d \right), \tag{IV.22}$$

where the subscripts indicating that we are in the body reference frame have been dropped for clarity. Here, $-\dot{\mathbf{h}}$ is the control torque on the satellite produced by the RW, T_c regroups the control torques produced by other actuators such as propulsion systems and magnetorquers, and $\mathbf{T}_d$ are the torques due to disturbances.
The whole physical problem can be stated combining kinematic and dynamic equations (equation IV.12 and equation IV.22), leading to the general nonlinear model for the spacecraft

$$\frac{d}{dt} \begin{pmatrix} \boldsymbol{\omega} \\ q_0 \\ \mathbf{q}_{1:3} \\ \dot{\mathbf{h}} \end{pmatrix} = \begin{pmatrix} \mathbf{I}^{-1} \left(-\boldsymbol{\omega} \times \mathbf{I}\boldsymbol{\omega} - \boldsymbol{\omega} \times \mathbf{h} - \dot{\mathbf{h}} + \mathbf{T}_c + \mathbf{T}_d \right) \\ -\frac{1}{2} \boldsymbol{\omega}^T \mathbf{q}_{1:3} \\ -\frac{1}{2} \boldsymbol{\omega} \times \mathbf{q}_{1:3} + \frac{1}{2} q_0 \mathbf{I}\boldsymbol{\omega} \\ -\mathbf{T}_{RW} \end{pmatrix}. \tag{IV.23}$$

The reader must be aware that the spacecraft is supposed to be rigid, that is to say no flexibility is considered.

IV.1.4 - Disturbance Torques

Before getting to the presentation of the disturbances mentioned above, it is of interest to note that they can have various impacts, depending on the attitude of the satellite and the origin of the perturbation. On the one hand, effects that are null once averaged over an entire orbit are called cyclical. On the other hand, secular perturbations accumulate with time. Generally, perturbations are secular, which is problematic when RWs are used to manage the angular momentum because they tend to saturate.

IV.1.4.1 - Gravity Gradient

The gravity gradient results from the interaction between the gravitational field and a satellite of distributed mass. The closer satellite's part is to the attractive body, the stronger the gravitational acceleration is. This gradient causes a torque that disturbs the satellite's attitude but can also be used for passive control. Gravity gradient torque appears when the satellite's gravity center is not aligned with the center of mass regarding the local vertical. Figure IV.4 displays the geometry of the phenomenon. The gravity gradient torque can be defined by

$$\mathbf{T}_g = \int_b \mathbf{r}_b \times d\mathbf{F}_g, \tag{IV.24}$$

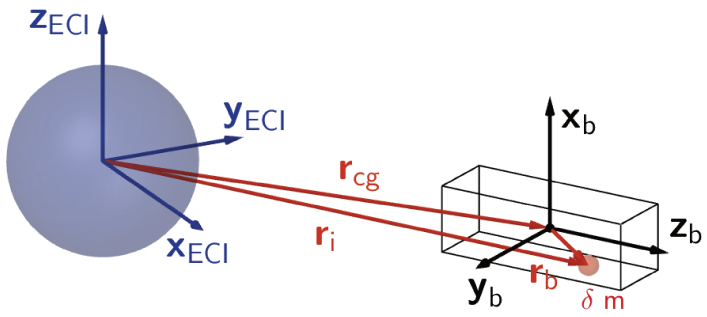

Figure IV.4: Gravity gradient torque geometry. The Earth-Centered Inertial (ECI) frame is represented in blue, while the body frame is in black. $\mathbf{r}_b$ is the position of the mass element in the body frame. $\mathbf{r}_{cg}$ and $\mathbf{r}_i$ are respectively the position vector of the gravity center and the position vector of the mass element dm, both expressed in the inertial frame.

where $\mathbf{r}_b$ is the position of the mass element in the body frame and $d\mathbf{F}_g$ is the gravitational force on the mass element dm calculated as

$$d\mathbf{F}_g = \frac{-GM}{|\mathbf{r}_i{}^3|}\mathbf{r}_i dm, \tag{IV.25}$$

where $G = 6.67 \times 10^{-11}\ \mathrm{m^3\,kg^{-1}\,s^{-2}}$ is the gravitational constant, M is the mass of the attractive body and $\mathbf{r}_i = \mathbf{r}_{cg} + \mathbf{r}_b$ is the position vector of the mass element dm in the inertial frame. Here, $\mathbf{r}_{cg}$ is the position vector of the gravity center in the inertial frame. Equation IV.24 can now be rewritten

$$\mathbf{T}_g \simeq \frac{3GM}{|\mathbf{r}_{cg}|^5}\mathbf{r}_{cg} \times (\mathbf{I}\mathbf{r}_{cg})\,. \tag{IV.26}$$

All the vectors from equation IV.26 are expressed in the body frame and so is the inertia tensor. Assuming that the body is rigid, the inertia tensor becomes constant in this frame. This equation tells us that the gravity torque direction is perpendicular to the radius vector and that it vanishes when one of the principal axes of inertia is aligned with this radius vector.

IV.1.4.2 - Magnetic Field

Some celestial bodies such as the Earth have magnetic fields powerful enough to induce noticeable effects in the surrounding space. Schematically, the Earth magnetic field can be seen as a dipole (figure IV.5). This field interacts with any other magnetic field that it encounters, which makes it very promising for attitude control with magnetorquers. As a matter of fact, artificial satellites have a certain amount of residual magnetic dipole moment that translates into a weak magnetic field. As a result, satellites act like magnetic dipoles because they carry current loops. A current of I amperes flowing in a planar loop of area A produces a dipole moment

$$\mathbf{m} = IA\hat{\mathbf{n}}_A. \tag{IV.27}$$

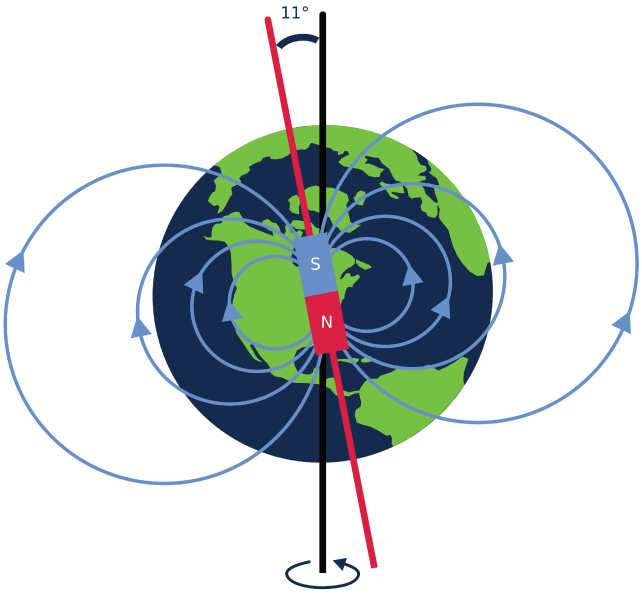

Figure IV.5: Earth magnetic field regarded as a magnetic dipole which axis is tilted by $\sim$ 11 deg with respect to the geographical north-south axis.

This dipole moment, expressed in $\mathrm{A\,m^2}$, is time-varying and aligned with the surface normal satisfying the right-hand rule $\hat{\mathbf{n}}_A$. Few CubeSat residual dipoles are available in the literature. The Dart 3U CubeSat residual dipole was characterized at NASA Goddard Spaceflight Center to be 9×10^{-3} $\mathrm{Am^2}$ [141], whereas the one of the PACE CubeSat was estimated to be 5×10^{-4} $\mathrm{Am^2}$ [131]. An estimation of the residual magnetic dipole moment per unit mass generated by on-board currents for classical satellites is proposed in [142]. Depending on the level of design, quality control, test and compensation, the residual moment may vary between 1×10^{-3} $\mathrm{Am^2/kg}$ and 10×10^{-3} $\mathrm{Am^2/kg}$.

The magnetic torque caused by the interaction of the local magnetic field B and the satellite's residual dipole is

$$\mathbf{T}_m = \mathbf{m} \times \mathbf{B}. \tag{IV.28}$$

In the case of the Earth magnetic field, a model for computing its local instant value and direction is presented in appendix B.1.

IV.1.4.3 - Radiation Pressure

There are two categories of radiative sources: primary sources and secondary sources. The Sun is the typical example of primary source. It emits not only photons, but also protons and electrons (solar wind) that interact with the spacecraft. Solar Radiation Pressure (SRP) is the principal source of disturbance for a spacecraft on an interplanetary trajectory. Extrasolar primary sources, such as cosmic rays, can be considered as negligible. Secondary sources, such as the Earth or the moon, are elements that reflect an incoming flux as a function of their albedo. Because the average Earth albedo is 0.3, it is only one order of magnitude smaller than the Sun,

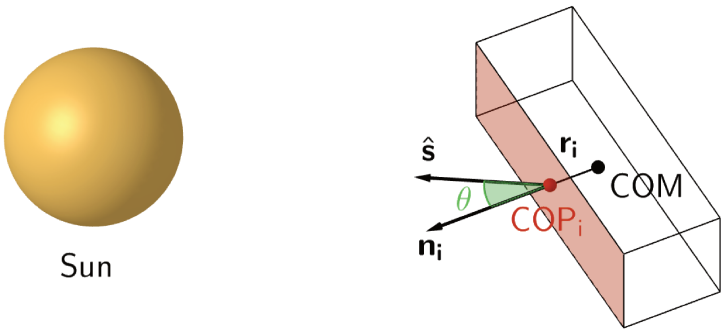

Figure IV.6: Solar Radiation Pressure (SRP) torque geometry. $\mathbf{n}_i$ is the normal vector of the i$^{\text{th}}$ plate, and COP_i is its Center Of Pressure. The Center Of Mass (COM) is indicated, together with the distance from the COM to the Center Of Pressure (COP) $\mathbf{r_i}$. Finally, $\hat{\mathbf{s}}$ is the unit vector from the COP to the Sun.

making it non-negligible for Earth-orbiting satellites requiring a fine pointing.

The interaction between the solar radiation and the surface of a spacecraft is modeled as a pressure exerted on the spacecraft. The geometry of the SRP is displayed in figure IV.6. The spacecraft is considered to be a collection of N plates of area S_j. Each plate has a normal vector $\mathbf{n}_i$ in the body frame and a radiation pressure coefficient c_R that lies between zero and one (usually $c_R = 0.6$ for small satellites). The spacecraft-to-Sun unit vector in the satellite reference frame is $\hat{\mathbf{s}}$ and the angle between this vector and the normal to the j$^{\text{th}}$ plate is the noted θ^i_{prs}. The force of solar radiation pressure that the Sun exerts of the j$^{\text{th}}$ plate is

$$\mathbf{F}^j_{srp} = -\mathbf{p}_{srp} c_R S_j \max\left(\cos\theta^j_{srp}; 0\right), \tag{IV.29}$$

where it has been assumed that the radiation pressure coefficient is uniform all over the spacecraft. This is a strong assumption motivated by the fact that we are not considering final designs in our work. The "max" function is here to discard unlit spacecraft surfaces. The radiation pressure vector $\mathbf{p}_{srp}$ is calculated from the solar constant

$$\mathbf{p}_{srp} = \frac{\phi_\odot}{c}\hat{\mathbf{s}}, \tag{IV.30}$$

where c is the speed of light in vacuum and $\phi_\odot$ is the solar irradiance which depends on the distance to the Sun. The mismatch between the positions of the Center Of Pressure (COP) and the Center Of Mass (COM) of the satellite results in a torque. Such a mismatch depends on the lit surfaces, on the incident angle of energetic rays, and on the mass distribution inside the satellite. Let $\mathbf{r}_j$ be the vector from the center of mass to the SRP center of the j$^{\text{th}}$ plate. The SRP torque acting on the satellite is expressed

$$\mathbf{T}_{srp} = \sum_{j=1}^{N} \mathbf{r}_j \times \mathbf{F}^j_{srp}. \tag{IV.31}$$

In order to simulate the SRP, one must not forget to consider the Earth shadowing. A simple model is proposed in appendix B.2.

IV.1.4.4 - Atmospheric Drag

The atmosphere of celestial bodies may be a dominant factor when it comes to orbiting on very low orbits. For instance, the atmospheric drag is the main disturbance that an Earth-orbiting satellite has to face when it is below 400 km. Similarly to the SRP, the force exerted by the atmospheric drag is computed considering that the spacecraft is made of N surfaces of area S_j. This force is a function of the relative velocity between the spacecraft and the atmosphere, which is given in the inertial frame by

$$\mathbf{v}_{rel}^{i} = \mathbf{v}_i - \boldsymbol{\omega}_{\oplus}^{i} \times \mathbf{r}_i, \tag{IV.32}$$

where $\mathbf{r}_i$ and $\mathbf{v}_i$ are respectively the position and velocity of the satellite in the inertial frame. Here, the Earth's angular velocity vector is $\boldsymbol{\omega}_{\oplus}^{i} = \omega_{\oplus}^{i}[0,0,1]^T$ with $\omega_{\oplus}^{i} = 7.27 \times 10^{-5}$ s. The equation in the body frame is easily obtained using the attitude matrix. Hereafter, the b index denotes the body frame and the j index will denote j$^{\text{th}}$ plate. The aerodynamic force acting on the j$^{\text{th}}$ plate is

$$\mathbf{F}_{aero}^{j} = -\frac{1}{2}\rho c_D S_j |\mathbf{v}_{rel}^{b}| \mathbf{v}_{rel^b} \max\left(\cos\theta_{aero}^{j}, 0\right), \tag{IV.33}$$

where ρ is the atmospheric density and c_D is the dimensionless drag coefficient. Surfaces that are not exposed to the atmospheric drag are discarded through the use of the "max" function with

$$\cos\theta_{aero}^{j} = \frac{\hat{\mathbf{n}}_j^b \cdot \mathbf{v}_{rel}^{b}}{|\mathbf{v}_{rel}^{b}|}, \tag{IV.34}$$

where $\hat{\mathbf{n}}_j^b$ is the normal unit vector to the j$^{\text{th}}$ plate. The total torque is finally obtained from equation IV.33, considering the vector from the center of mass to the center of aerodynamic pressure of the j$^{\text{th}}$ plate

$$\mathbf{T}_{aero} = \sum_{j=1}^{N} \mathbf{r}_i \times \mathbf{F}_{aero}^{j}. \tag{IV.35}$$

The complexity of this perturbation lies in the temporal variability of all the parameters. The atmospheric density ρ is obtained from models, one of them being introduced in appendix B.3. The drag coefficient c_D depends on the shape of the spacecraft, and the way molecules collide with it. It is determined empirically and a typical value of $c_D = 2.2$ is assumed for CubeSats [5]. Such a value is consistent with the $[2-4]$ boundaries proposed by Vallado [143]. Aerodynamic torques can be used both to passively and actively control the attitude, the latter requiring moving parts.

IV.1.5 - Actuators

The ADCS relies on actuators to produce the control torques, whose role is to compensate external disturbances, provide the expected pointing or spin, detumble the satellite, etc. Hereafter, we present the most used actuators on-board CubeSats: magnetorquers (MTQs) and reaction Wheels (RWs). We also briefly mention thrusters, because they have been extensively presented in section II.2.2.

IV.1.5.1 - Magnetorquers

Many CubeSats use MTQs, or magnetorquers, for controlling their attitude because they are very simple devices. MTQs create their own magnetic dipole that will interact with the local magnetic field, such as the Earth magnetic field (see appendix B.1), generating a torque. The principle is the same as for the disturbing magnetic torque that will be presented in section IV.1.4.2, except that the undesired residual magnetic dipole of the satellite in equation IV.28 is here replaced by the designed magnetic dipole of the actuator $\mathbf{m}_{MTQ}$

$$\mathbf{T}_{MTQ} = \mathbf{m}_{MTQ} \times \mathbf{B}, \tag{IV.36}$$

where $\mathbf{B}$ is the local magnetic field and $\mathbf{T}_{MTQ}$ is the control torque produced by the MTQs.

One can notice a main drawback of MTQs: the torque generated depends on the geometry of the local magnetic field. In other words, the torque will tend to align the magnetic moment created by the actuator with the local magnetic field.

MTQs are made of a coil in which a current is flown, generating a dipole moment that will interact with the ambient magnetic field. This means that it is possible to act on the generated torque in-orbit by modifying the quantity of current flowing in the coil. Their very straightforward design makes them cheap to produce and reliable in operations. In terms of system impact, they present the advantage of being lightweight and consume little electric power. They also provide continuous and smooth torque controls. The performance and characteristics of some available MTQs are displayed in table IV.1.

However, they also come with major drawbacks. We have seen that they rely on the ambient magnetic field to produce the control torque. As a result, the level of torque that they can produce is very low. Therefore, they have been used only in LEO where the Earth magnetic field is strong enough. Even if the satellite is in a strong ambient magnetic field, the magnetic torque vector always acts in the plane that is normal to the magnetic field vector. Consequently, at a specific location in space the achievable torques are limited. Last but not least, a good knowledge of the ambient magnetic field is necessary if one wants to obtain the correct control torque.

Table IV.1: Performance and characteristics of available magnetorquers (MTQs) for CubeSats.

Model	Control	Magnetic moment [A m^2]	Power [W]	Mass [kg]
ISIS Magnetorquer board [125]	motherboard, 3-axis control	0.2	1.2	0.196
NCTR-M002 [144]	one rod only, 1-axis control	0.2	0.2	0.03
SatBus MTQ [145]	motherboard, 3-axis control	0.2	0.550	0.200
NanoTorque GST-600 [146]	motherboard, 3-axis control	0.3	N/A	0.156

IV.1.5.2 - Reaction Wheels

Some devices are called momentum exchange devices. The total angular momentum of the body being preserved, momentum exchange devices transfer the angular momentum between different parts of the satellite thanks to rotating masses. RWs, momentum wheels and control moment gyros are momentum exchange devices. Because RWs are by far the most used momentum exchange device on-board CubeSats, this section will focus on them.

In general, RWs are recommended for accurate attitude control because they produce a small amount of parasite torques compared to other uators. They also generate torques several orders of magnitudes higher than MTQs and many propulsion systems (see table IV.2). They can store and distribute angular momentum. They are made of a mass rotating around an axis of rotation. If the rotation of the mass inside a RW is accelerated, this modifies the wheel's angular momentum, resulting in a torque $\mathbf{T}_{RW}$

$$\mathbf{T}_{RW} = \dot{\mathbf{h}}_{RW} = \frac{d}{dt}(\mathbf{I}_{RW}\boldsymbol{\omega}_{RW}), \tag{IV.37}$$

where $\mathbf{h}$ is the angular momentum stored by the RW, $\mathbf{I}_{RW}$ and $\boldsymbol{\omega}_{RW}$ are the inertia matrix and the angular velocity vector of the RW. Because the overall angular momentum of the spacecraft is conserved, a transfer of angular momentum between the RW and the rest of the satellite appears. This means that the control torque is opposite to the RW torque.

At least three RWs are required to fully control the attitude of a spacecraft. Such actuators are limited in terms of rotation speed. If the maximal rotation speed is reached, the wheel can only decelerate, hence producing a torque about its axis in the wrong direction. Another actuator is necessary to desaturate the RW, which means lowering its angular velocity to its normal operating range. MTQs and Attitude Control Thrusters (ACTs) are usually operated for wheel desaturation. The performance and characteristics of some available wheels are displayed in table IV.2.

Table IV.2: Performance and characteristics of available reaction wheels (RWs) for CubeSats.

Model	Control	Maximum torque [mN.m]	Power [W]	Mass [kg]
CubeWheel Small [124]	1-axis control	0.32	0.72	0.060
CubeWheel Medium [147]	1-axis control	1	1.5	0.130
CubeWheel Large [148]	1-axis control	2.3	2.2	0.200
NanoTorque GSW-600 [149]	1-axis control	2	2.5	0.180
SatBus 4RW0 [150]	1-axis control	3.2	3	0.137

IV.1.5.3 - Attitude Control Thrusters

As seen in section II.2.2, reaction jets are the main actuators for orbit control. While this work is mainly interested in the disturbances due to thrusters misalignment with the COM, it is also worthwhile to note that the torques created by thrusters are also used to control the attitude of the spacecraft. As a matter of fact, a single thruster producing the thrust vector $\mathbf{F}_{th}$ also generates a torque $\mathbf{T}_{th}$ about the COM of the spacecraft

$$\mathbf{T}_{th} = \mathbf{r} \times \mathbf{F}_{th}, \tag{IV.38}$$

where $\mathbf{r}$ is the position of the thruster in the body-fixed reference frame.

Compared to orbit control, the inverse drawback comes from using ACTs, that is to say that the orbit of the spacecraft is modified as a side effect. To solve this problem, ACTs can be positioned with opposite directions in order to cancel their action on the COM, hence generating pure torques. Otherwise, the same set of thrusters can be operated for both the attitude and orbit control of a spacecraft. This is the purpose of the configuration illustrating section IV.1.7. Such concepts are very promising for CubeSats, where volume and mass are very constrained.

IV.1.6 - Attitude Control Strategies

Control laws are an essential part of attitude control. Their purpose is to transform a difference between nominal and measured attitudes into commands for the actuators presented previously. Attitude control strategies not only vary from one spacecraft to another, they are also mode dependent. Hereafter, I introduce and develop three control strategies.

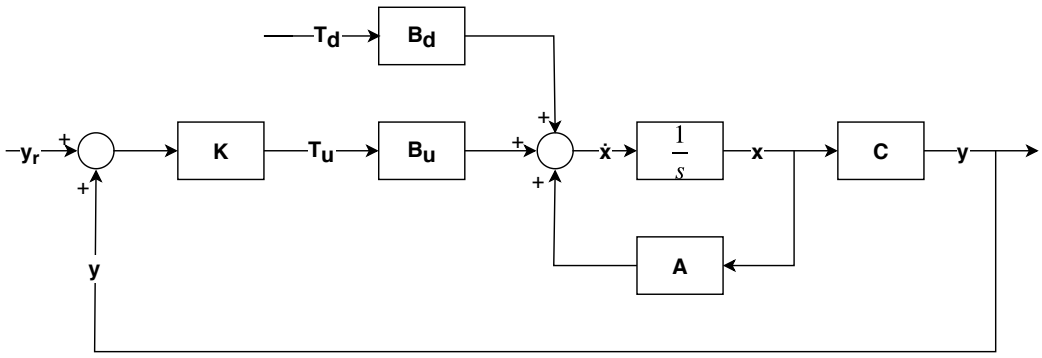

Figure IV.7: Block diagram representation of the closed control loop of the attitude of the spacecraft.

IV.1.6.1 - Control Law Using Quaternion Error

The objective of a control law is to make a measured value reach a reference one. The closed-loop control with output feedback presented in figure IV.7 is proposed. The reader should be reminded that our work is based on quaternions to represent rotations because it is common for real-time implementations.

Linearization of Attitude Control Model

Most physical systems are fundamentally nonlinear and so are the physical equations describing the attitude control of a spacecraft. Nonlinear controllers exist and can guarantee the global stability of the system as well as increase the control performance.

The behavior of a control system such as a spacecraft attitude control system is based on a feedback loop (see figure IV.7). Feedback loops are part of control theory, which is a strategy to select the most suitable input to a system so that its output is controlled. Attitude control loops shall produce a stable control of the spacecraft's attitude, based on operational constraints (response time, overshoot, etc.) and both external and internal perturbations. A feedback loop compares at each time step the measured state vector and the set state vector, then proposes controls that will reduce the gap between the two. An introduction to the mathematical tools used in this work regarding control theory is available in appendix C.1.

Automatic control theory can only provide analytical solutions for linear systems. However, attitude dynamic equations are generally second-order nonlinear equations. Therefore, equations have to be linearized to apply standard automatic control techniques. Usually, engineers define domains of linearity in which the plants[1] can be approximated by linear equations. Nonlinear attitude control can be based on passivity, sliding mode and feedback linearization. The objective is to linearize equation IV.23 around an arbitrary point of operation $\overline{\mathbf{x}} = (\overline{\boldsymbol{\omega}}, \overline{q}_0, \overline{\mathbf{q}}_{1:3}, \overline{\mathbf{h}})$ in order to perform stability and performance analysis. The nonlinear system shown in figure IV.7 can be expressed by

[1] In control theory, the plant is the combination of processes and actuators, and referred to with a transfer function.

$$\dot{\mathbf{x}}(t) = \mathbf{f}(\mathbf{x}(t), \mathbf{u}(t)), \tag{IV.39}$$

where $\mathbf{f}$ is expressed in equation IV.23 and recalled here,

$$\frac{d}{dt}\begin{pmatrix} \boldsymbol{\omega} \\ q_0 \\ \mathbf{q}_{1:3} \\ \dot{\mathbf{h}} \end{pmatrix} = \begin{pmatrix} \mathbf{I}^{-1}\left(-\boldsymbol{\omega} \times \mathbf{I}\boldsymbol{\omega} - \boldsymbol{\omega} \times \mathbf{h} - \dot{\mathbf{h}} + \mathbf{T}_c + \mathbf{T}_d\right) \\ -\frac{1}{2}\boldsymbol{\omega}^T \mathbf{q}_{1:3} \\ -\frac{1}{2}\boldsymbol{\omega} \times \mathbf{q}_{1:3} + \frac{1}{2} q_0 \mathbf{I}\boldsymbol{\omega} \\ -\mathbf{T}_{RW} \end{pmatrix}.$$

The deviation from steady state of the angular velocity and internal angular momentum are expressed by

$$\delta\boldsymbol{\omega} = \boldsymbol{\omega} - \overline{\boldsymbol{\omega}} \qquad , \qquad \delta\mathbf{h} = \mathbf{h} - \overline{\mathbf{h}}. \tag{IV.40}$$

The quaternion representation of attitude is more complicated and we need to linearize the kinematic equation (equation IV.13). We express the orientation at time $t + dt$ relative to the orientation at time t using equation IV.1

$$\delta q = \begin{pmatrix} dq_0 \\ dq_1 \\ dq_2 \\ dq_3 \end{pmatrix} = \begin{pmatrix} \cos\left(\frac{1}{2}\omega dt\right) \\ e_1 \sin\left(\frac{1}{2}\omega dt\right) \\ e_2 \sin\left(\frac{1}{2}\omega dt\right) \\ e_3 \sin\left(\frac{1}{2}\omega dt\right) \end{pmatrix} \simeq \begin{pmatrix} 1 \\ \frac{1}{2}\omega_1 dt \\ \frac{1}{2}\omega_2 dt \\ \frac{1}{2}\omega_3 dt \end{pmatrix}. \tag{IV.41}$$

It is now possible to linearize the kinematic equation (equation IV.13) for δq, noticing that $\frac{d}{dt} q_0 = 0$ and $\boldsymbol{\omega} \times \delta\mathbf{q}_{1:3} = 0$,

$$\frac{d}{dt}\delta q = \frac{d}{dt}\begin{pmatrix} \delta q_0 \\ \delta\mathbf{q}_{1:3} \end{pmatrix} = \begin{pmatrix} 0 \\ -\frac{1}{2}\boldsymbol{\omega} \times \delta\mathbf{q}_{1:3} + \frac{1}{2}\delta q_0 \mathbf{I}_{3\times 3} \end{pmatrix} = \begin{pmatrix} 0 \\ \frac{1}{2}\mathbf{I}_{3\times 3}\boldsymbol{\omega} \end{pmatrix}. \tag{IV.42}$$

Our final linearized model will have a state vector $\mathbf{x}$ of the form

$$\mathbf{x} = \begin{pmatrix} \delta\boldsymbol{\omega} \\ \delta\mathbf{q}_{1:3} \\ \mathbf{h} \end{pmatrix} \tag{IV.43}$$

and a control input $\mathbf{u} = \mathbf{T}_c$.

Equation IV.39 becomes the state-space equation

$$\dot{\mathbf{x}}(t) = \begin{pmatrix} \dot{\delta\boldsymbol{\omega}} \\ \dot{\delta q_0} \\ \dot{\delta\mathbf{q}}_{1:3} \\ \dot{\delta\mathbf{T}}_{RW} \end{pmatrix} = \mathbf{A}\mathbf{x}(t) + \mathbf{B}_u\mathbf{T}_c(t) + \mathbf{B}_d\mathbf{T}_d(t), \tag{IV.44}$$

where

$$\mathbf{x}(t) = \begin{pmatrix} \boldsymbol{\omega} \\ q_0 \\ \mathbf{q}_{1:3} \\ \mathbf{h} \end{pmatrix} \quad , \quad \mathbf{T}_c = (\mathbf{T}_{RW} \;\; \mathbf{T}_{PS} \;\; \mathbf{T}_{MTQ}) \,, \tag{IV.45}$$

and

$$\mathbf{A}_{ij} = \frac{\partial f_i}{\partial x_j} \quad , \quad \mathbf{B}_{u,ij} = \frac{\partial f_i}{\partial u_j}. \tag{IV.46}$$

Thanks to the Jacobian linearization described in appendix C.2, we can now linearize our system. Through symbolic manipulation, equation IV.46 becomes

$$\mathbf{A} = \begin{pmatrix} \mathbf{I}^{-1}\mathbf{A}_{\boldsymbol{\omega},\boldsymbol{\omega}} & \mathbf{0} & \mathbf{I}^{-1}\mathbf{A}_{\boldsymbol{\omega},\mathbf{h}} \\ \frac{1}{2}\mathbf{I}_{3\times 3} & \mathbf{0} & \mathbf{0} \\ \mathbf{0} & \mathbf{0} & \mathbf{0} \end{pmatrix}, \tag{IV.47a}$$

$$\mathbf{B}_u = \begin{pmatrix} \mathbf{I}^{-1} & \mathbf{I}^{-1} & \mathbf{I}^{-1} \\ \mathbf{0} & \mathbf{0} & \mathbf{0} \\ -\mathbf{I}_{3\times 3} & \mathbf{0} & \mathbf{0} \end{pmatrix}, \tag{IV.47b}$$

$$\mathbf{B}_d = \begin{pmatrix} \mathbf{I}^{-1} \\ \mathbf{0} \\ \mathbf{0} \end{pmatrix}, \tag{IV.47c}$$

where the columns of $\mathbf{A}_{\boldsymbol{\omega},\boldsymbol{\omega}}$ are

$$\mathbf{A}_{\boldsymbol{\omega},1} = \begin{pmatrix} \omega_2 I_{31} - \omega_3 I_{21} \\ -\omega_3 I_{11} - 2\omega_1 I_{31} - \omega_2 I_{32} + \omega_3 I_{33} + h_3 \\ 2\omega_1 I_{21} - \omega_2 I_{22} + \omega_3 I_{23} + \omega_2 I_{11} - h_2 \end{pmatrix}, \tag{IV.48a}$$

$$\mathbf{A}_{\boldsymbol{\omega},2} = \begin{pmatrix} \omega_1 I_{31} + 2\omega_2 I_{32} - \omega_3 I_{33} + \omega_3 I_{22} - h_3 \\ \omega_3 I_{12} - \omega_1 I_{32} \\ -\omega_1 I_{22} + \omega_1 I_{11} - 2\omega_2 I_{12} - \omega_3 I_{13} + h_1 \end{pmatrix}, \tag{IV.48b}$$

$$\mathbf{A}_{\boldsymbol{\omega},3} = \begin{pmatrix} -\omega_2 I_{33} - \omega_1 I_{21} + \omega_2 I_{22} - 2\omega_3 I_{23} + h_2 \\ -\omega_1 I_{11} + \omega_2 I_{12} + 2\omega_3 I_{13} + \omega_1 I_{33} - h_1 \\ \omega_1 I_{23} - \omega_2 I_{13} \end{pmatrix}, \tag{IV.48c}$$

and the expression of $\mathbf{A}_{\boldsymbol{\omega},\mathbf{h}}$ is

$$\mathbf{A}_{\boldsymbol{\omega},\mathbf{h}} = \begin{pmatrix} 0 & \omega_3 & -\omega_2 \\ -\omega_3 & 0 & \omega_1 \\ \omega_2 & -\omega_1 & 0 \end{pmatrix}. \tag{IV.49}$$

The attitude control state-space equation (equation IV.44) represents our linear model of the spacecraft attitude. Assuming that all the matrices are invariant, we have a Linear Time-Invariant (LTI) system (see appendix C.1.1). This model allows controller design as well as sensitivity analysis around specific points of operation.

Quaternion Feedback Regulator

This section is dedicated to the design of control laws based on the linearized model from section IV.1.6.1. Based on the book of Sidi [151], I use a Proportional Derivative (PD) quaternion error controller

$$\mathbf{u} = -\mathbf{K}_p \begin{pmatrix} q_{1e}q_{0e} \\ q_{2e}q_{0e} \\ q_{3e}q_{0e} \end{pmatrix} - \mathbf{K}_d \begin{pmatrix} \omega_{1e} \\ \omega_{2e} \\ \omega_{3e} \end{pmatrix}, \tag{IV.50}$$

where $\mathbf{K}_p$ and $\mathbf{K}_d$ are proportional and derivative gain matrices respectively, $\boldsymbol{\omega}_e$ is the angular velocity vector error and q_e is the error quaternion. Let q_s be the quaternion describing the rotation to go from inertial axes to satellite body coordinate system axes and q_t the rotation to go from inertial axes to the target coordinate system axes. The quaternion error in equation IV.50 is

$$\begin{pmatrix} q_{0e} \\ q_{1e} \\ q_{2e} \\ q_{3e} \end{pmatrix} = \begin{pmatrix} q_{0t} & q_{1t} & q_{2t} & q_{3t} \\ -q_{1t} & q_{0t} & q_{3t} & -q_{2t} \\ -q_{2t} & -q_{3t} & q_{0t} & q_{1t} \\ -q_{3t} & q_{2t} & -q_{1t} & q_{0t} \end{pmatrix} \begin{pmatrix} q_{0s} \\ q_{1s} \\ q_{2s} \\ q_{3s} \end{pmatrix} \tag{IV.51}$$

and the angular velocity vector error is

$$\boldsymbol{\omega}_e = \boldsymbol{\omega}_s - \boldsymbol{\omega}_t. \tag{IV.52}$$

The sign "$-$" in equation IV.50 differs from some identical controllers available in literature. This difference is compensated by the fact that the scalar part of q_s in equation IV.50 is positive.

Our goal is to set the two gain matrices $\mathbf{K}_p$ and $\mathbf{K}_d$ by using the linear model in equation IV.44. For small angles, and taking q_0 positive, the quaternion error q_e is

$$q_e \simeq \begin{pmatrix} 1 \\ q_{1s} - q_{1t} \\ q_{2s} - q_{2t} \\ q_{3s} - q_{3t} \end{pmatrix}. \tag{IV.53}$$

As $\mathbf{u}$ in equation IV.50 is the control torque $\mathbf{T}_c$, the equation can now be rewritten

$$\mathbf{T}_c = \begin{pmatrix} \mathbf{K}_d & \mathbf{K}_p \end{pmatrix} \begin{pmatrix} \omega_{1t} - \omega_{1s} \\ \omega_{2t} - \omega_{2s} \\ \omega_{3t} - \omega_{3s} \\ q_{1t} - q_{1s} \\ q_{2t} - q_{2s} \\ q_{3t} - q_{3s} \end{pmatrix} = \mathbf{K}(\mathbf{y}_t - \mathbf{y}), \tag{IV.54}$$

where the two gain matrices have been regrouped in the same matrix $\mathbf{K}$. $\mathbf{y}$ and $\mathbf{y}_t$ are the measured and reference vectors, respectively,

$$\mathbf{y} = \begin{pmatrix} \boldsymbol{\omega} \\ \mathbf{q}_{1:3} \end{pmatrix}, \tag{IV.55a}$$

$$\mathbf{y}_t = \begin{pmatrix} \boldsymbol{\omega}_t \\ \mathbf{q}_{1:3\ t} \end{pmatrix}. \tag{IV.55b}$$

They can be seen in figure IV.7, together with the state vector $\mathbf{x}$ introduced in equation IV.43.

All that is left to do is to identify the transfer function of our control loop, from the reference to the measured vector. To this end, we make use of the Laplace transform (see appendix C.1.2). The state vector is obtained from figure IV.7

$$\mathbf{x} = (s\mathbf{I}_{9\times 9} - \mathbf{A})^{-1}\,\mathbf{B}_u\mathbf{T}_c, \tag{IV.56}$$

where s is the complex frequency. Introducing equation IV.54 and noting that $\mathbf{y} = \mathbf{C}\mathbf{x}$ provides the transfer function

$$H(s) = \frac{\mathbf{y}(s)}{\mathbf{y}_t(s)} = \mathbf{C}\,(s\mathbf{I}_{9\times 9} - \mathbf{A} + \mathbf{B}_u\mathbf{K}\mathbf{C})^{-1}\,\mathbf{B}_u\mathbf{K}\mathbf{y}_r(s). \tag{IV.57}$$

It is possible to identify the terms of the transfer function by comparing it to the standard form in equation C.8. We define

$$\mathbf{A}_{cl} = \mathbf{A} - \mathbf{B}_u\mathbf{K}\mathbf{C}, \tag{IV.58a}$$

$$\mathbf{B}_{cl} = \mathbf{B}_u\mathbf{K}, \tag{IV.58b}$$

$$\mathbf{C}_{cl} = \mathbf{C}, \tag{IV.58c}$$

$$\mathbf{D}_{cl} = \mathbf{0}_{6\times 6}. \tag{IV.58d}$$

Hence, the transfer function is

$$H(s) = \mathbf{C}_{cl}(s\mathbf{I} - \mathbf{A}_{cl})^{-1}\mathbf{B}_{cl} + \mathbf{D}_{cl} \tag{IV.59}$$

For a realistic system, the closed-loop system is unstable when its transfer function H has poles in the complex right half-plane. A closed-loop stability analysis therefore boils down to determining where the poles are located.

IV.1.6.2 - Momentum Dumping Using Magnetorquers

Attitude control with RWs requires excess momentum management from other actuators. This is called momentum dumping. MTQs are often used for this task in LEO, especially on CubeSats. Indeed, small platforms (few CubeSat units) make it very complicated to carry and power both RWs and ACTs, not to mention that several of them are needed for 3-axis attitude control.

We consider the excess momentum $\Delta\mathbf{h} = \mathbf{h} - \mathbf{h}_{nom}$, where $\mathbf{h}$ is the momentum vector of the RW and $\mathbf{h}_{nom}$ is its expected nominal momentum vector. A basic control law proposed in Sidi [151] is

$$\mathbf{T} = -k_u \Delta \mathbf{h}, \tag{IV.60}$$

where k_u is called the unloading control gain. Inserting equation IV.60 in IV.36 yields

$$-k_u \Delta \mathbf{h} = \mathbf{m}_{MTQ} \times \mathbf{B}. \tag{IV.61}$$

The same problem arises once again with MTQs, that is to say the impossibility to dump the momentum in the direction parallel to the local magnetic field. The following strategy is adopted. We apply the cross product of $\mathbf{B}$ on both sides of equation IV.61

$$\mathbf{B} \times (-k_u \Delta \mathbf{h}) = \mathbf{B}^2 \mathbf{m}_{MTQ} - \mathbf{B}(\mathbf{m}_{MTQ} \cdot \mathbf{B}). \tag{IV.62}$$

We now suppose that the applied magnetic moment is perpendicular to the ambient magnetic field; hence equation IV.62 simplifies to

$$\mathbf{m}_{MTQ} = -\frac{k_u}{B^2}(\mathbf{B} \times \Delta \mathbf{h}). \tag{IV.63}$$

One can see that this control magnetic moment is not proportional to the excess momentum. Indeed, the torque produced is

$$\mathbf{T} = -\frac{k_u}{B^2}\left(\mathbf{B}^2 \Delta \mathbf{h} - \mathbf{B}(\mathbf{B} \cdot \Delta \mathbf{h})\right). \tag{IV.64}$$

IV.1.6.3 - $\dot{\mathbf{B}}$-Controller

The detumbling controller is in charge of canceling the current tumbling of a satellite. It is usually operated to slow down the unknown initial spin of a satellite due to its separation from the launcher. The $\dot{\mathbf{B}}$-controller in particular is very robust and has been successfully operated in orbits on both classic satellites and CubeSats.

Disturbance torques play a marginal role during detumbling; therefore they are neglected. The variation of the magnetic field in the body frame is due to two separate movements:

- the rotation of the body frame relative to the inertial frame,
- the position of the satellite in space, which is related to the orbital change of the local magnetic field.

When detumbling, it is assumed that the first term prevails. It means that the rotational frequency is supposed to be higher than the orbital frequency. The controller can then despin the spacecraft relative to the magnetic field down to the rate of change of the ambient magnetic field.

The $\dot{\mathbf{B}}$-controller is used for satellites with MTQs and magnetometers. The information from magnetometers is directly used to control the MTQs. Although the instantaneous information given by a magnetometer is irrelevant in this case, the time derivative of the measurements is directly proportional to the rate of change of the satellite's attitude. Therefore, generating magnetic torques proportional to

the derivative of the magnetic field is common practice. In that sense, the following magnetic control moment is proposed

$$\mathbf{m}_{MTQ} = -K\dot{\mathbf{B}}, \tag{IV.65}$$

where K is a positive gain factor and $\dot{\mathbf{B}}$ is the rate of change of the local magnetic field. The resulting torque is then

$$\mathbf{T}_{MTQ} = -K\dot{\mathbf{B}} \times \mathbf{B}. \tag{IV.66}$$

An easier control method, based on the bang-bang logic, consists in using the maximum MTQ capacity $\mathbf{m}_{max}$. It can be stated as

$$\mathbf{m}_{MTQ} = -\mathbf{m}_{max}\ \text{sign}\left(\dot{\mathbf{B}}\right). \tag{IV.67}$$

RWs and ACTs can also be used to despin the satellite. As such, they need information from gyrometers to monitor the current rotation velocity. Although magnetometers could be used as in the $\dot{\text{B}}$ control, satellites carrying RWs or ACTs usually fly with gyrometers.

IV.1.7 - Command Distribution to Actuators

The control laws defined in section IV.1.6 generate control commands in the body-fixed reference frame without considering the geometry of the actuators. How the control torque must be distributed to the actuators is addressed in this section. This last step consists in adapting the command in the body frame to a command for each actuator expected to control the spacecraft's attitude.

We are only interested in command distribution to sets of identical actuators, this means only RWs, MTQs or ACTs. Indeed, we consider that for a specific attitude control mode only a set of the same type of actuators is used.

IV.1.7.1 - Command Distribution to Reaction Wheels

Let us consider the case where three RWs are positioned with their axis of rotation in random directions. If the torques delivered by the wheels are called T_i $(i = 1, ..., 3)$, they can be obtained from the torque command $\mathbf{T}_c$ through a body-to-wheel transformation matrix

$$\begin{pmatrix} T_1 \\ T_2 \\ T_3 \end{pmatrix} = \begin{pmatrix} \mathbf{e}_{RW_1} \cdot \mathbf{e}_{b_1} & \mathbf{e}_{RW_2} \cdot \mathbf{e}_{b_1} & \mathbf{e}_{RW_3} \cdot \mathbf{e}_{b_1} \\ \mathbf{e}_{RW_1} \cdot \mathbf{e}_{b_2} & \mathbf{e}_{RW_2} \cdot \mathbf{e}_{b_2} & \mathbf{e}_{RW_3} \cdot \mathbf{e}_{b_2} \\ \mathbf{e}_{RW_1} \cdot \mathbf{e}_{b_3} & \mathbf{e}_{RW_2} \cdot \mathbf{e}_{b_3} & \mathbf{e}_{RW_3} \cdot \mathbf{e}_{b_3} \end{pmatrix} \begin{pmatrix} T_{c_x} \\ T_{c_y} \\ T_{c_z} \end{pmatrix}. \tag{IV.68}$$

When a 3-axis attitude control is required, the simplest configuration is three RWs with each one's rotational axis parallel to a body axis. However, any failure would be fatal for the AOCS. For this reason, a fourth RW is usually added, whose axis is not collinear with any of the others. In this way, this new RW can provide small torques about any one of the body axis, allowing the replacement of the first three RW in case of malfunction. For instance, a pyramidal configuration of four

RW that can fit in half a CubeSat unit is developed by NanoAvionics [150]. Because of the lack of space, such a redundancy is rarely possible on CubeSats.

If a RW is not aligned with a body axis, a projection of its angular momentum in the body reference frame is necessary. Let $\mathbf{C}_{bw}$ be the transform matrix transforming the wheel momentum vector along the wheel axes $\mathbf{h}_{RW}^{w}$ to the total wheel momentum $\mathbf{h}_{RW}^{b}$ along the body axes:

$$\mathbf{h}_{RW}^{b} = \mathbf{C}_{bw}\mathbf{h}_{RW}^{w}. \tag{IV.69}$$

Reversing equation IV.69 requires to inverse the transformation matrix $\mathbf{C}_{bw}$. Unfortunately, if there are more or less than three reaction wheels on-board, this matrix is rectangular $(3 \times n_{RW})$ and its pseudo-inverse is

$$\mathbf{C}_{bw}^{+} = \mathbf{C}_{bw}^{T}\left(\mathbf{C}_{bw}\mathbf{C}_{bw}^{T}\right)^{-1}, \tag{IV.70}$$

where we assume that the inverse of matrix $\mathbf{C}_{bw}\mathbf{C}_{bw}^{T}$ exists in the considered applications. For instance, it would not exist for a configuration where all the RWs would be located at the same position and with the same orientation, which would correspond to an error of configuration.

The expected rate of change of the RW angular momentum $\dot{\mathbf{h}}_{RW}^{w}$ is expressed from the known control torque $\mathbf{T}_c$ using the pseudo-inverse matrix from IV.70

$$\dot{\mathbf{h}}_{RW}^{w} = -\mathbf{C}_{bw}^{+}\mathbf{T}_c. \tag{IV.71}$$

IV.1.7.2 - Command Distribution to Thrusters

The command distribution to thrusters follows the same logic as with RWs. In this simulation, its implementation with ACTs is based on the book of Sidi [151]. To present how it works, we need to consider a given configuration. Hence, we will use a configuration proposed to provide both attitude and orbit control, displayed in figure IV.8.

The torques produced by the various thrusters Th_i in the body reference frame $\mathbf{T}_{th}$ can be expressed as [151]

$$\mathbf{T}_{th} = \begin{pmatrix} (Th_3 + Th_4 - Th_1 - Th_2)\, G_x \\ (Th_2 + Th_3 - Th_1 - Th_4)\, G_y \\ (Th_2 + Th_4 - Th_1 - Th_3)\, G_z \end{pmatrix}, \tag{IV.72}$$

where G_i is the torque constant defined by the thrust level F and the torque arm r_i, with $i = (x, y, z)$. The normalized torques are

$$\hat{T}_i = \frac{T_i}{G_i}. \tag{IV.73}$$

Regrouping equation IV.72 and equation IV.73 gives

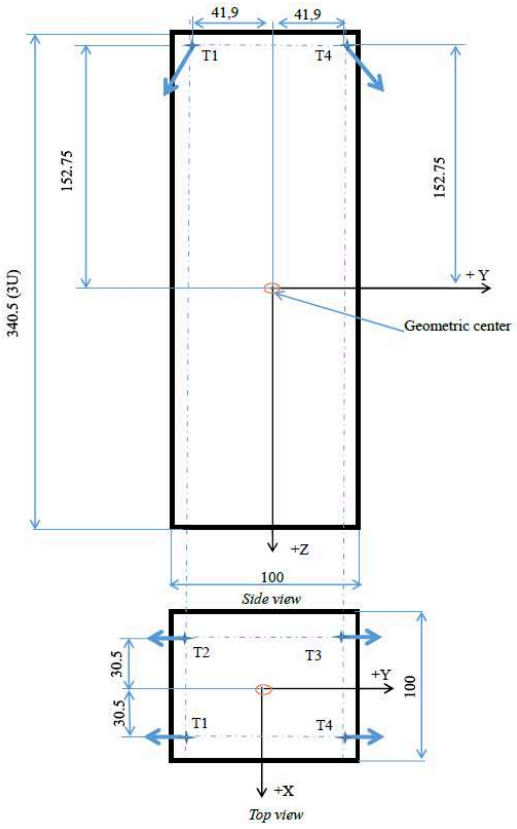

Figure IV.8: Schematic of a 4-thruster configuration on a 3U CubeSat. The blue arrows represent the thrusts that apply to the CubeSat.

$$\hat{\mathbf{T}} = \begin{pmatrix} -1 & -1 & 1 & 1 \\ -1 & 1 & 1 & -1 \\ -1 & 1 & -1 & 1 \end{pmatrix} \begin{pmatrix} Th_1 \\ Th_2 \\ Th_3 \\ Th_4 \end{pmatrix}. \tag{IV.74}$$

As in section IV.1.7.1, the pseudo-inverse matrix is requested, leading to

$$\begin{pmatrix} Th_1 \\ Th_2 \\ Th_3 \\ Th_4 \end{pmatrix} = \frac{1}{4} \begin{pmatrix} -1 & -1 & -1 \\ -1 & 1 & 1 \\ 1 & 1 & -1 \\ 1 & -1 & 1 \end{pmatrix} \hat{\mathbf{T}}. \tag{IV.75}$$

To ensure the positivity of the command (i.e., a thruster can produce a torque only in one direction), one must add an arbitrary vector in the null space of the pseudo-inverse matrix [152].

The use of equation IV.75 ensures that the thrusters corresponding to the maximum maneuver efficiency will be fired.

IV.1.7.3 - Command Distribution to Magnetorquers

As explained in section IV.1.5.1, the CubeSat can only be controlled in the planes perpendicular to the ambient magnetic field at a specific time due to the geometry of the magnetic torque. Hence, the spacecraft is underactuated. During the orbit, the axis of underactuation varies following the Earth magnetic field. If at a specific time the angular momentum of the spacecraft is controllable in only two directions, at the end of one orbit all the directions will have been controllable at some point.

Similarly to the method presented in section IV.1.6.2, a procedure for calculating the best magnetic moments from the required vector torque and the surrounding magnetic field is proposed in [153]

$$\mathbf{m}_{best} = \frac{\mathbf{B} \times \mathbf{T}_c}{B^2}. \tag{IV.76}$$

IV.2 - Guidance Navigation & Control

Now that attitude control simulation environment is introduced, we shift our attention to orbit control. The trajectory of a spacecraft is controlled by the GNC subsystem. It is in charge of determining the position, computing the trajectory maneuver and realizing it. In our scientific cases, the IFOD is responsible for the first step and a control logic on-board the satellite will have to compute the required maneuver given the current position and the expected one. Then, the on-board propulsion provides the orbital thrust.

When it comes to the Earth-orbiting scenarios proposed in section III.5, we can imagine that less autonomy is necessary and that commands are computed by the ground segment and sent to the satellite. Hence, the GNC is composed of a ground segment part, hereafter simulated by the trajectory solver, and the flight segment made of the on-board propulsion system that produces the required thrust.

IV.2.1 - Trajectory Solvers

Solving trajectories is a common task in GNC theory. The purpose of our trajectory solver is to compute a trajectory optimizing the duration and propellant consumption, to go from an initial orbit to a final one. These two parameters are the translation of the propulsion system's thrust force and specific impulse into mission drivers.

A natural approximation for trajectory solving is to consider instantaneous maneuvers. A famous case is the Hohmann transfer orbit between two circular orbits [154], proposed by Walter Hohmann in 1925. This approximation does not hold when the thrust of the propulsion system is too weak, which is generally the case with electric thrusters. Hence, one has to compute continuous thrust profiles that optimize performance parameters. Various methods exist in the case of long-term low-thrust transfers around a central body [155]. Among them, one could men-

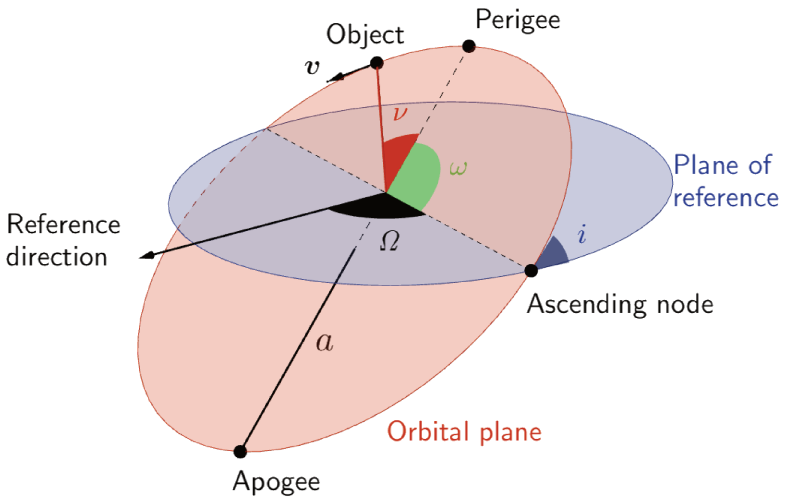

Figure IV.9: Classical Orbital Elements (COEs) for an object orbiting around a central body: semi-major axis (a), eccentricity (e), inclination (i), right ascension of the ascending node (Ω), argument of perigee (ω), and true anomaly (ν). The plane of reference and the orbital plane are represented, respectively in blue and orange.

tion direct, indirect, shooting or collocation methods. However, analytic methods, in particular based on the two-body problem, are easy to implement and realistic enough so as not to affect our conclusions on the on-board system.

Fundamental in astrodynamics, the two-body problem goes back to the 17^{th} century and the works of Kepler and Newton. Kepler's laws of planetary motion describe the movement of planets, and the simplest way to solve them involves Classical Orbital Elements (COEs). COEs form a set of parameters necessary to uniquely define a position in orbit. Different sets exist, but I will stick to the six Keplerian elements $(a, e, i, \Omega, \omega, \nu)$, respectively semi-major axis, eccentricity, inclination, right ascension of ascending node, argument of perigee and true anomaly (see figure IV.9).

Orbit modifications in terms of COEs have been studied thoroughly since the beginning of electric propulsion. Edelbaum derived analytic expressions for low-thrust maneuvers on inclined and quasi-circular orbits as early as 1961 [156]. A reformulation of Edelbaum's equations within the framework of optimal control theory led to new control laws for such orbits, which can easily be implemented [157], but do not cover a large spectrum of orbital maneuvers. Instead, I will use the Gauss expression of Lagrange Planetary Equations that expand the spectrum [158, 159].

IV.2.2 - Perturbed Two-body Problem

Here is the theory behind the trajectory solver that I have implemented for this work [160, 161]. First, we define the state vector of six COEs. The purpose is to determine the thrust direction maximizing the modification of each COE at each time step (elementary maneuvers). Because one may want to avoid thrusting when the maneuver is less efficient, hence saving propellant mass, the solver needs to compute the efficiency of those elementary maneuvers. Finally, a weighted sum of

elementary maneuvers over the COEs that need to be modified is performed. As a result, the user will get sets of thrust directions and efficiencies corresponding to elementary maneuvers. The trajectory solver is detailed hereafter.

IV.2.2.1 - Modifying One Classical Orbital Element

Using the Lagrange Planetary Equations, the two-body problem, modified with the addition of a disruptive acceleration $\mathbf{f}$, is solved

$$\frac{da}{dt} = \frac{2a^2}{h}\left(e\ \sin\ \nu\ f_q + \frac{p}{r}f_s\right), \tag{IV.77a}$$

$$\frac{de}{dt} = \frac{1}{h}\left(p\ \sin\ \nu f_q + \left((p+r)\cos\ \nu + re\right) f_s\right), \tag{IV.77b}$$

$$\frac{di}{dt} = \frac{r\ \cos(\nu+\omega)}{h} f_w, \tag{IV.77c}$$

$$\frac{d\Omega}{dt} = \frac{r\ \sin(\nu+\omega)}{h\ \sin\ i} f_w, \tag{IV.77d}$$

$$\frac{d\omega}{dt} = \frac{1}{he}\left(-pf_q\ \cos\ \nu + (p+r)f_s\ \sin\ \nu\right), \tag{IV.77e}$$

$$- \frac{r\ \sin(\nu+\omega)}{h\ \sin\ i}\cos\ i\ f_w,$$

$$\frac{d\nu}{dt} = \frac{h}{r^2} + \frac{1}{eh}\left(p\ \cos\ \nu\ f_q - (p+r)\ \sin\ \nu\ f_s\right), \tag{IV.77f}$$

where h is the specific orbital angular momentum, p is the semilatus rectum and r is the radial distance from the central body. The thrust acceleration vector is given in the body-fixed "qsw" reference frame. This reference frame is defined in such a way that the radial vector $\mathbf{q}$ is collinear with the geocentric position of the satellite, $\mathbf{w}$ is collinear with the orbital kinetic momentum thus normal to the orbit plane and $\mathbf{s}$ completes the right-handed triad of unit vectors. This reference frame is represented in figure IV.2, together with other usual reference frames. The expression of the acceleration is

$$f_q = |\mathbf{f}|\cos\beta_{qsw}\ \sin\alpha_{qsw} \tag{IV.78a}$$

$$f_s = |\mathbf{f}|\cos\beta_{qsw}\ \cos\alpha_{qsw} \tag{IV.78b}$$

$$f_w = |\mathbf{f}|\sin\beta_{qsw}. \tag{IV.78c}$$

The thrust direction maximizing the Rate Of Change (ROC) of each COE is found by setting to zero the partial derivatives of equation IV.77. An efficiency parameter measuring the efficiency of the thrust is now derived, in order to allow the propulsion system to thrust only at efficient locations [159, 160]. This parameter η_{COE} is the ratio between the instantaneous ROC of a specific COE and the maximum obtainable COE variation

$$\eta^i = \frac{dCOE^i}{dt} \Big/ \left.\frac{dCOE^i}{dt}\right|_{\max}. \tag{IV.79}$$

Similarly to the thrust angles, the location on the orbit providing the maximum ROC in a COE is obtained by taking the partial derivatives of Eq IV.77 with respect to the true anomaly, considering the optimal thrust angles found previously.

One can now produce a thrust profile that optimizes the maneuver efficiency. All one needs to do is to set an efficiency threshold. A trade-off between maneuver duration and propellant consumption must be found on a case-by-case basis. However, equation IV.79 falls short of taking into account the range of efficiency values during a maneuver. Therefore, another method to appraise the efficiency is proposed in [161]. In what follows, I have decided to modify this method by using the cumulative distribution function of the maneuver efficiency over the current osculating orbit. Hence, the cumulative distribution function of $\eta_{COE}(\nu)$ over one orbit is estimated at the current true longitude using the probability P

$$w_{eff}^{i} = \mathrm{P}\left(\eta_{COE}^{i}(\nu) \leqslant \eta_{COE}^{i}\right). \tag{IV.80}$$

IV.2.2.2 - Modifying Several Classical Orbital Elements

All that is left is managing the cases where more than one COE has to be modified between the initial and targeted state vectors. We will show how the optimal acceleration vector is obtained by applying a couple of weightings. The first weighting is the maneuver efficiency presented earlier and the second is dedicated to appraise where the satellite stands in the correction of a specific COE. Therefore, it is based on the relative value of a COE compared to its starting and targeted values, respectively COE_0 and COE_f

$$w_{pos}^{i} = \frac{COE_f^i - COE^i}{|COE_f^i - COE_0^i|}. \tag{IV.81}$$

The resulting optimal thrusting vector can now be determined by summing the weighed thrust vectors corresponding to the COEs that need to be modified. We get

$$\mathbf{T} = \sum_{i=1}^{N} w_{eff}^{i} w_{pos}^{i} \mathbf{T}^{i}, \tag{IV.82}$$

where N is the number of COEs that are being modified, $\mathbf{T}^i$ is the optimal thrusting vector for the modification of each COE and $\mathbf{T}$ is the resulting thrust vector. The in-plane and out-of-plane angles of thrust, respectively α_{qsw} and β_{qsw}, are then extracted from this vector

$$\alpha_{qsw} = \arctan\left(\frac{\mathbf{T}_q}{\mathbf{T}_s}\right), \tag{IV.83a}$$

$$\beta_{qsw} = \arctan\left(\frac{\mathbf{T}_w}{\sqrt{{\mathbf{T}_q}^2 + {\mathbf{T}_c}^2}}\right). \tag{IV.83b}$$

A comparison of this trajectory optimizer with other methods presented in [155] is available in [161] and confirms its relevance.

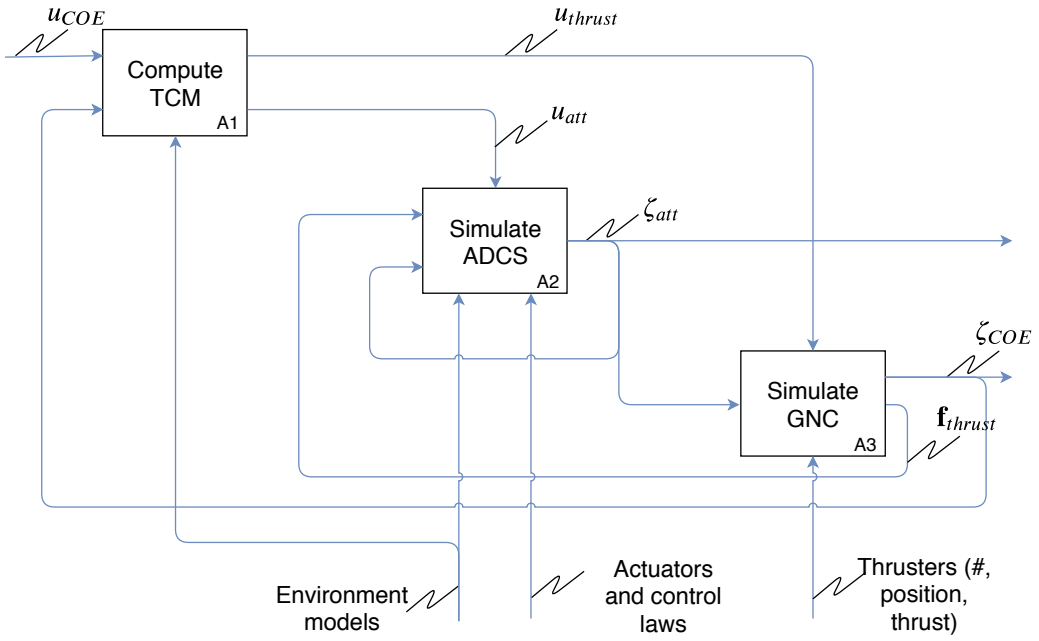

Figure IV.10: Structured Analysis & Design Technique (SADT) representation of the attitude and orbit simulation environment. The block A_1 represents the maneuver computation on the ground. It is executed once per orbit, determining the optimal thrust direction for the whole osculating orbit. Blocks A_2 and A_3 represent the flight system part.

IV.3 - Attitude & Orbit Control System

The Structured Analysis & Design Technique (SADT) is used to depict the whole simulation. The first level is represented in figure IV.10, including the on-ground computation of the TCM law, the ADCS and the on-board GNC blocks. Here, we consider that the ground segment computes and sends commands for TCM, including the necessary pointing and thrust profile. Similarly, our TCM control block determines in advance the thrust profile and direction for a certain duration (typically once per orbit), following the logic in section IV.2.1. Attitude and thrust profiles are instructions sent to the ADCS and on-board GNC. Sensors and filters are not simulated in this work and are therefore replaced by a unitary gain.

The attitude control block provides an attitude, based on the command and its own actuators and control law, and feeds the GNC block that propagates the orbit according to the commanded thrust profile and the provided attitude. The thrust produced by the GNC is an input of the ADCS to simulate the perturbation due to alignment errors.

CHAPTER V

Application to Relevant Cases

The simulation environment detailed in section IV is now used to investigate the mission scenarios presented in section III.5, and recalled here:

- deorbiting from a Low Earth Orbit (LEO),
- escaping the Earth attraction from a Geostationary Transfer Orbit (GTO).

V.1 - Attitude & Orbit Control Coupling in Earth Orbit

The two case studies representative of contexts requiring orbit control in Earth orbit with CubeSats will allow us to feed our analysis about the importance of mutual impacts between Attitude Determination & Control System (ADCS) and Guidance Navigation & Control (GNC) at CubeSat scale. The study proposed in this section comes from Quinsac et al. [162], a manuscript submitted for publication.

First, the common Commercial Off-The-Shelf (COTS) approach is applied to identify actuators compliant with the proposed mission concepts. An analytic trajectory solver (see section IV.2.1) provides idealistic mission-level performance indexes typical of what can be found in the literature. Its purpose is to compute a trajectory optimizing the duration and propellant consumption, to go from an initial orbit to a final one. These two parameters will be the mission drivers in our case studies. Then, we use the Attitude & Orbit Control System (AOCS) simulation (see section IV.3), gathering the trajectory solver and the attitude control simulation, in order to obtain more realistic indexes. The results are compared with those obtained while ignoring ADCS requirements during thrust maneuvers.

Table V.1: Performance of the propulsion systems selected in the two fictional case studies in Earth orbit. The first two are dedicated to orbital maneuvers, whereas the Cold Gas Thruster (CGT) is used for Reaction Wheel (RW) desaturation in our second case study (see section IV.1).

Manufacturer	Model	Dry mass [kg]	Power [W]	Thrust [mN]	I_{sp} [s]
Mars Space Ltd.	PPTCUP	0.280	5	0.09	670
Accion Systems	TILE 5000	1.10	30	1.5	1,500
N/A	CGT	0.5	< 4	1	60

V.1.1 - Proposed Configurations

In both our case studies starting in Earth orbit, electric thrusters are required because of the high I_{sp} that the missions require. In the deorbiting case, I decide to use a Pulsed Plasma Thruster (PPT) to provide orbital maneuvers. PPTs are electromagnetic propulsion systems presented in detail in section II.2.2. They are made of two electrodes positioned close to a fuel source, usually solid teflon. Hence, only one vector of thrust is available per thruster. This means that several thrusters should be placed in various directions if one wants to provide attitude control. PPTs are popular electric thrusters because of their relative simplicity and low power consumption, even though they have low thrust. High ΔV maneuvers, such as the one in our second case study, require even more propellant-efficient thrusters in order to fit in the spacecraft, as well as higher thrust for the maneuver duration to remain feasible in the span of the CubeSat lifetime. Very few systems meet those two conditions, as explained in section II.3.3. The TILE 5000 electrospray thruster[1] designed by Accion Systems is considered. Once again, no attitude control is possible with one TILE 5000 thruster. Indeed, this technology relies on a conductive propellant stored in a tank set to a high voltage when firing. Performance of the propulsion systems selected for our two case studies are detailed in table V.1.

In terms of power, a common practice is to assess the Orbit Average Power (OAP). To a first approximation, 60 % of the available peak power can be taken (see section III.2.1.3). Considering that a 3U CubeSat with body-mounted solar panels collects a maximum of 10 W in LEO, the PPT selected for the deorbiting mission complies with the available power. The Earth escape scenario, based on the electrospray thruster, is more complicated. Here, I select the lowest proposed point of operation, which corresponds to 30 W. Yet, such a power demand can hardly be provided by a 3U platform. Hence, a 6U CubeSat with deployable solar panels is proposed. The mass of solar panels needed to continuously provide the 30 W of power that the propulsion system requires can be calculated thanks to the mass-to-power ratio α_{pow}. At the moment, COTS deployable solar panels have $\alpha_{pow} \simeq 22$ kg kW^{-1} [163].

Both cases will rely on three Reaction Wheels (RWs) to provide the main attitude control during orbital maneuvers. The RWs are positioned to provide pure torques about each axis of the spacecraft. Although a pyramidal configuration of four RWs if

[1]The data sheet used for this work [120] is no longer available.

Table V.2: Selected actuators (see section IV.1.5) for the fictional case studies in Earth orbit. The Reaction Wheels (RWs) are used in both our case studies, whereas the Magnetic TorQuer (MTQ) and Cold Gas Thruster (CGT) perform Reaction Wheel (RW) desaturation in the first and second case respectively.

Model	Control	Magnetic moment [A m^2]	Maximum torque [mN m]	Power [W]	Mass [kg]
ISIS Magnetorquer board	motherboard, 3-axis control	0.2	~ 0.001 at 780 km	2	0.196
CubeWheel Small	1-axis control per RW	N/A	0.23	0.72	0.060
CubeWheel Medium	1-axis control per RW	N/A	1	1.5	0.130
CubeWheel Large	1-axis control per RW	N/A	2.3	2.2	0.200
CGT	3-axis control	N/A	~ 0.1	< 4	0.500 (dry)

often preferred, it is not considered in this work for simplicity reasons. RWs tend to saturate by reaching their maximal rotation speed, making it impossible to provide any further torque in the saturated direction. Because of the unavoidable misalignment of the principal motor mentioned earlier, RWs desaturation will periodically be required during a long Trajectory Correction Maneuver (TCM), increasing the maneuver duration. Selected COTS are presented in table V.2.

For RWs desaturation, other actuators shall provide momentum dumping. This is the role of magnetorquers (MTQs) or Attitude Control Thrusters (ACTs). Regarding MTQs, they are available for our case study in LEO, but not for the escaping case study. Indeed, the Earth magnetic field is too weak for the most part of the orbit. Furthermore, MTQs can only control the spacecraft in the plan perpendicular to the ambient magnetic field at a given moment, which, together with their low torque capability, will result in lengthy desaturations. Many off-the-shelf MTQs are available for CubeSats. The selected one is presented in table V.2.

Reaction jets are used as ACTs to off-load the RWs in the second case study. A simple Cold Gas Thruster (CGT) is simulated, made of six thrusters placed at one extremity of the CubeSat and directed as in figure V.1. This configuration is inspired by Nehrenz and Sorgenfrei [164]. The performance of this CGT, representative of identified devices in section II.3.1.1, is displayed in table V.1.

In the next sections, the AOCS simulation presented in section IV.3 is operated to investigate our deorbiting and Earth escaping CubeSats.

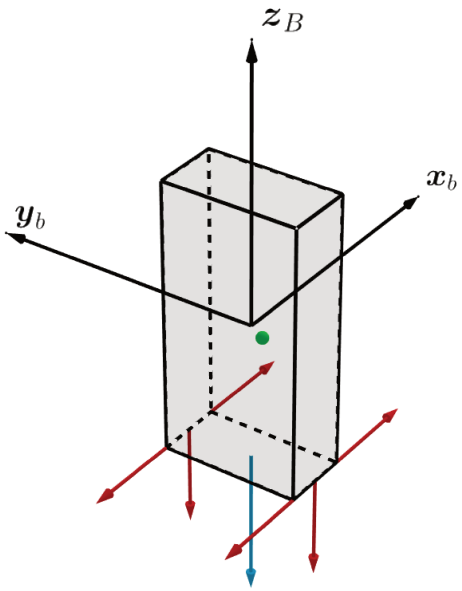

Figure V.1: Schematic of the 6U CubeSat configuration with two propulsion systems. The six thrust directions of the Cold Gas Thruster (CGT) are in red, and the orbital thrust vector is in blue. An example of Center Of Mass (COM) offset is represented in green.

Table V.3: Classical Orbital Elements (COEs) of the initial and targeted orbits in the deorbiting case.

Orbit	a [km]	e	i [°]	Ω [°]	ω [°]
Initial	7,151	0.000,1	98	0.000,1	0.000,1
Target	7,151	0.027,3	98	0.000,1	0.000,1

V.1.2 - Simulation of the Deorbiting Scenario

We now focus on the deorbiting case. The maneuver aims to decrease the perigee of the orbit down to 400 km, where it is expected that the satellite will naturally deorbit through atmospheric drag in less than 25 years. The state vectors of the initial and target orbits are available in table V.3.

V.1.2.1 - Ideal Maneuver

An ideal deorbitation maneuver is computed thanks to the trajectory solver introduced in section IV.2.1, resulting in 67 days of operation and 131.6 $\mathrm{m\,s^{-1}}$ of total ΔV. This has been obtained considering a continuous thrust even when the satellite is in the umbra of the Earth. However, it is unrealistic to consider that the 3U CubeSat will have sufficient batteries to power the propulsion system during eclipses. As soon as we impose the thrust to occur only when the satellite is on the sunlit side, the duration increases up to 89.2 days. The trajectory is visible in figure V.2.

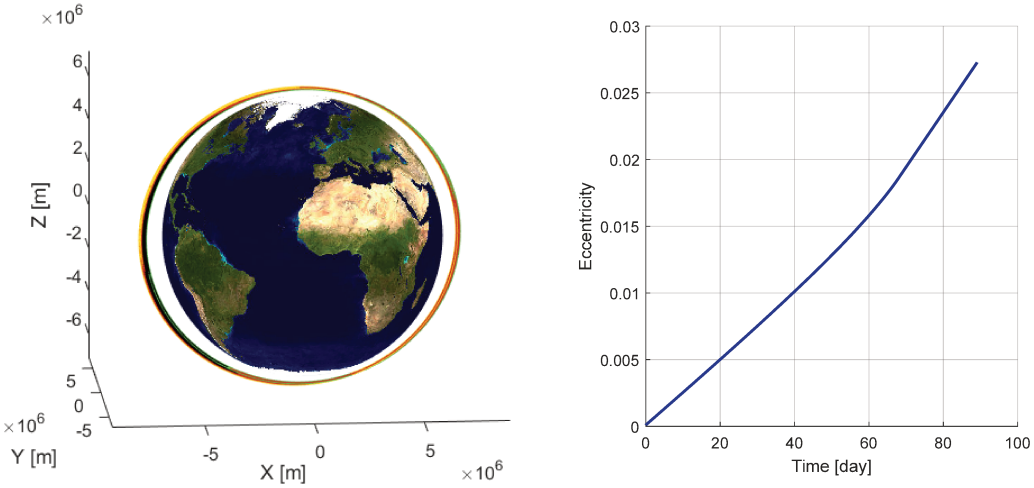

(a) Trajectory around the Earth. **(b)** Evolution of the eccentricity.

Figure V.2: Ideal maneuver in the deorbiting case. Thrusting and coasting phases due to Earth shadowing are in red and black respectively, while the initial and final orbits are in green and yellow.

The two previous durations were obtained considering that the thrust direction is recomputed at each time step. Yet, in the trajectory solver introduced in section IV.2.1, I consider that the required orbital maneuver is computed in advance by the ground segment. Once per orbit, the required thrust is computed for the whole current osculating orbit, which cannot be ideal because it omits the modification of the orbit due to the thrust. In order to tell the difference between the impact of this non-instantaneous maneuver computation and the inclusion of the ADCS performance, we simulate the TCM with in-advance orbital command computation and a perfect ADCS yet again. The maneuver takes 20 more days because of the non-optimal command. The reference for the design of the ADCS should then be $\sim$ 110 days.

V.1.2.2 - Realistic Maneuvers

Simulations are finally performed introducing the attitude control required during the orbital maneuver with the simulation environment from section IV.3. The orbital propulsion system is located at one extremity of the 3U CubeSat, with his thrust vector perfectly aligned with the Center Of Mass (COM) of the spacecraft. Three cases are processed, highlighting the necessity to consider the interactions between the GNC and the ADCS:

- Optimistic case: thanks to a careful integration, the COM is located within a circle of 5 mm radius in the transverse axes. Three CubeWheel Medium RWs are dedicated to the attitude control during the maneuver and are desaturated by three MTQs. The total mass of the RWs (390 g) and their maximum total power consumption (4.5 W) make their use very optimistic. In particular, 9.5 W are required to operate both the RWs and the PPT during orbital

Table V.4: CubeSat parameters in the deorbiting case study.

Parameter	Value		
Initial spacecraft mass [kg]	4		
Initial inertia matrix [kg m^{-1}]	$\begin{pmatrix} 33.3 & 0 & 0 \\ 0 & 33.3 & 0 \\ 0 & 0 & 6.67 \end{pmatrix} \cdot 10^{-3}$		
Residual magnetic dipole [A m^2]	$4 \cdot 10^{-4}$		
PD gains	$K_p = \begin{pmatrix} 33.3 \\ 33.3 \\ 6.67 \end{pmatrix} \cdot 10^{-5}$,	$K_d = \begin{pmatrix} 20.0 \\ 20.0 \\ 4.0 \end{pmatrix} \cdot 10^{-3}$	
Momentum dumping gain	$k_u = 5 \cdot 10^{-3}$		
	Optimistic	*Realistic*	*Worst*
COM position [m]	$\begin{pmatrix} 3.6 \\ 3.6 \\ 3.6 \end{pmatrix} \cdot 10^{-3}$	$\begin{pmatrix} 10 \\ -8 \\ 10 \end{pmatrix} \cdot 10^{-3}$	$\begin{pmatrix} 20 \\ -20 \\ -70 \end{pmatrix} \cdot 10^{-3}$

maneuvers, which may be considered as unfeasible.

- Realistic case: typical uncertainties during the integration and vibrations during the launch phase have resulted in a COM 10 mm and 8 mm off the COM. This time, three CubeWheel Small RWs are considered, because they are more adapted to the limitations of a 3U CubeSat. The same set of MTQs is used.
- Pessimistic case: the satellite designer has chosen to simply respect the limits imposed by the CubeSat Design Specification (CDS), that is to say 20 mm in the transverse axes. The attitude actuators of the realistic case are kept.

The parameters used for this simulation are summed up in table V.4, while the attitude actuators' performance are listed in table V.2. The gains used in these simulations were selected using the logic presented in sections IV.1.6.1 and IV.1.6.2. The results of the simulations are displayed in table V.5 and discussed in section V.1.4.

Table V.5: Maneuver duration and propellant consumption in the six scenarios of the deorbiting case study.

Scenarios	Duration [day]	m_p [g]
Ideal - w/o eclipse	67.0	79.0
Ideal - w/ eclipse	89.2	82.0
Reference	109.7	84.8
Optimistic	110.5	85.0
Realistic	162.8	86.0
Pessimistic	355.7	93.6

Table V.6: Classical Orbital Elements (COEs) of the initial and targeted orbits in the escaping case study.

Orbit	a [km]	e	i [°]	Ω [°]	ω [°]
Initial	24,630	0.716	7	170	178
Target	323,050	0.716	7	170	178

V.1.3 - Simulation of the Escaping Scenario

An Earth escape scenario is now investigated, with a 6U CubeSat deployed in a GTO inspired by the Ariane 5 (Janin 1997[2]). As a criterion, we choose that the spacecraft is said to be interplanetary as soon as the semi-major axis of its orbit reaches the first Earth-Moon Lagrange point (table V.6). The propulsion solution TILE 5000 from Accion Systems is selected to provide the orbital thrust required to perform the maneuver (table V.1). Deployable solar panels are mandatory to provide the 30 W this propulsion system needs in addition to the power used by the other subsystems. Yet, I neglect their impact on the inertia matrix.

V.1.3.1 - Ideal Maneuver

The same ideal maneuvers, with and without thrusting during eclipses, are simulated once again. As a result, 1.53 kg of propellant is required to perform the 175 day maneuver. As seen in section V.1.2, the in-advance computation of the thrust profile by the trajectory solver for the next orbit causes a small increase of the duration and the propellant consumed, still due to the progressive shift between the osculating orbit that the thrust profile is calculated on and the modified one. It follows that the impact of the imperfect ADCS should be compared to this reference.

Because the initial orbit is highly elliptical, the efficiency of the semi-major axis modification is varying along the orbit. Therefore, we test ideal maneuvers with various efficiency thresholds for the trajectory solver (see section IV.2.1). The results displayed in figure V.4 clearly show that increasing the efficiency threshold

[2]We could not access the resource.

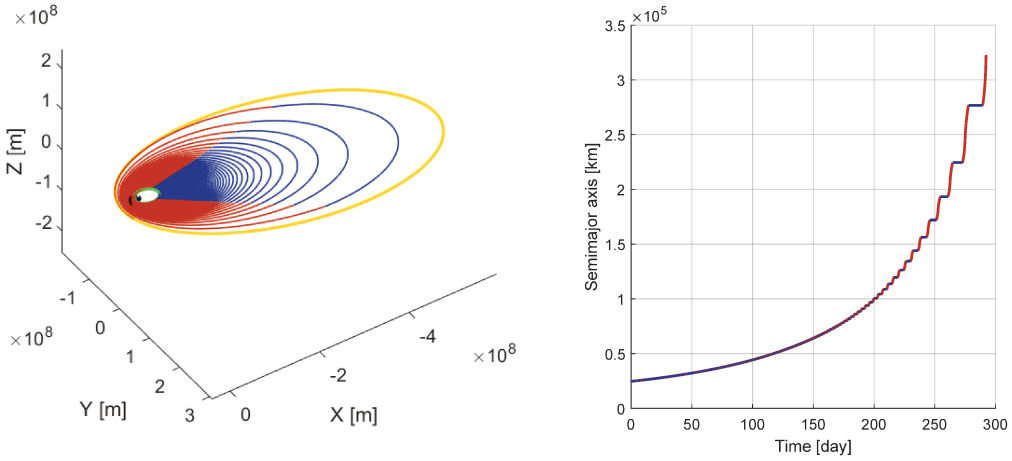

(a) Trajectory around the Earth.

(b) Evolution of the semi-major axis.

Figure V.3: Ideal maneuver in the Earth escape case. An efficiency threshold of 12.5 % was set (see section IV.2.1). Thrusting phases are in red, coasting phases due to Earth shadowing are in black, coasting phases when the instantaneous orbital maneuver efficiency is below 12.5 % are in blue. Initial and final orbits are in green and yellow respectively.

allows reducing the propellant required to perform the maneuver, at the expense of the duration. Figure V.3 shows an ideal trajectory with an efficiency threshold set to 12.5 %. In what follows, we will first run simulations of continuous thrust when the satellite is on the sunlit side (corresponding to an efficiency threshold of 0), and then an alternation of thrusting and coasting arcs based on the instantaneous maneuver efficiency threshold of 12.5 %.

V.1.3.2 - Realistic Maneuvers

Similarly to the deorbiting context, three variants are proposed for the inclusion of the ADCS to our Earth escape scenario.

- Optimistic case: inspired by the strong requirement imposed in the D-Sat mission, I propose an offset of the COM of 1.5 mm in all three axes. The thrust direction is ensured by three CubeWheel Large RWs that will be desaturated by a cold gas thruster, both presented in section IV.1.
- Realistic: the same COM position and RWs as in the optimistic deorbiting case are simulated, still desaturated by the CGT.
- Pessimistic: the center of mass is now shifted to 6 mm and 5 mm in the transverse axes, and 10 mm in the longitudinal one. The attitude actuators of the realistic case are considered.

The simulation parameters are regrouped in table V.7, while table V.8 gathers

the duration and the propellant consumed by both the orbital electrospray thruster and the attitude control CGT for all the scenarios.

V.1.4 - Lessons Learned

In this section, we examine what we have learned from the two hypothetical case studies. The deorbiting scenario highlights the important increase in terms of maneuver duration as soon as a realistic set of attitude actuators is considered. This increase in time is due to the necessary desaturation of the RWs from time to time. Yet, the orbital propulsion only delivers 90 µN, which does not produce a large amount of disturbance torque. In the case I consider to be very optimistic, the duration of the maneuver is only marginally increased and the increase can be considered negligible during the early phases of a mission design. In the more realistic case, in particular with smaller RWs, the duration increases by almost 50 %. When the CDS constraints are taken as requirements for the location of the COM, the duration skyrockets to 355 days, representing an increase of $\sim$ 225 %. Such a difference between the idealistic maneuver and the more realistic ones means that the CubeSat may cease working properly before it successfully performed its end-of-life maneuver.

In the second case study, from GTO to Earth escape, the impact of the propulsion system on the ADCS is measured in terms of mass. Indeed, the more the RWs have to compensate thruster disturbance torques, the more the cold gas ACTs must offload them and the more propellant they need. In return, the more propellant mass has been used by the ACTs, the less the CubeSat weights, reducing the amount of propellant needed by the orbital thruster. Obviously, this feedback effect should not be seen as beneficial. As a matter of fact, the mission designer must focus on reducing the propellant mass required by the propulsion system with the smallest I_{sp}, here by far the CGT. The total propellant mass consumed in the various scenarios of our Earth escape study is displayed in figure V.5. The total mass of propellant required to perform the maneuver is increased by $\sim$ 35 %, $\sim$ 90 % and $\sim$ 140 % in our optimistic, realistic and pessimistic scenarios, respectively (compared to the reference). Yet, the COM mismatches with the COG remain very small and hard to respect on a CubeSat platform. Summing up the 2.5kg of propellant in the realistic case (with 12.5 % efficiency), the dry masses of both the propellant systems, the RWs, the dedicated solar panels and all the other vital subsystems, such a mission might already be unfeasible. Also, from figures V.4 and V.5, one can see that the propellant saved selecting efficient places to perform the orbital maneuvers is about 20 %.

These results suggest that there is more to be gained in terms of mass in minimizing the mutual impacts of the GNC and the ADCS than in selecting the most favorable periods for performing the orbital maneuver. Obviously, this only applies for large enough integration uncertainties (although we have seen that they are quite small in the proposed configurations) and for reasonable maneuver duration (the more selective we are on the efficiency of the orbital maneuver, the longer the maneuver lasts as seen in figure V.4).

In both cases, a non-negligible increase related to the in-advance computation of

Table V.7: CubeSat parameters in the escaping case study.

Parameter	Value		
Initial spacecraft mass [kg]	4		
Initial inertia matrix [kg m^{-1}]	$\begin{pmatrix} 33.3 & 0 & 0 \\ 0 & 33.3 & 0 \\ 0 & 0 & 6.67 \end{pmatrix} \cdot 10^{-3}$		
PD gains	$K_p = \begin{pmatrix} 43.3 \\ 33.3 \\ 16.7 \end{pmatrix} \cdot 10^{-5}$	$K_d = \begin{pmatrix} 26.0 \\ 20.0 \\ 10.0 \end{pmatrix} \cdot 10^{-3}$	
Momentum dumping gain	$k_u = 5 \cdot 10^{-3}$		
	Optimistic	*Realistic*	*Worst*
COM position [m]	$\begin{pmatrix} 1.5 \\ 1.5 \\ -1.5 \end{pmatrix} \cdot 10^{-3}$	$\begin{pmatrix} 3.6 \\ 3.6 \\ 3.6 \end{pmatrix} \cdot 10^{-3}$	$\begin{pmatrix} 6 \\ -5 \\ -10 \end{pmatrix} \cdot 10^{-3}$

Table V.8: Maneuver duration and propellant consumption in all the variants of the escaping case study.

Case	Efficiency [%]	Duration [day]	$m_{p,\mathrm{OCT}}$ [kg]	$m_{p,\mathrm{ACT}}$ [kg]
Ideal - w/o eclipse	0	173.5	1.53	N/A
Ideal - w/ eclipse	0	176.6	1.53	N/A
Reference	0	187.8	1.61	N/A
Optimistic	0	193.0	1.54	0.63
Realistic	0	199.1	1.42	1.60
Pessimistic	0	201.5	1.32	2.53
Ideal - w/o eclipse	12.5	293.6	1.16	N/A
Ideal - w/ eclipse	12.5	290.5	1.16	N/A
Ideal - in-advance	12.5	324.2	1.34	N/A
Optimistic	12.5	308.9	1.27	0.54
Realistic	12.5	315.9	1.18	1.33
Pessimistic	12.5	335.7	1.10	2.12

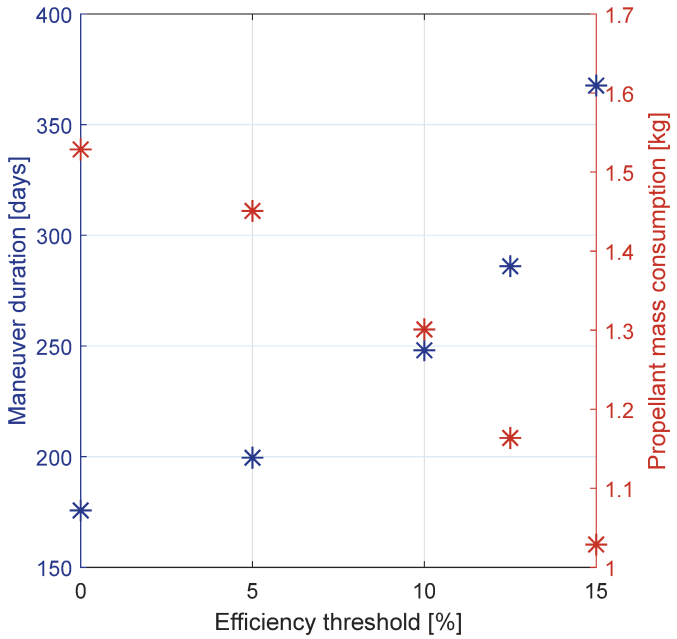

Figure V.4: Propellant consumption and maneuver duration for various efficiency thresholds and an ideal Attitude Determination & Control System (ADCS) in the Earth escape case. Maneuvers are only performed when the instantaneous efficiency (see section IV.2.1) is higher than the threshold.

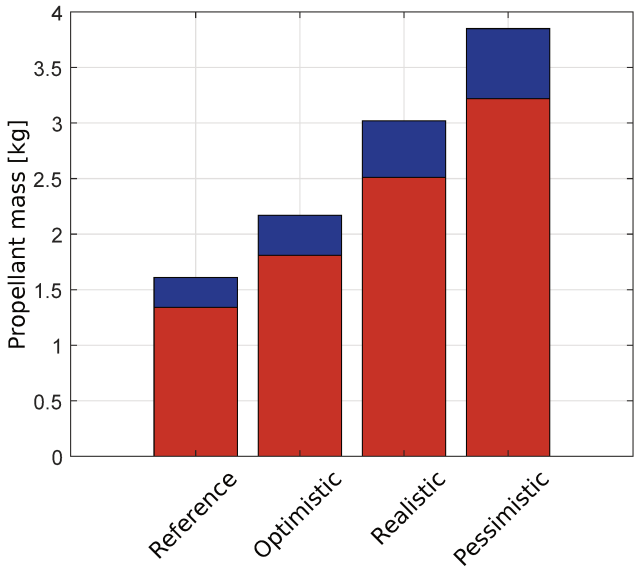

Figure V.5: Total propellant required by Guidance Navigation & Control (GNC) and Attitude Determination & Control System (ADCS) for the completion of the Earth escape in all the scenarios with in-advance thrust profile calculation. Blue bars refer to simulations with thrusting all along the orbit (except in shadow regions) and red bars refer to simulations where only the most efficient regions are selected for performing the orbital maneuver (efficiency threshold at 12.5 %).

the orbital thrust profile was also observed.

Let us now review the limits of our approach. First of all, one can see that the attitude determination part of the ADCS was not simulated. It is expected that its impact is within the uncertainties of this work. Then, the orbital propulsion system is positioned at one extremity of the longitudinal axis of the CubeSat and perfectly centered in the transverse ones. It is also perfectly aligned with the longitudinal axis. Consequently, the longitudinal shift in the COM position does not translate in a more disruptive torque. Also, we have assumed that inertia matrices were symmetrical. This is an important simplification because the initial COM shift which provides the inertia matrices is far from being symmetrical. As the time goes on, the decrease of the propellant should result in an asymmetric evolution of the inertia. Because such a modification would result in less optimal control laws, one can assume that our simplification led to conservative results. In terms of propellant, a larger increase should be expected. Indeed, the trajectory solver and propagator use a Keplerian model. Hence, when no orbital thrust is applied (i.e., when the RWs are being desaturated), no external force perturbs the trajectory. A more realistic propagator, including the Earth flatness, third bodies, Solar Radiation Pressure (SRP) or atmospheric drag, would alter the ΔV budget. However, such perturbations are not expected to be dominant.

There are several ways to mitigate the negative mutual impacts between the GNC and the ADCS at CubeSat scale. Although the philosophy behind this standard promotes fast and low cost developments, a careful integration and test campaign is vital when designing spacecrafts with orbital maneuvers. Setting the spacecraft spinning before orbital thrust is applied is also an efficient technique to lower the demand on attitude actuators. However, it was not sufficient in the case of the D-Sat mission [84]. Integrating a thrust vector control is often proposed to actively compensate inherent thruster disturbance torques [35, 73], but it is at the cost of simplicity and reliability. Finally, the concept of Unified Propulsion System (UPS), with several thrusters fed by the same propellant tank and providing multiple thrust vectors, is promising (see section VI).

V.2 - Implications for the Scientific Cases

Going back to the scientific applications motivating this work, several conclusions can be made. First of all, the interplanetary environment limits us in terms of available actuators. Only RWs, ACTs and solar actuators may be considered. Hence, two main scenarios must be assessed:

- a single-thruster propulsion system is dedicated to orbit control, similarly to the fictional study cases;
- a multi-thruster Unified Propulsion System (UPS) is in charge of providing both attitude and orbit control.

The large impact of having a single thruster to perform orbital maneuvers was extensively investigated in the previous section. In interplanetary missions, it will

slowly saturate the RWs, if any, or consume propellant from dedicated attitude control thrusters. In addition, the cost at system level of having two separate propulsion systems is too high. Solar actuators, such as solar sails or solar panels, are hard to operate and perform very slow maneuvers, likely to be incompatible with the required autonomy in both missions.

A multi-thruster system seems like the most promising solution. From the investigation of thruster concepts compatible with UPS (see section II.4.1), we can see that compatible thrusters are usually fed by gaseous or liquid propellant. As a matter of fact, among identified CubeSat propulsion systems, only CGTs, several mono-propellant systems and the L-µPPT already provide multiple thrust vectors. In the cruise context, where the CubeSat must correct its Hohmann transfer trajectory, the small ΔV budget ($\sim 10\,\mathrm{m\,s^{-1}}$) is compliant with what many CGTs can provide. In contrast, proximity operations, based on the proposed TCM loop (see section III.3.1), are more demanding. Therefore, the L-µPPT is the best solution, thanks to its high I_{sp} (1,000 s).

The attitude control required in both missions must also be considered in the propellant budget. The cruise context has very low requirements in terms of attitude control, and the UPS can easily be in charge of pointing maneuvers outside of orbital maneuver windows. Once again, the proximity operation case is proving to be more challenging. As seen in section III.1, performing pointing with thrusters is prohibited because it may harm scientific measurements. Consequently, RWs will be in charge of attitude control, at least during scientific phases, and the liquid PPT will off-load the RWs probably during TCMs.

In both cases (cruise and proximity operations), the amount of propellant consumed for attitude control, whether it is to point the spacecraft or to desaturate RWs, must be assessed. In this regard, the simulation environment developed in section IV will be used. The major modification concerns the trajectory solver, currently optimized for Earth-orbiting spacecrafts. Unfortunately, the realistic simulation of trajectory maneuvers in the two scientific cases could not be covered in the frame of my thesis. Such simulations are identified as the main next step regarding the design of the AOCS for BIRDY-T.

CHAPTER VI

New System Performance Index for Thrusters

The need of relying on mission-relevant performance indexes when designing CubeSats with low-thrust propulsion is present all along this work. The limits of the current approach to CubeSats with propulsion design were investigated in section II.4, while the functional requirements of an Attitude & Orbit Control System (AOCS) for interplanetary CubeSats, in the frame of the BIRDY-T project, were listed in section III.4. Yet, such performance indexes are not easily accessible from Commercial Off-The-Shelf (COTS) designers who mainly rely on low-level indexes. This observation is especially true when dealing with electric propulsion systems for CubeSats. To overcome this difficulty, C. Koppel and I have proposed a selection criterion [163], which is the topic of this section.

For clarity, we recall here that three main performance indicators are currently provided by thruster designers:

- the thrust F,
- the specific impulse I_{sp},
- the power consumption.

Depending on the data sheets, the dry mass of the system m_{dry} (mass of the system with empty tanks), the propellant mass m_p, or the system wet mass $m_{wet} = m_{dry} + m_p$ may also be provided.

VI.1 - Power Impact for Electric Propulsion

The specific impulse (I_{sp}), is widely used to compare thrusters' performance. Based on this index, electric propulsion systems are by far superior to chemical systems. Yet, when using the specific impulse for electric propulsion, its dependency on the electric power must be taken into account. As a matter of fact, I_{sp} can be seen as an indicator of the power P_{el} needed by the thruster

$$\frac{P_{el}}{F} = \frac{I_{sp} g_0}{2\eta} \; [\mathrm{W\,N^{-1}}], \tag{VI.1}$$

where η is the efficiency of the thruster (efficiency of the process of conversion from electrical power to mechanical power). From this expression, one can see that the high specific impulses permitted by electric thrusters come at the cost of more power demand for the same thrust. This increase in power demand does not appear explicitly in the current I_{sp} expression which is hence misleading.

VI.1.1 - Example of an Electric Thruster Concept

In order to illustrate the need for a strong power supply, we now focus on a specific example of electric thruster: the IFM Nano Thruster from Enpulsion [112, 111]. At one point of operation, the thruster is said to consume 40 W and deliver 3,770 s of I_{sp}. For a 3 kg CubeSat at Beginning Of Life (BOL) (mass proposed in the data sheet), the manufacturer translates this I_{sp} into 2,204 $\mathrm{m\,s^{-1}}$ of ΔV. Disregarding every other consideration, one could imagine that this amount of ΔV may be sufficient for a CubeSat released in Geostationary Transfer Orbit (GTO) to escape the attraction of the Earth and perform an interplanetary mission. The purpose of the following study is to assess the relevance of this question for such small CubeSats.

The propulsion system dry mass and the propellant mass at BOL are said to be $m_{dry} = 0.75$ kg and $m_{prop} = 0.25$ kg, which results in a wet mass $m_{wet} = 1$ kg. As a consequence, only 2 kg are left to use for the CubeSat. Operating this thruster for orbital maneuvers requires long continuous thrusting. Indeed, the propulsion system delivers a nominal thrust of 350 µN, incompatible with impulsive maneuvers even with CubeSats. Except during eclipses, where the power must come from on-board batteries, the electrical power is delivered by solar panels. From section III.2.1.3, we know that, at BOL, a 3U CubeSat covered with solar arrays produces 4.1 W of Orbit Average Power (OAP). Such power is incompatible with the 40 W required by the thruster. Hence, deployable solar panels must be added, which will come with an added mass.

Here, we propose to estimate the mass impact of additional solar panels introducing the mass-to-power ratio α_{pow}. Investigating available solar panels for CubeSats, and the solution proposed by ISIS in particular [135], we find $\alpha_{pow} = 22$ kg/kW. In Koppel and Quinsac [163], the OAP at midlife is calculated for a spacecraft able to rotate around its thrust axis (to maximize the area of solar panels on the sunlit side), with the Sun line-of-sight in the orbital plane. It results that the OAP is 34 % of the peak power at BOL. Taking this value into account, the mass-to-power ratio of solar panels increases to $\alpha_{pow} = 64$ kg/kW.

One can now easily measure the mass of solar panels required to continuously power the electric thruster: $m_{sol.pan.} = 2.56$ kg. One notices that the required mass for the thruster to operate is 3.56 kg ($m_{wet} + m_{sol.pan.}$), which is already higher than the proposed satellite mass at BOL. As a result, interpreting I_{sp} as a ΔV of 2,204 $\mathrm{m\,s^{-1}}$ for a 3 kg CubeSat is misleading, and a bigger platform is required to profit from the high level of performance enabled by this propulsion solution.

Yet, it must be mentioned that the added mass that we have just computed is underestimated. Indeed, the mass of the batteries is not considered, and neither is the impact of such high power on the Power Management And Distribution (PMAD) system. The required mass to handle increased thermal loss and provide the required attitude control are also neglected.

VI.1.2 - System Specific Impulse

In 1997, Erichsen [2] proposed a new index called the system-specific impulse (I_{ssp}) to improve the deficient specific impulse, which is essential as proven in the previous section. By noting that I_{sp} only considers the mass of propellant, the system-specific impulse is defined[1] as a function of the total mass of the thruster m_{PS}, as

$$I_{ssp} = \frac{I_{tot}}{m_{PS} g_0} \text{ [s]}. \tag{VI.2}$$

Thus defined, I_{ssp} necessitates introducing the thruster mass for chemical and electric thrusters. In the case of chemical thrusters, this mass is

$$m_{PS} = m_{H/W} + m_{PSS} \text{ [kg]}, \tag{VI.3}$$

where $m_{H/W}$ is the mass of the propulsion system's hardware (including the thruster, valves and piping), and m_{PSS} is the mass of propellant with its corresponding tankage.

For electric propulsion, the mass of the propulsion device is adapted to take the mass of the power supply and electric control system m_{El} into account

$$m_{PS} = m_{H/W} + m_{PSS} + m_{El} \text{ [kg]}. \tag{VI.4}$$

If applied to the example from the prior section, the system-specific impulse from Erichsen is $I_{ssp} = 238\,\text{s}$. This value is only 6 % of the previous I_{sp}, which translates in less than $200\,\text{m}\,\text{s}^{-1}$ of ΔV.

VI.2 - Proposition for an Improved System Specific Impulse

VI.2.1 - Identified Criteria

The limits of the specific impulse, mentioned on several occasions all along this work, has been demonstrated for an electric propulsion system. Then, the system-specific impulse, as proposed by Erichsen [2], was introduced. Despite the promising handling of the power supply, the above form of I_{ssp} does not cover all the aspects

[1] Similarly to I_{sp}, I_{ssp} can be expressed without the standard acceleration.

that we consider essential when it comes to characterizing propulsion systems. Below, we list thruster criteria that are of importance:

- Thrust system mass,
- Power needs,
- Management of simultaneous or sequential use of thrusters,
- Thermal discharges and ElectroMagnetic Compatibility (EMC), defined hereafter,
- System redundancy philosophy,
- Number of thrusters,
- Unified Propulsion System (UPS) compatibility (see section II.4.1),
- Continuous or intermittent use of propulsion,
- Thruster uptime, which transcribes the delay before the propulsion device can be fully operated,
- Standby power,
- Operational total impulse (qualified lifetime),
- System worst case total impulse, related to end-of-life of one thruster before the others, as detailed below,
- Attitude control capability and consistency with inherent disturbance torque,
- Thruster Technology Readiness Level (TRL).

This list is not exhaustive. Unfortunately, not all the above criteria could be included in our concept of improved system-specific impulse (for example, thruster uptime and TRL). Before expressing the new index, we develop some of these criteria, either because they are relatively new or because they come with hidden interconnections.

Many electric thrusters require important amounts of energy to operate. Among other negative consequences, the increased power demand comes at the cost of increased thermal discharges, which can be seen as heat loads that must be dissipated by the thermal management system. Similarly, high levels of electromagnetic energy associated with some thruster concepts can harm surrounding equipment and yield therefore EMC concerns. Solutions, such as shielding, result in more mass.

If one wants a spacecraft with redundant thrusters, the cost will be entirely different depending on the compatibility of the with the UPS concept. For incompatible systems, the cost of redundancy may be to double every component required for the thruster to operate, hence dividing I_{ssp} by a factor of two.

In section V.1, we have seen that the mutual impacts of attitude and orbit control may be reduced if the same thrusters can provide both attitude and orbit control. A UPS is perfectly suited to this need. Incompatible systems, however, suffer from a great penalty related to the worst case total impulse design. Indeed, the offset between the Center Of Mass (COM) and the Center Of Geometry (COG) results

in a more important usage of one thruster at the expanse of the others. Because each thruster has its own propellant, hence its own thruster total impulse, the end-of-life is then defined by the first thruster running out of propellant. In Koppel and Quinsac [163], a worst-case design based on the CubeSat Design Specification (CDS) is proposed, leading to a total impulse reduced to about 50 %. Obviously, in case there is no geometrical offset, the total impulse of the system is the sum of the total impulse of each thruster.

Another aspect of the attitude control during Trajectory Correction Maneuvers (TCMs) is the minimum number of actuators. In order to perform three-axis attitude control in addition to the orbital control, a minimum of four actuators is required. This means that, if only thrusters are considered, there should be at least four of them on-board the CubeSat. In case those thrusters are meant to provide attitude control outside of TCMs, they should be quickly available, and not have to wait a long warm-up phase as it is the case with some thruster concepts. This is what we mean by thruster uptime.

VI.2.2 - Definition of the New System-Specific Impulse

Here is the proposed definition for a new system-specific impulse:

$$I_{ssp} = \frac{I_{tot} k_2}{g_0 \left(m_p + m_{tank}\right) k_1 + m_{thruster} k_3 + \left(m_{El} + m_{The}\right) k_4 + m_{ACS} k_5} [\text{s}], \quad \text{(VI.5)}$$

where:

- I_{tot} is the total impulse capability per thruster;
- m_p is the propellant mass per thruster;
- m_{tank} is the mass of the tank. For non-exotic and large systems, $k = m_{tank}/m_p$ is almost constant;
- $m_{thruster}$ is the dry mass of one thruster;
- m_{El} is the mass of the electric system dedicated to one thruster, including the thruster power supply, as well as the dedicated mass of solar arrays and batteries if any;
- m_{The} is the mass of the thermal system dedicated to managing the thermal discharges of one thruster (which includes its power system);
- m_{ACS} is the mass of the attitude control system dedicated to orbital maneuvers if any.

Inserting equation II.7 in equation VI.5 allows us to rewrite the newly defined system-specific impulse as

$$I_{ssp} = \frac{I_{sp} k_2}{(1+k) k_1 + \frac{1}{m_p} \left(m_{thruster} k_3 + \left(m_{El} + m_{The}\right) k_4 + m_{ACS} k_5\right)} [\text{s}], \quad \text{(VI.6)}$$

where k is the structural index defined as m_{tank}/m_p. The coefficients in both equations VI.5 and VI.6 are explained in table VI.1.

Table VI.1: Coefficients for the proposed system-specific impulse (I_{ssp}) in equation VI.5.

Coefficient	Nominal value	Comments
k_1	1	Set to 2 for a mission requiring redundancy but using a thruster concept incompatible with the UPS.
k_2	1	May be set to 0.5 in a mission worst case, when several thrusters incompatible with the UPS are firing in about the same direction (see section VI.2.1).
k_3	1	Set to 2 if the mission requires redundancy.
k_4	$1/N$	Set to 1 if the thrusters are all used simultaneously.
k_5	0	Set to 1 if the thrusters cannot provide the required attitude control during orbital maneuvers.

VI.2.3 - Application

A first application of the above new index is now carried on. Because an exhaustive study of the thrusters reviewed in section II.3 including the possible configurations and operation logic is unfeasible, the approach is simplified, considering two following configurations of propulsion systems:

1. One single thruster system with short pulses. This case relates to the case studies investigated in section III.5 where we have demonstrated how important the impact of a continuous orbit control thruster is on the attitude control system. Therefore, only short pulses, with respect to the orbital period, are dealt with here. The case of a dedicated attitude control system ($k_5 = 1$ in equations VI.5 and VI.6) is not explored.

2. A propulsion system made of four thrusters with a thrust approximately parallel with the main axis. Thrusters are operated sequentially, hence reducing the mass and complexity of the power subsystem. Such a configuration allows thrust orientation without the need for other actuators. For this case, propulsion systems requiring a hot standby power must be treated carefully. Although we have defined m_{El} and m_{The} as the mass of the electric and thermal systems dedicated to one thruster (the multiplicity being taken care of by the coefficient k_4), the hot standby power concerns all thrusters at once.

We have considered that any system requiring more than 5 W needs a dedicated power subsystem whose mass is computed with $\alpha_{pow} = 64\,\mathrm{kg\,kW^{-1}}$. The results are gathered in table VI.2.

Table VI.2: System-specific impulses of identified propulsion systems. When computed for four thrusters, it is assumed that they are aligned with the main axis of the CubeSat, and that they are operated sequentially.

Type	Model	I_{sp} [s]	I_{ssp} single thrust. [s]	I_{ssp} 4 thrust. [s]
Cold gas	MEMS	68	15	15
	NanoProp 3U	60	12	12
	NanoProp 6U	60	9	9
	JPL MarCO MPS	40	11	18
	NEA Scout MiPS	40	8	15
	CuSP	40	5	8
	ACS	65	5	8
	CNAPS	45	6	6
	MEPSI MiPS	44	2	2
	MiPS Standard	40	4	6
	MiPS End-mounted	40	7	11
	C-POD	40	15	15
	Palomar	50	8	8
Mono- & bi-propellant	MPS-120	210	37	48
	BGT-X5	220	21	32
	ADN MiPS	200	38	52
	ArgoMoon PS	190	24	33
	Lunar Flashlight PS	169	47	61
	EPSS	200	39	50
	MPS-130	244	38	59
	PM400	285	74	84
	PM200	285	48	58
	HYDROS-C	310	54	76
Resistojets	XR-50-050	49	3	10
	VHTR	100	4	12
	MRT	150	19	28
	PUC 0.25U	70	11	20
	PUC 0.5U	70	17	27
	PUC 1U	70	25	35
	MVP	83	16	16

Continued on next page

Table VI.2: Continued from previous page

Type	Model	I_{sp} [s]	I_{ssp} single thrust. [s]	I_{ssp} 4 thrust. [s]
Electroth. RF	RFT	120	13	26
PPT & VAT	PPTCUP	670	14	7
	NanoPPT	640	55	28
	BmP-220	536	23	18
	L-µPPT	1,000	308	308
	µCAT	3,000	501	251
	Plasma Jet Pack	5,000	150	159
Ion	RIT-µX	2,000	54	149
	BIT-3	2,300	456	425
HET	HT-100	1,000	30	96
	BHT-200	1,375	24	74
	ExoMG-nano	1,200	90	179
Electrospray	IFM Nano	3,770	223	212
	S-iEPS	1,160	264	132
	TILE-50	1,250	111	56
	TILE-500	1,250	226	157
	TILE-5000	1,500	146	128
	BET-100	2,104	20	24
	BET-1mN	800	29	22

A comparison between thrusters' I_{sp} and I_{ssp} from the second case (four thrusters operated sequentially) is displayed in figure VI.1, while figure VI.2 shows the power as the function of I_{ssp} (to be compared with figure II.11). One can see that I_{ssp} is often ten times smaller than I_{sp}, highlighting the poor system performance of many thrusters. On the contrary, some thrusters concept that may not be ideal when looking only at I_{sp} proves to provide excellent performance at the system level. This is especially important for CubeSats, when the mass and power available are so constrained. As a matter of fact, the discrepancies between I_{sp} and I_{ssp} shown by this study tend to reduce for larger platforms. This has to do with the high structural index of CubeSats (m_{tank}/m_p).

In this application of the novel system-specific impulse, it is important to note that we have been limited in several manners:

- The estimate of the mass required to handle thermal rejections m_{The} could not be assessed.

- The fragmented information provided by designers' data sheets sometimes prevent us from computing accurately the proposed I_{ssp}.

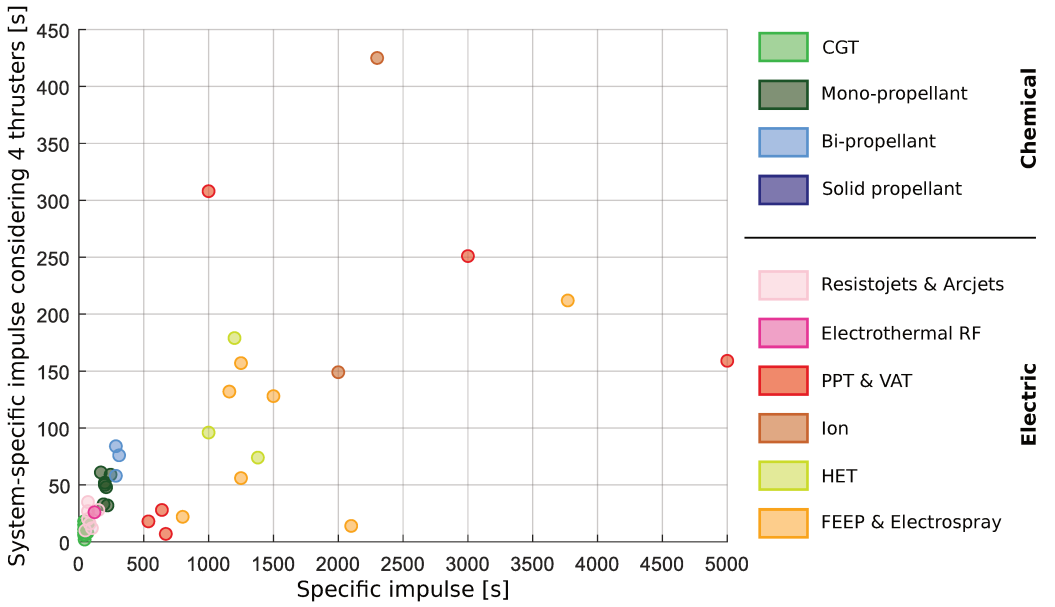

Figure VI.1: System specific impulse (I_{ssp}) versus specific impulse (I_{sp}). The system specific impulse is computed considering four thrusters used sequentially.

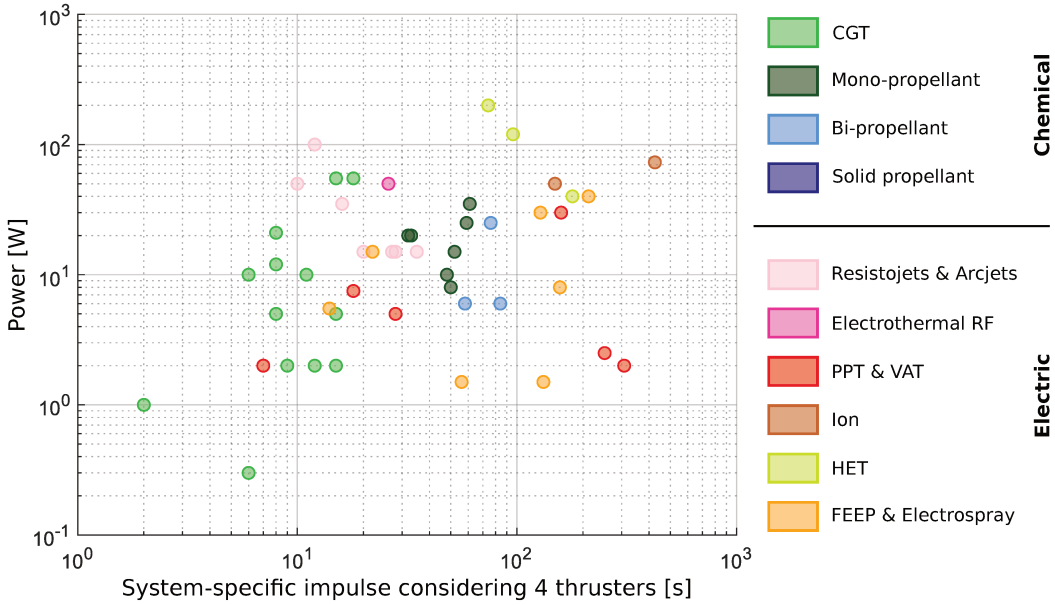

Figure VI.2: Power versus system specific impulse (I_{ssp}). The system specific impulse is computed considering four thrusters used sequentially.

- The multiplicity of possible configurations forced us to propose two specific configurations for this work. Now that the foundation of this index has been laid, other configurations may be investigated by each CubeSat designers, so as to select the system that suits his needs best.

Thus defined, the system-specific impulse can be used inside the well-known Tsiolkovski equation (see equations II.5 and II.8). Yet, it must be mentioned that the I_{ssp} is a function of the total impulse considered. Hence, if smaller total impulses are required, the corresponding I_{ssp} is roughly proportional (as long as $m_p \ll m_{PS}$). It follows that a value in the range $]0, I_{ssp,max}]$ must be applied into the Tsiolkovski equation.

Conclusion

The first motivation of this work comes from the BIRDY-T (BIRDY Technology) project. This project was born out of the necessity of providing an interplanetary CubeSat with sufficient autonomy, notably in terms of Attitude & Orbit Control System (AOCS). The key points of this technological development are the In-Flight Orbit Determination (IFOD), covered by the thesis of Segret [9], and the orbit control. BIRDY-T became a reality when two scientific mission concepts, based on CubeSats, were proposed:

- to perform space weather measurements on an Earth-Mars-Earth trajectory (cruise context),
- to investigate the gravity field of a system of asteroids (proximity operations context).

These two missions are still at the heart of the project.

From the identification of the need for orbital maneuvers in the two mission concepts, we started investigating current and under development propulsion systems. Soon, the comparison made possible by common performance indexes proved to be flawed. Then, we chose to change the initial low-level approach and perform a functional analysis of the AOCS. Several key points were identified, the main ones being the coupling between Attitude Determination & Control System (ADCS) and Guidance Navigation & Control (GNC), and the need to establish a system-level index for propulsion systems. Through the simulation of hypothetical, yet representative, orbital maneuvers in Earth orbit, with the inclusion of active attitude control, we showed how overly optimistic the literature can be. Finally, we proposed a new performance index for systems, which proved to be very enlightening, especially at CubeSat scale.

Results

A State of the Art of Propulsion Systems

The state of the art of propulsion systems that I conducted since the beginning of my thesis leads to the same conclusions as recent studies, such as Tummala and Dutta [31] (2017), Krejci and Lozano [24] (2018), or Silva et al. [165] (2018). The

result is an extensive database of small propulsion devices, which can easily be used to compare thrusters performance and characteristics.

More often than not, the comparison of reaction jets is commonly based on three main performance indexes: the level of thrust, the specific impulse (I_{sp}) and the power consumption. As a matter of fact, those performance indexes, or ways to compute them, are present in most thrusters data sheets, whatever the source of energy. Mission designers rely on them to select a system and its point of operation (set of thrust, I_{sp} and power). For a mission requiring fast maneuvers, chemical propulsion systems are favored, while large orbital maneuvers tend to be accomplished with electric thrusters. But what is mainly left out is the inclusion of the propulsion inside the wider Attitude & Orbit Control System (AOCS). Studies proposing a more high-level approach rarely investigate both the necessity of attitude control during propulsive maneuvers and the inherent disturbances caused by the thruster [30, 128, 27].

Need for a High-Level Approach

For all these reasons, I derive the requirements of an AOCS for two interplanetary CubeSat missions which motivated this thesis, through a functional analysis. Ensuring that nearby surfaces are not contaminated by thrusters' plume or that ElectroMagnetic Compatibility (EMC) is respected are some shared requirements that one may retrieve on most spacecrafts with propulsion, although they are rarely taken into account in the early stages of the mission design. The more conventional compliance with the external environment requires the assessment of external perturbations, such as disruptive torques. Both our missions will be exposed to external torques of the order of $1 \times 10^{-8}\,\mathrm{N\,m}$, which is well within the capabilities of CubeSat actuators. Actually, the disruptive torque produced by the on-board propulsion is the major factor. It is shown that, considering the specifications imposed to 3U CubeSats by the CubeSat Design Specification (CDS) [6], currently available reaction wheels (RWs) cannot provide attitude control for every chemical thrusters, with the exception of some Cold Gas Thrusters (CGTs). The situation is even worse with magnetorquers (MTQs), whose maximum torque is incompatible with any of the identified propulsion systems.

The ΔV budget in the proximity operations context depends on the identification of trajectory correction maneuvers (TCMs) required by the CubeSat, while being compliant with the autonomy concern. A so-called TCM loop is proposed, taking profit of a useful mathematical property. I derive the control law behind the TCM loop and assess the associated $\Delta V \simeq 140\,\mathrm{m\,s^{-1}}$ for a three-month mission. Although this budget allows me to constrain the selection of a propulsion system, the resulting attitude control budget is still to be estimated. This estimation will, among other things, necessitate a modification of the attitude and orbit control simulation from this work, as explained hereafter.

In order to assess the mutual impacts between ADCS and propulsion, or with GNC in general, I come up with hypothetical study cases in Earth orbit. The first one is a CubeSat performing a deorbiting maneuver from a 780 km-altitude Sun Synchronous Orbit (SSO). In the second one, a CubeSat deployed in Geostationary

Transfer Orbit (GTO) must escape the Earth attraction on its own. The choice of Earth orbits stems from two aspects: the willingness to suggest case studies representative of the needs for propulsion on-board CubeSats, and the significant amount of literature on the topic of trajectory solvers for Earth-orbiting spacecrafts [156, 157, 158, 159].

Investigating Mutual Impacts Between Attitude & Orbit Control

Then, I design a simulation environment to be used, ultimately, not only in the Earth environment. The simulation of spacecraft attitude takes into account the four external perturbations and simulates main CubeSat actuators, namely RWs, MTQs and Attitude Control Thrusters (ACTs). The principal control strategy, based on the quaternion error, is adapted from Sidi [151]. Other control laws are also implemented, which allow simulating operational modes such as RW desaturation or satellite detumbling. Although the whole control part is simulated, the attitude determination aspect is omitted in this work. Regarding the spacecraft trajectory, it is simulated using a propagator from the literature. More specifically, TCMs are computed and propagated thanks to the Lagrange Planetary Equations, which means that only the attraction of the Earth and the disruptive force represented by the thrust are considered. Effects such as the Earth flatness (J2), atmospheric drag or third bodies are neglected. One can assume that results obtained without those effects are conservative. As a result of my PhD, the entire attitude and orbit control simulation that I designed using Matlab is available for further studies at the Paris Observatory. As a matter of fact, its adaptation to the Python language started few months ago with an internship under my supervision, in order for the simulation to be integrated into a wider simulation tool called DOCKS, and currently developed at C^{2}ERES.

The fictional cases proposed are simulated using my attitude and orbit control simulation. I compare several realistic cases with their references that do not consider attitude control. In a case of deorbiting, I find that a realistic scenario yields +50 % increase in maneuver duration. While matching the CDS requirements strictly, the duration is at least +225 % longer than expected, meaning that the CubeSat is lost. In an Earth escape case, I show that the mass of propellant is +100 %, although the configuration is still optimistic. The propellant mass is even increased by more than 200 % in our pessimistic scenario. A final result is the dominant impact of inherent thruster disturbance torque over the efficiency thrusting locations.

Escaping the Earth orbit to reach interplanetary trajectories is an even more challenging case. From GTO, an efficient and powerful orbital propulsion is necessary. In order to keep the mission feasible in terms of mass assigned to the propellant, very strong requirements must be imposed to orbital propulsion integration and ADCS design. Indeed, the fuel mass is already doubled when the Center Of Mass (COM) is located on a sphere of 5 mm around the Center Of Geometry (COG), reaching 2.5 kg for an 8 kg CubeSat. Adding the dry mass of both the propulsion devices, the RWs, the dedicated solar panels and all the other vital subsystems, such a mission might already be unfeasible. Finally, the fuel that can be saved by adjusting the

moments on the orbit when the maneuver is performed is several times lower than the mass lost to counteract undesired mutual impacts between GNC and ADCS.

When it comes to the two scientific missions inspiring BIRDY-T, we recommend using a Unified Propulsion System (UPS). Because the proximity operation context is also quite demanding in terms of ΔV ($142\,\mathrm{m\,s^{-1}}$), few propulsion devices meet these requirements. At the moment, the system called L-µPPT is the most promising option, although it is only at Technology Readiness Level (TRL) 3.

Overcoming the Specific Impulse: the System Specific Impulse

Building on all the previous reflections about integrating a propulsion system onboard a CubeSat, it is clear that a new performance index is necessary to help mission planners select the thruster that will meet their requirements and constraints. By taking the example of an efficient thruster design, the demonstration is made that working only in terms of specific impulse omits considerations such as the increase in mass required to power an electric thruster, which may greatly mislead mission designers. A promising improvement to I_{sp} was proposed by Erichsen [2], in particular for including the impact of the power demand: the system-specific impulse (I_{ssp}).

From the original idea of Christophe Koppel, together we recommend exploiting further the concept of I_{ssp} by including every hidden impact coming with the integration of a propulsion system [163]. Out of these impacts, one can mention the number of thrusters, the UPS compatibility and the operational total impulse or the attitude control capability. Another interesting feature is the index dependency on the thruster configuration and concept of operation. The expression of this new performance index is recalled here:

$$I_{ssp} = \frac{I_{tot} k_2}{g_0 \left(m_p + m_{tank}\right) k_1 + m_{thruster} k_3 + \left(m_{El} + m_{The}\right) k_4 + m_{ACS} k_5} [\mathrm{s}].$$

This equation takes into account the masses of all the necessary components for the propulsion system to operate, together with ad hoc coefficients, as defined in section VI.2.2.

When applying this index to previously identified propulsion systems, it results that some thruster concepts, originally disregarded when only focusing on I_{sp}, are now more appealing. It is essential, especially when considering small platforms such as CubeSats, where any large demand - whether it is power, thermal dissipation, dedicated attitude control, etc. - immediately translates into additional mass. I_{ssp} should be thought as a more viable selection criterion than I_{sp}, the latter being more of an indication regarding the power need of electric thrusters.

It must be pointed out that the proposed application of I_{ssp} is not complete because the impact of thermal loads and electromagnetic interference were too difficult to assess at this stage. The lack of data from thruster designers is sometimes also an issue when trying to apply the proposed system-specific impulse.

Future Work

This thesis lays the groundwork of the design of low-thrust propulsion for CubeSats at the Paris Observatory - Paris Sciences & Lettres (PSL). The tools developed as well as the gained experience will benefit to both ongoing and future CubeSat missions supported by C^2ERES, the space pole of PSL.

Regarding BIRDY-T, a propulsion system, namely L-µPPT, was identified as a promising solution. However, its development is currently in standby at TRL $3-4$. Based on the approach proposed in this work, other systems may be selected, especially if the concept of UPS disseminates.

The attitude and orbit control simulation environment is, at the moment, limited to the Earth environment. The simulation of parasite torques is easily transposable to interplanetary missions, provided that the local environment is known (magnetic field, atmosphere, ejecta, distance to main bodies). Similarly, propagating interplanetary trajectories can be done using techniques based on the three-body problem, or more complex ones. The main difficulty lies in the computation of the orbital maneuver command, which makes the difference between a trajectory propagator and a trajectory solver. In the proximity operations context, because the control law is already known (TCM loop), all that is left to do is to implement the aforementioned propagator in the simulation environment. The task is more complex for the cruise context, because the TCM will depend on the shift with respect to the reference trajectory as well as when it is performed during the Hohmann transfer trajectory to Mars. This brings us to the next milestone of the BIRDY-T project: an end-to-end simulation of the autonomous AOCS including the IFOD developed by B. Segret. The purpose here is to simulate the interactions between the autonomous determination of the position and the rest of the AOCS, to assess further its feasibility in the proposed mission contexts. We estimate that another full-time year is necessary to link those two aspects of BIRDY-T.

The results of the hypothetical case studies (deorbiting from a 780 km altitude orbit and escaping Earth orbit) may serve the CubeSat community interested in gaining orbital autonomy in Earth orbit. Indeed, the proposed maneuvers and CubeSat configurations are typical of what can be seen in the literature. Now, however, the mutual impacts between ADCS and GNC have been assessed. Without any modification, other maneuvers/configurations can be investigated in the Earth environment. Among the possible improvements, the simulation of the attitude determination is not the most decisive one, contrary to what one might think. In fact, the time evolution of the spacecraft inertia matrix is probably the major impact currently left out, because it is expected to result in less optimal control. Here, I should recall that a non-negligible increase of the maneuver duration due to the in-advance computation of the orbital control law was observed. Further investigations of that matter should be considered.

Finally, the system-specific impulse proposed as new performance index has the potential to, if not replace the system impulse, at least be a more meaningful alternative for selecting propulsion systems for very small platforms. Many thruster designers, mainly focused on improving the specific impulse of their system, may hopefully start considering more aspects that are essential to mission designers (uni-

fied propulsion concept, worst-case design, interactions with the attitude control system, thermal system or power system, etc.). At least, this new index will benefit to mission designers to properly select a propulsion system. The proposed formulation may not be definitive, and some improvements may come from its application to a large number of systems. As a matter of fact, some aspects are still difficult to assess and to integrate in the equation, in particular the additional mass associated with thermal dissipation, EMC, or dedicated attitude control.

APPENDIX A

Fundamentals of Attitude Representation

The most fundamental way of describing the orientation of two frames relative to each other is to describe their basis vectors in the other frame. Let two reference frames $\mathcal{N}$ and $\mathcal{B}$ be defined in $\mathbb{R}^3$ with three orthonormal base vectors $\hat{\mathbf{n}}_{1,2,3}$ and $\hat{\mathbf{b}}_{1,2,3}$. We define the direction cosine α_{ij} as the angle between a particular base vector $\hat{\mathbf{b}}_i$ from $\mathcal{B}$ and the corresponding base vector from $\mathcal{N}$. Hence, we can express $\hat{\mathbf{b}}_i$ in terms of the base vectors $\hat{\mathbf{n}}_{1,2,3}$ as

$$\begin{aligned}\hat{\mathbf{b}}_i &= \left(\hat{\mathbf{b}}_i\hat{\mathbf{n}}_1\right)\hat{\mathbf{n}}_1 + \left(\hat{\mathbf{b}}_i\hat{\mathbf{n}}_2\right)\hat{\mathbf{n}}_2 + \left(\hat{\mathbf{b}}_i\hat{\mathbf{n}}_3\right)\hat{\mathbf{n}}_3 \\ &= \cos\alpha_{i1}\hat{\mathbf{n}}_1 + \cos\alpha_{i2}\hat{\mathbf{n}}_2 + \cos\alpha_{i3}\hat{\mathbf{n}}_3.\end{aligned} \tag{A.1}$$

The Direction Cosine Matrix (DCM), also called rotation matrix or attitude matrix, is the 3-by-3 matrix that transforms arbitrary vectors from one frame to another. The elements forming the DCM are the unsigned angles between one frame and the other. The transformation from a vector $\mathbf{v}_n$ in $\mathcal{N}$ frame to a vector $\mathbf{v}_b$ in $\mathcal{B}$ frame is expressed using the DCM, such as

$$\mathbf{v}_b = \begin{pmatrix}\cos\alpha_{11} & \cos\alpha_{12} & \cos\alpha_{13} \\ \cos\alpha_{21} & \cos\alpha_{22} & \cos\alpha_{23} \\ \cos\alpha_{31} & \cos\alpha_{32} & \cos\alpha_{33}\end{pmatrix}\mathbf{v}_n = \mathbf{C}_{bn}\mathbf{v}_n. \tag{A.2}$$

The DCM $\mathbf{C}_{bn}$ describes the orientation of $\mathcal{B}$ relative to $\mathcal{N}$ and it is also called the rotation matrix or coordinate transformation matrix to $\mathcal{B}$ from $\mathcal{N}$. The DCM being orthogonal, its inverse is its transpose so that $\mathbf{C}_{bn}^T = \mathbf{C}_{nb}$ describes the orientation of $\mathcal{N}$ relative to $\mathcal{B}$. Another interesting property is the composition, which means that successive rotations can be described as matrix multiplications of individual matrices. Despite these advantages, DCMs are not the most suited representation. Indeed, they use nine parameters to describe orientation, of which only three are independent.

Euler angles are a set of three successive rotations that describe the attitude of a reference frame $\mathcal{B}$ relative to a reference frame $\mathcal{N}$. The three successive rotations are about the sequentially displaced axes of $\mathcal{B}$. Each rotation must be about an axis that has not been used for the previous rotation. Therefore, 12 transformation

sets exist. However, aircraft and spacecraft orientations are commonly described using the Euler angles yaw, pitch and roll (ψ, θ and ϕ). This specific set of Euler angles is usually referred to as the (3-2-1) set. Euler angles determine a unique orientation, which is generally an advantage over the rotation matrix. However, a given orientation can be described by several sets of Euler angles.

APPENDIX B

Models for Attitude Control Simulation

The Attitude Determination & Control System (ADCS) simulation that was presented in this thesis is based on several models, introduced in this appendix.

B.1 - Earth Magnetic Field Model

Although the Earth's magnetic field is complex, it can be modeled as a dipole (30 % errors are usually considered). In this simulation, we use data from the 12$^{\text{th}}$ generation of the International Geomagnetic Reference Field (IGRF) [166]. This model provides a field model up to 2015 and a linear annual predictive variation model for 2015-2020. Therefore, using the simulator at times after 2020 is not recommended because it would require to extrapolate available data. The magnetic field on and above the Earth's surface is defined in terms of a magnetic scalar potential V

$$\mathbf{B} = -\nabla V, \tag{B.1}$$

where the scalar potential is approximated in spherical polar coordinates at a specific time t by a finite series expansion

$$V(r,\theta,\phi,t) = a\sum_{n=1}^{N}\sum_{m=0}^{M}\left(\frac{a}{r}\right)^{n+1}\Big(g_n^m(t)\cos m\phi + h_n^m(t)\sin m\phi\Big)P_n^m(\cos\theta), \tag{B.2}$$

where $\mathbf{r}$ is the radial distance from the center of the Earth, $a = 6371.2$ km is the geomagnetic conventional Earth's mean reference spherical radius, θ is the geocentric co-latitude and ϕ the east longitude. The model provides the $g_n^m(t)$ and $h_n^m(t)$ to compute the magnetic scalar potential.

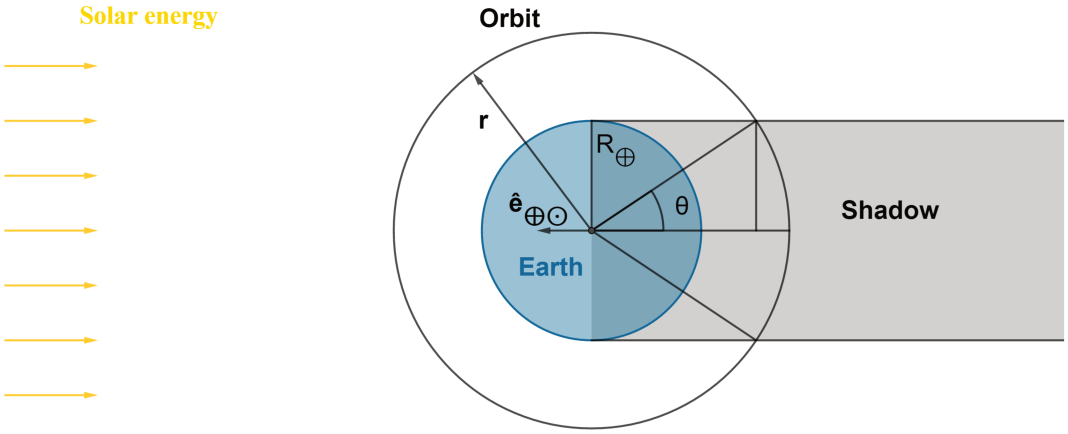

Figure B.1: Geometry of the cylindrical Earth shadowing.

B.2 - Earth Shadowing Model

Shadowing plays an essential part in space missions, especially for spacecrafts orbiting a body. They affect the electric power management by preventing the solar panels from collecting the Sun power, and also impact the spacecraft's attitude and orbit. A very simplistic model for determining whether the spacecraft is in the Earth shadow or not is presented here [167].

We consider that the shadow of the Earth is a cylindrical projection of the Earth's diameter along the direction of the Sun to the Earth as seen in figure B.1. Given the position $\mathbf{r}$ of the spacecraft and the unit vector from the Earth to the Sun $\hat{\mathbf{e}}_{\oplus\odot}$, it is possible to set a shadowing condition on the scalar product of those two vectors

$$\mathbf{r} \cdot \hat{\mathbf{e}}_{\oplus\odot} < -\sqrt{r^2 - R_\oplus^2}, \tag{B.3}$$

where $R_\oplus$ is the Earth equatorial radius, approximated as a sphere.

For satellites in higher orbits one should use a canonical approach that takes into account the finite size of both the Sun and the Earth. Umbra and penumbra areas can be calculated through geometric methods [154, 168]. When the satellite travels in the penumbra, the intensity of the illumination is proportional to the area of the solar disk illuminating the spacecraft. Slightly more complex geometric considerations were proposed to evaluate this illumination [168]. The impact of the planetary atmosphere on the light coming from the Sun, such as light absorption and scattering, is another factor that should be considered for precise simulations.

B.3 - Earth Atmospheric Density Model

Modeling the local atmospheric density is essential for the computation of its effects on the spacecraft's attitude and orbit. [143] provides a description of existing models with their assumptions in order to help the reader select the model that suits his mission the best. Our simulation is based on the empirical density model called NRLMISE-00 [169] because it is said to be more accurate for altitudes above 500 km, which corresponds to our domain of interest.

APPENDIX C

Modeling and Designing Attitude Control with Quaternions

This appendix introduces the mathematical tools that have been used to design the attitude control, based on the book of Sidi [151] and the lecture note of Blanke and Larsen [170]. First of all, a brief presentation of control theory is made, including the importance of Linear Time-Invariant (LTI) systems and some insights into the controller design process and stability test. Then, a linearization technique is presented.

C.1 - Classical Control Theory

The purpose of control theory it to design controllers for continuous operating dynaicl systems. This discipline overlaps many other fields such as electronics and aerodynamics.

Control theory is used when someone wants to control the output $x(t)$ of a system receiving an input $u(t)$. The objective of the control system design is to optimally control the output, according to criteria like delay or overshoot. Two fundamental types of control logic can be made: the open-loop and closed-loop control. Open-loop control is the simplest one because the process output is not taken into account. It is the case of a dish washer where the control is simply a fixed duration of the washing cycle. If the duration did depend on the evolution of the cleanliness during the cycle, this would be a closed-loop control. Block diagrams of those two types of control are displayed in figure C.1.

A system analysis is performed to ensure that a system has the expected behavior. Indeed, it must be stable under expected conditions, prevent oscillations or have a good enough response time and steady-state error.

The most important characteristic of our system is probably its stability. A system is considered stable if the output remains finite for finite inputs. Practically, it means that the satellite remains under control. Stability analysis is usually performed through the transfer function representation where all the poles of the transfer function must have negative real parts.

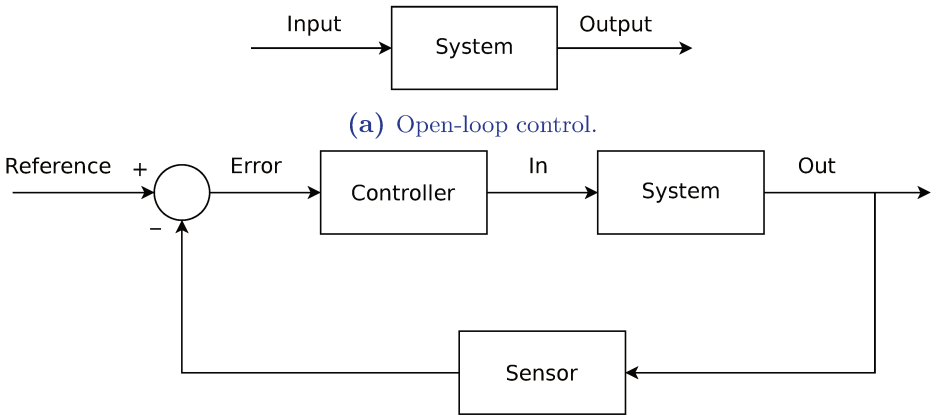

(a) Open-loop control.

(b) Closed-loop control.

Figure C.1: Block diagram of control loops.

The system time response represents the way the response of a dynamic system to an input evolves with time. It is made of the transient response and the steady state response. These are the responses right after the input signal application and a long time after, respectively. It may be of interest to study the frequency response of a system. Although LTI systems have the particularity of conserving the form and frequency of a sinusoidal input, the amplitude and the phase may be changed. Investigating these amplitude and phase differences as a function of the frequency concerns the frequency response of the system. Bode plots are probably the most common methods to display this frequency response.

C.1.1 - State-space Representation

Differential equations allow systems' description in continuous time domain. A state-space model represents a system by relating a set of input, output and state variables through differential equations. A classic representation of a linear system is

$$\begin{aligned} \dot{\mathbf{x}}(t) &= \mathbf{A}(t)\mathbf{x}(t) + \mathbf{B}(t)\mathbf{u}(t) \\ \mathbf{y}(t) &= \mathbf{C}(t)\mathbf{x}(t) + \mathbf{D}(t)\mathbf{u}(t), \end{aligned} \tag{C.1}$$

where $\mathbf{x}(t)$ is the state vector, $\mathbf{y}(t)$ is the output vector, $\mathbf{u}(t)$ is the input (or control) vector, $\mathbf{A}(t)$ is the state (or system) matrix, $\mathbf{B}(t)$ is the input matrix, $\mathbf{C}(t)$ is the output matrix and $\mathbf{D}(t)$ is the feedforward matrix. A block diagram of the linear system is available in figure C.2

Although the matrices can be time-dependent in the general case, we will make the assumption that they are not. Equation C.1 becomes a LTI system:

$$\begin{aligned} \dot{\mathbf{x}}(t) &= \mathbf{A}\mathbf{x}(t) + \mathbf{B}\mathbf{u}(t) \\ \mathbf{y}(t) &= \mathbf{C}\mathbf{x}(t) + \mathbf{D}\mathbf{u}(t), \end{aligned} \tag{C.2}$$

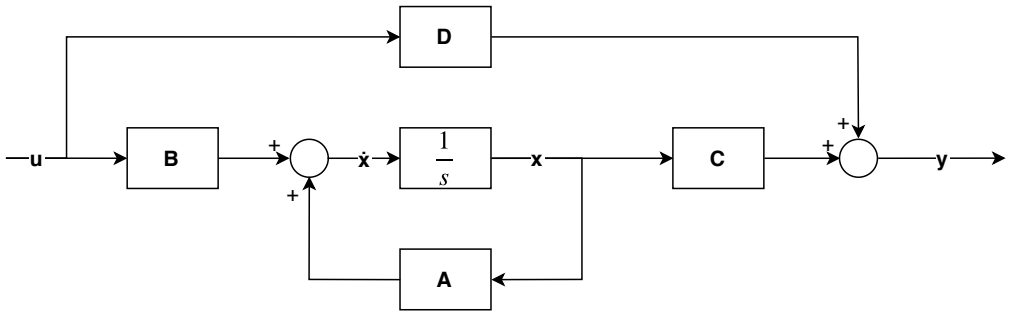

Figure C.2: Block diagram of the classic state-space representation.

Table C.1: Basic Laplace transforms.

$f(t)$	$F(s)$
$\delta(t)$	1
$x(t)$	$X(s)$
$x'(t)$	$sX(s) - X(0)$
$x''(t)$	$s^2X(s) - sX(s) - X'(0)$

LTI systems can be solved, making them fundamental in control theory. Their stability and natural response characteristics can be investigated by studying the eigenvalues of the matrix **A**. The objective is to simplify our system so as to make it linear and study its stability.

Impulse responses are of importance because the response of a system is obtained by summing the impulse responses. The summation in the time domain to get the output is called convolution and is expressed

$$(f * g)(t) = f(t) * h(t) = \int_{-\infty}^{+\infty} f(t-\tau)h(\tau)d\tau, \tag{C.3}$$

where $f(t)$ and $h(t)$ are two real or complex functions.

C.1.2 - Laplace Transform of a Linear Time Invariant System

Laplace transforms operate in the complex frequency $s = \sigma + i\omega$, with real numbers σ and ω. The Laplace transform $\mathcal{L}$ of a function $f(t)$, defined for $t \in \mathbb{R}+$ is the function $F(s)$

$$F(s) = \int_{0}^{+\infty} f(t)\exp(-st)dt. \tag{C.4}$$

Other useful transforms can be found in table C.1.

The complexity of equation C.3 is reduced using the Laplace transform $\mathcal{L}$ and introducing the transfer function. A transfer function $H(s)$ is the impulse response of a LTI system when all the initial conditions are set to zero. It transforms the

convolution in the time domain into a simple multiplication in the complex frequency domain:

$$H(s) = \frac{Y(s)}{X(s)} = \frac{\mathcal{L}(y(t))}{\mathcal{L}(x(t))}. \tag{C.5}$$

C.1.3 - Procedure for Stability Analysis and Design of Feedback Control Systems

The transfer function releases us from solving the complete differential equations. Because we are interested in the roots of the numerator and the denominator, it is more convenient to factor them into polynomials, respectively $N(s)$ and $D(s)$. Hence, the roots of $N(s)$ are the system zeros, whereas the roots of $D(s)$ are the system poles. Together with the gain K they fully characterize the differential equation and our system

$$H(s) = K\frac{N(s)}{D(s)}. \tag{C.6}$$

The stability of the linear system lies in its transfer function. The system is asymptotically stable if all its poles have negative real parts. Any unstable pole, that is to say with a positive real part, will cause the system response to increase without bound. The more negative the real part is, the quicker the response will decay.

The Laplace transform is now applied to the state-space model in equation C.2:

$$\begin{aligned} s\mathbf{x}(s) &= \mathbf{A}\mathbf{x}(s) + \mathbf{B}\mathbf{u}(s) + \mathbf{x}(t_0) \\ \mathbf{y}(s) &= \mathbf{C}\mathbf{x}(s) + \mathbf{D}\mathbf{u}(s). \end{aligned} \tag{C.7}$$

Introducing the identity matrix $\mathbf{I} \in \mathbb{R}^{n\times n}$, the transfer function of our system described in equation C.7 is

$$H(s) = \mathbf{C}(s\mathbf{I} - \mathbf{A})^{-1}\mathbf{B} + \mathbf{D}. \tag{C.8}$$

The stability of our system is investigated evaluating the poles of equation C.8. They are the roots of the denominator, i.e., the determinant of $s\mathbf{I} - \mathbf{A} = 0$ or the eigenvalues of $\mathbf{A}$. Control theory tells us that these poles must have a strictly negative real part for the system to be asymptotically stable.

C.2 - Jacobian Linearization of a Nonlinear Model

As mentioned in section C.1.1, LTI systems are very important in control theory because they can be solved. However, practically no real-world system meets the requirements of LTI systems, i.e., being linear and time-invariant. Therefore, the

objective is to simplify the systems as LTI systems and thereby use the classical control theory.

Here is some theory about the Jacobian linearization of a nonlinear system about an equilibrium point $(\overline{\mathbf{x}}, \overline{\mathbf{u}})$. Let a nonlinear differential equation be defined by:

$$\dot{\mathbf{x}}(t) = \mathbf{f}(\mathbf{x}(t), \mathbf{u}(t)), \tag{C.9}$$

where $\mathbf{x} \in \mathbb{R}^n$ is the state vector, $\mathbf{u} \in \mathbb{R}^m$ is the control input. We now define the deviation variables to measure a small deviation from a reference:

$$\begin{aligned} \delta\mathbf{x}(t) &= \mathbf{x}(t) - \overline{\mathbf{x}}(t) \\ \delta\mathbf{u}(t) &= \mathbf{u}(t) - \overline{\mathbf{u}}(t). \end{aligned} \tag{C.10}$$

Let's apply a Taylor expansion and truncate it after the 1$^{\text{st}}$ order:

$$\delta\dot{\mathbf{x}}(t) \approx \mathbf{f}(\overline{\mathbf{x}}, \overline{\mathbf{u}}) + \left.\frac{\partial \mathbf{f}}{\partial \mathbf{x}}\right|_{\substack{\mathbf{x}=\overline{\mathbf{x}} \\ \mathbf{u}=\overline{\mathbf{u}}}} \delta\mathbf{x}(t) + \left.\frac{\partial \mathbf{f}}{\partial \mathbf{u}}\right|_{\substack{\mathbf{x}=\overline{\mathbf{x}} \\ \mathbf{u}=\overline{\mathbf{u}}}} \delta\mathbf{u}(t). \tag{C.11}$$

Equation C.11 can be simplified using the definition of an equilibrium point, $\mathbf{f}(\overline{\mathbf{x}}, \overline{\mathbf{u}}) = 0_n$. The derivation of a vector with respect to a vector in equation C.11 is performed using the Jacobian

$$\frac{\partial \mathbf{f}}{\partial \mathbf{x}} = \frac{\partial f_i}{\partial x_j} = \begin{pmatrix} \frac{\partial f_1}{\partial x_1} & \cdots & \frac{\partial f_1}{\partial x_n} \\ \vdots & \ddots & \vdots \\ \frac{\partial f_n}{\partial x_1} & \cdots & \frac{\partial f_n}{\partial x_m} \end{pmatrix}. \tag{C.12}$$

For small deviations, the differential equation expressed in equation C.11 approximately governs the deviations' behavior. What is remarkable about this equation is that it is linear and time-invariant. Indeed, the derivatives of $\delta\mathbf{x}$ are linear combinations of the state vector deviation $\delta\mathbf{x}$ and the input deviation $\delta\mathbf{u}$. Moreover, the matrices

$$\mathbf{A} = \left.\frac{\partial \mathbf{f}}{\partial x}\right|_{\substack{\mathbf{x}=\overline{\mathbf{x}} \\ \mathbf{u}=\overline{\mathbf{u}}}} \in \mathbb{R}^{n\times n} \quad , \quad \mathbf{B} = \left.\frac{\partial \mathbf{f}}{\partial u}\right|_{\substack{\mathbf{x}=\overline{\mathbf{x}} \\ \mathbf{u}=\overline{\mathbf{u}}}} \in \mathbb{R}^{n\times m}, \tag{C.13}$$

are constant matrices. Finally, we write the linear system using the matrices $\mathbf{A}$ and $\mathbf{B}$ that we have just defined:

$$\dot{\delta\mathbf{x}}(t) = \mathbf{A}\delta\mathbf{x}(t) + \mathbf{B}\delta\mathbf{u}(t). \tag{C.14}$$

APPENDIX D

Mathematical Model of the TCM Loop

The Trajectory Correction Maneuver (TCM) loop proposed in section III.3.1, and displayed in figure D.1, is based on the parametric curve called rosette. In this appendix, we present its mathematical model.

Let M be a point on the curve, representing the position of an object. The curvilinear abscissa s is given by

$$ds^2 = \|d\mathbf{M}\| = dx^2 + dy^2. \tag{D.1}$$

Such a curve is parametrized by

$$\mathbf{OM} = r \sin k\theta \begin{pmatrix} \cos\theta \\ \sin\theta \end{pmatrix}. \tag{D.2}$$

The velocity of the object is derived from its position, leading to

$$\begin{aligned} \mathbf{v} &= \frac{d\mathbf{OM}}{d\theta} \\ &= rk\cos k\theta \begin{pmatrix} \cos\theta \\ \sin\theta \end{pmatrix} + r\sin k\theta \begin{pmatrix} -\sin\theta \\ \cos\theta \end{pmatrix}. \end{aligned} \tag{D.3}$$

Same goes for the acceleleration

$$\begin{aligned} \mathbf{a} &= \frac{d^2\mathbf{OM}}{d^2\theta} \\ &= 2rk\cos k\theta \begin{pmatrix} -\sin\theta \\ \cos\theta \end{pmatrix} - r\left(1+k^2\right)\sin k\theta \begin{pmatrix} \cos\theta \\ \sin\theta \end{pmatrix}. \end{aligned} \tag{D.4}$$

The length of a petal of the rosette Δs, which represents distance traveled during one full TCM described earlier, is obtained by

$$\Delta s = 2r \int_0^{\frac{\pi}{2}} \sqrt{1 - \left(1 - \frac{1}{k^2}\right)\sin^2(t)}\, dt. \tag{D.5}$$

To get a quatrefoil, we have to set $k = 2$, hence

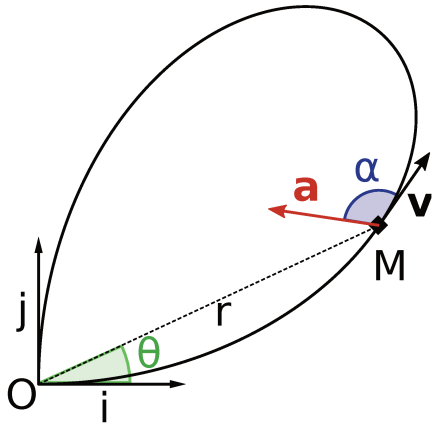

Figure D.1: Rosette parametric curve.

$$\Delta s = \frac{1}{2} r \int_0^{\frac{\pi}{2}} \sqrt{1 - \frac{3}{4}\sin^2(t)} dt \simeq 2.43r. \tag{D.6}$$

Bibliography

[1] A. Klesh, B. Clement, C. Colley, J. Essmiller, D. Forgette, J. Krajewski, A. Marinan, T. Martin-mur, J. Steinkraus, D. Sternberg, T. Werne, and B. Young, "MarCO : Early Operations of the First CubeSats to Mars," *32nd Annual AIAA/USU Conference on Small Satellites*, pp. 1–6, 2018.

[2] P. Erichsen, "Performance Evaluation of Spacecraft Propulsion Systems in Relation to Mission Impulse Requirements," in *Second European Spacecraft Propulsion Conference*. ESA SP-398. Paris, 1997.

[3] J. Janicik and J. Wolff, "CHIPSat spacecraft design: significant science on a low budget," in *UV/EUV and Visible Space Instrumentation for Astronomy II*, 2004.

[4] J. Puig-Suari, J. Schoos, C. Turner, T. Wagner, R. Connolly, and R. P. Block, "CubeSat developments at Cal Poly: the standard deployer and PolySat," B. J. Horais and R. J. Twiggs, Eds., vol. 4136, nov 2000, pp. 72–78. [Online]. Available: http://proceedings.spiedigitallibrary.org/proceeding.aspx?articleid=919754

[5] D. L. Oltrogge and K. Leveque, "An Evaluation of CubeSat Orbital Decay," *25th Annual AIAA/USU Conference on Small Satellites*, 2011.

[6] The CubeSat Program, "Cubesat design specification," Cal Poly SLO, Tech. Rep., 2009.

[7] SpaceWorks, "Nano/microsatellite Market Forecast, 9th Edition," SpaceWorks, Tech. Rep., 2019.

[8] NASA, "State of the Art of Small Spacecraft Technology," 2019. [Online]. Available: https://sst-soa.arc.nasa.gov/

[9] B. Segret, "Algorithme embarqué de navigation optique autonome pour nanosatellites interplanétaires," Ph.D. dissertation, Observatoire de Paris, PSL Université Paris, 2019.

[10] D. M. Hassler, C. Zeitlin, R. F. Wimmer-Schweingruber, S. Böttcher, C. Martin, J. Andrews, E. Böhm, D. E. Brinza, M. A. Bullock, S. Burmeister, B. Ehresmann, M. Epperly, D. Grinspoon, J. Köhler, O. Kortmann, K. Neal, J. Peterson, A. Posner, S. Rafkin, L. Seimetz, K. D. Smith, Y. Tyler, G. Weigle,

G. Reitz, and F. A. Cucinotta, "The Radiation Assessment Detector (RAD) investigation," *Space Science Reviews*, 2012.

[11] J. Vannitsen, F. Rizzitelli, K. Wang, B. Segret, J. C. Juang, and J. J. Miau, "A Satellite Data Analysis and CubeSat Instrument Simulator Tool for Simultaneous Multi-spacecraft Measurements of Solar Energetic Particles," *Journal of Astrophysics and Astronomy*, vol. 38, no. 4, pp. 1–10, 2017.

[12] A. Posner, D. Odstrčil, P. MacNeice, L. Rastaetter, C. Zeitlin, B. Heber, H. Elliott, R. A. Frahm, J. J. Hayes, T. T. Von Rosenvinge, E. R. Christian, J. P. Andrews, R. Beaujean, S. Böttcher, D. E. Brinza, M. A. Bullock, S. Burmeister, F. A. Cucinotta, B. Ehresmann, M. Epperly, D. Grinspoon, J. Guo, D. M. Hassler, M. H. Kim, J. Köhler, O. Kortmann, C. Martin Garcia, R. Müller-Mellin, K. Neal, S. C. Rafkin, G. Reitz, L. Seimetz, K. D. Smith, Y. Tyler, E. Weigle, and R. E. Wimmer-Schweingruber, "The Hohmann-Parker effect measured by the mars science laboratory on the transfer from Earth to Mars: Consequences and opportunities," *Planetary and Space Science*, vol. 89, pp. 127–139, 2013.

[13] D. A. Tito, G. Anderson, J. P. Carrico, J. Clark, B. Finger, G. A. Lantz, M. E. Loucks, T. Maccallum, J. Poynter, T. H. Squire, and S. P. Worden, "Feasibility analysis for a manned mars free-return mission in 2018," in *IEEE Aerospace Conference Proceedings*, 2013.

[14] J. Vannitsen, "Propagation of Solar Energetic Particles in interplanetary space by study of the particles spreading across the Interplanetary Magnetic Field," Ph.D. dissertation, NCKU, 2018.

[15] B. Segret, D. Hestroffer, G. Quinsac, M. Agnan, J. Vannitsen, and B. Mosser, "In-flight orbit determination for a deep space CubeSat," in *IEEE Aerospace Conference Proceedings*, vol. 2018-March, 2018.

[16] K. H. Glassmeier, H. Boehnhardt, D. Koschny, E. Kührt, and I. Richter, "The Rosetta mission: Flying towards the origin of the solar system," *Space Science Reviews*, 2007.

[17] J. Kawaguchi, A. Fujiwara, and T. Uesugi, "Hayabusa-Its technology and science accomplishment summary and Hayabusa-2," *Acta Astronautica*, vol. 62, no. 10-11, pp. 639–647, 2008.

[18] Y. Tsuda, M. Yoshikawa, M. Abe, H. Minamino, and S. Nakazawa, "System design of the hayabusa 2-asteroid sample return mission to 1999 JU3," *Acta Astronautica*, vol. 91, pp. 356–362, 2013. [Online]. Available: http://dx.doi.org/10.1016/j.actaastro.2013.06.028

[19] D. S. Lauretta, S. S. Balram-Knutson, E. Beshore, W. V. Boynton, C. Drouet d'Aubigny, D. N. DellaGiustina, H. L. Enos, D. R. Golish, C. W. Hergenrother, E. S. Howell, C. A. Bennett, E. T. Morton, M. C. Nolan, B. Rizk, H. L. Roper, A. E. Bartels, B. J. Bos, J. P. Dworkin, D. E. Highsmith, D. A. Lorenz, L. F. Lim, R. Mink, M. C. Moreau, J. A. Nuth, D. C. Reuter, A. A. Simon, E. B. Bierhaus, B. H. Bryan, R. Ballouz, O. S. Barnouin, R. P.

Binzel, W. F. Bottke, V. E. Hamilton, K. J. Walsh, S. R. Chesley, P. R. Christensen, B. E. Clark, H. C. Connolly, M. K. Crombie, M. G. Daly, J. P. Emery, T. J. McCoy, J. W. McMahon, D. J. Scheeres, S. Messenger, K. Nakamura-Messenger, K. Righter, and S. A. Sandford, "OSIRIS-REx: Sample Return from Asteroid (101955) Bennu," *Space Science Reviews*, vol. 212, no. 1-2, pp. 925–984, oct 2017.

[20] P. Michel, M. Kueppers, H. Sierks, I. Carnelli, A. F. Cheng, K. Mellab, M. Granvik, A. Kestilä, T. Kohout, K. Muinonen, A. Näsilä, A. Penttila, T. Tikka, P. Tortora, V. Ciarletti, A. Hérique, N. Murdoch, E. Asphaug, A. Rivkin, O. Barnouin, A. C. Bagatin, P. Pravec, D. C. Richardson, S. R. Schwartz, K. Tsiganis, S. Ulamec, and O. Karatekin, "European component of the AIDA mission to a binary asteroid: Characterization and interpretation of the impact of the DART mission," *Advances in Space Research*, 2018.

[21] M. Zannoni, G. Tommei, D. Modenini, P. Tortora, R. Mackenzie, M. Scoubeau, U. Herfort, and I. Carnelli, "Radio science investigations with the Asteroid impact mission," *Advances in Space Research*, 2018.

[22] P. Michel, A. Cheng, M. Küppers, P. Pravec, J. Blum, M. Delbo, S. Green, P. Rosenblatt, K. Tsiganis, J. Vincent, J. Biele, V. Ciarletti, A. Hérique, S. Ulamec, I. Carnelli, A. Galvez, L. Benner, S. Naidu, O. Barnouin, D. Richardson, A. Rivkin, P. Scheirich, N. Moskovitz, A. Thirouin, S. Schwartz, A. Campo Bagatin, and Y. Yu, "Science case for the Asteroid Impact Mission (AIM): A component of the Asteroid Impact & Deflection Assessment (AIDA) mission," *Advances in Space Research*, vol. 57, no. 12, pp. 2529–2547, jun 2016.

[23] F. Damme, H. Hussmann, E. Mai, J. Oberst, and K. Wickhusen, "Orbit Stability in the Binary Asteroid System Didymos - An Opportunity for Spacecraft Exploration," mar 2016.

[24] D. Krejci and P. Lozano, "Space Propulsion Technology for Small Spacecraft," *Proceedings of the IEEE*, vol. 106, no. 3, pp. 362–378, mar 2018. [Online]. Available: http://ieeexplore.ieee.org/document/8252908/

[25] M. Leomanni, A. Garulli, A. Giannitrapani, and F. Scortecci, "Propulsion options for very low Earth orbit microsatellites," *Acta Astronautica*, vol. 133, no. October, pp. 444–454, apr 2017.

[26] D. Guglielmo, S. Omar, R. Bevilacqua, L. Fineberg, J. Treptow, B. Poffenberger, and Y. Johnson, "Drag Deorbit Device: A New Standard Reentry Actuator for CubeSats," *Journal of Spacecraft and Rockets*, vol. 56, no. 1, pp. 129–145, jan 2019.

[27] E. Edlerman and I. Kronhaus, "Analysis of Electric Propulsion Capabilities in Establishment and Keeping of Formation Flying Nanosatellites," 2016.

[28] N. H. Roth, B. Risi, C. C. Grant, and R. E. Zee, "Flight Results from the CanX-4 and CanX-5 Formation Flying Mission," *29th Annual AIAA/USU Conference on Small Satellites*, 2015.

[29] T. Imken, J. Castillo-Rogez, Y. He, J. Baker, and A. Marinan, "CubeSat flight system development for enabling deep space science," in *2017 IEEE Aerospace Conference*. IEEE, mar 2017, pp. 1–14.

[30] S. Tardivel, A. T. Klesh, and S. Campagnola, "Technology Enabling Interplanetary Trajectories for Nanospacecraft," *Journal of Spacecraft and Rockets*, vol. 55, no. 1, pp. 95–105, jan 2018.

[31] A. R. Tummala and A. Dutta, "An Overview of Cube-Satellite Propulsion Technologies and Trends," *Aerospace*, vol. 4, no. 4, p. 58, dec 2017. [Online]. Available: http://www.mdpi.com/2226-4310/4/4/58

[32] Legifrance, "LOI num. 2008-518 du 3 juin 2008 relative aux opérations spatiales," 2008. [Online]. Available: https://www.legifrance.gouv.fr/affichTexte.do?cidTexte=JORFTEXT000018931380

[33] P. Lascombes, "Electric Propulsion For Small Satellites Orbit Control And Deorbiting : The Example Of A Hall Effect Thruster," in *15th International Conference on Space Operations*, no. June. Reston, Virginia: American Institute of Aeronautics and Astronautics, may 2018, pp. 1–13.

[34] K. Sarda, C. C. Grant, M. Chaumont, S. Y. Choi, B. Johnston-Lemke, and R. E. Zee, "On-Orbit Performance Of The Bright Targer Explorer (BRITE) Nanosatellite Astronomy Constellation," pp. 1–20, 2014.

[35] J. Hudson, K. Lemmer, and A. Hine, "Integration of Micro Electric Propulsion System for CubeSat Orbital Maneuvers," in *AIAA SPACE 2015 Conference and Exposition*. Reston, Virginia: American Institute of Aeronautics and Astronautics, aug 2015, pp. 299–365.

[36] W. Marshall and C. Boshuizen, "Planet Labs' Remote Sensing Satellite System," 2013.

[37] S. Ciaralli, M. Coletti, F. Guarducci, and S. B. Gabriel, "PPTCUP lifetime test results," in *Presented at the 33rd International Electric Propulsion Conference*, The George Washington University, Washington D.C., USA, 2013.

[38] S. Bandyopadhyay, R. Foust, G. P. Subramanian, S.-J. Chung, and F. Y. Hadaegh, "Correction: Review of Formation Flying and Constellation Missions Using Nanosatellites," *Journal of Spacecraft and Rockets*, vol. 53, no. 3, pp. 1–1, 2018.

[39] C. R. Boshuizen, J. Mason, P. Klupar, and S. Shannon, "Results from the Planet Labs Flock Constellation," in *28th Annual AIAA/USU Conference on Small Satellites*, Logan, Utah, USA, 2014.

[40] K. Danzmann, "LISA - An ESA cornerstone mission for the detection and observation of gravitational waves," *Advances in Space Research*, 2003.

[41] B. Cecconi, M. Dekkali, C. Briand, B. Segret, J. N. Girard, A. Laurens, A. Lamy, D. Valat, M. Delpech, M. Bruno, P. Gélard, M. Bucher, Q. Nenon, J. M. Grießmeier, A. J. Boonstra, and M. Bentum, "NOIRE study report:

Towards a low frequency radio interferometer in space," *IEEE Aerospace Conference Proceedings*, vol. 2018-March, pp. 1–19, 2018.

[42] T. Wekerle, J. B. P. Filho, L. E. V. L. da Costa, and L. G. Trabasso, "Status and trends of smallsats and their launch vehicles - An up-to-date review," 2017.

[43] A. T. Klesh, J. D. Baker, J. Bellardo, J. Castillo-Rogez, J. Cutler, L. Halatek, E. G. Lightsey, N. Murphy, and C. Raymond, "INSPIRE: Interplanetary NanoSpacecraft Pathfinder in Relevant Environment," in *AIAA SPACE 2013 Conference and Exposition*. Reston, Virginia: American Institute of Aeronautics and Astronautics, sep 2013, pp. 1–6.

[44] K. Oguri, K. Kakihara, S. Campagnola, N. Ozaki, K. Oshima, T. Yamaguchi, and R. Funase, "EQUULEUS Mission Analysis : Design of the Science Orbit Phase," 2017.

[45] P. Hayne, B. Greenhagen, D. Paige, J. Camacho, B. Cohen, G. Sellar, and J. Reiter, "Lunar Flashlight: Illuminating the Lunar South Pole," in *47th Lunar and Planetary Science Conference*, vol. 3, no. 2016, 2016, pp. 4–5.

[46] L. Mcnutt, L. Johnson, D. Clardy, J. Castillo-Rogez, A. Frick, and L. Jones, "Near-Earth Asteroid Scout," 2014.

[47] A. F. Cheng, A. S. Rivkin, C. Reed, O. S. Barnouin, Z. Fletcher, C. M. Ernst, A. Galvez, I. Carnelli, and P. Michel, "Aida: Asteroid Impact & Deflection Assessment," *64th International Astronautical Congress*, pp. 1–8, 2013.

[48] R. Shimmin, "Trajectory Design for a Very-Low-Thrust Lunar Mission," Doctorate of Phylosophy, The University of Adelaide, 2012.

[49] P. Erichsen, "Sacecraft Propulsion - A brief introduction," mar 2005.

[50] K. Fuhrhop, D. Morris, and B. Gilchrist, "Electron Emission for Electrodynamic Tether Systems in Space," in *40th AIAA/ASME/SAE/ASEE Joint Propulsion Conference and Exhibit*, no. 2004. Reston, Virigina: American Institute of Aeronautics and Astronautics, 2004. [Online]. Available: http://arc.aiaa.org/doi/10.2514/6.2004-3495

[51] G. L. Matloff and E. Mallove, "Solar sail starships: the clipper ships of the galaxy," *Journal of the British Interplanetary Society*, vol. 34, pp. 371–380, 1981.

[52] R. Ridenoure, R. Munakata, and A. Diaz, "LightSail Program Status: One Down, One to Go," *29th AIAA/USU Conference on Small Satellites*, 2015.

[53] P. Wiktor, "Temperature control of a liquid helium propulsion system," *Journal of Propulsion and Power*, vol. 9, no. 4, pp. 536–544, jul 1993. [Online]. Available: http://arc.aiaa.org/doi/10.2514/3.23656

[54] U. Kvell, M. Puusepp, F. Kaminski, J.-E. Past, K. Palmer, T.-A. Grönland, and M. Noorma, "Nanosatellite orbit control using MEMS cold gas thrusters," *Proceedings of the Estonian Academy of Sciences*, vol. 63, no. 2S, p. 279, 2014. [Online]. Available: http://www.kirj.ee/?id=23803{&}tpl=1061{&}c{_}tpl=1064

[55] VACCO, "JPL MarCO Micro CubeSat Propulsion System." [Online]. Available: http://www.cubesat-propulsion.com/jpl-marco-micro-propulsion-system/

[56] NanoSpace, "CubeSat MEMS propulsion module," 2012. [Online]. Available: http://www.sscspace.com/{\protect\T1\textdollar}2/file/cubesat-mems-propulsion-module.pdf

[57] GOMSpace, "MEMS Cold Gas Propulsion Module for 2-3U nanosatellites," 2019. [Online]. Available: https://gomspace.com/shop/subsystems/attitude-orbit-control-systems/nanoprop-3u-propulsion.aspx

[58] VACCO, "NEA Scout Propulsion System." [Online]. Available: https://www.cubesat-propulsion.com/nea-scout-propulsion-system/ http://www.cubesat-propulsion.com/nea-scout-propulsion-system/

[59] VACCO, "CuSP Propulsion System." [Online]. Available: https://www.cubesat-propulsion.com/cusp-propulsion-system/

[60] T. K. Imken, T. H. Stevenson, and E. G. Lightsey, "Design and Testing of a Cold Gas Thruster for an Interplanetary CubeSat Mission," *JoSS*, vol. 4, no. 2, pp. 371–386, 2015. [Online]. Available: http://www.jossonline.com/wp-content/uploads/2015/12/Final-Design-and-Testing-of-a-Cold-Gas-Thruster-for-an-Interplanetary-CubeSat-Mission.pdf

[61] B. W. Risi, "Propulsion System Development for the CanX-4 and CanX-5 Dual Nanosatellite Formation Flying Mission," Thesis submitted for the degree of Master of Applied Science, University of Toronto, 2014.

[62] K. Cote, J. Gabriel, B. Patel, N. Ridley, Z. Taillefer, and S. Tetreault, "Mechanical, Power, and Propulsion Subsystem Design for a CubeSat," Project submitted for the degree of Bachelor of Science in Aerospace Engineering, Worcester Polytechnic Institute, 2011.

[63] VACCO, "MEPSI Micro CubeSat Propulsion System." [Online]. Available: http://www.cubesat-propulsion.com/mepsi-micro-propulsion-system/

[64] VACCO, "Standard Micro CubeSat Propulsion System." [Online]. Available: http://www.cubesat-propulsion.com/standard-micro-propulsion-system/

[65] VACCO, "End-Mounted Standard Micro-Propulsion System for CubeSat." [Online]. Available: http://www.cubesat-propulsion.com/end-mounted-standard-mips/

[66] A. Williams, "CubeSat Proximity Operations Demonstration (CPOD) Overview," *CubeSat Industry Days*, pp. 1–16, 2015. [Online]. Available: http://www.nasa.gov/sites/default/files/files/A{_}Williams-A{_}Tsuda-CPOD{_}Overview.pdf

[67] VACCO, "NASA C-POD Micro CubeSat Propulsion System." [Online]. Available: https://www.cubesat-propulsion.com/reaction-control-propulsion-module/

[68] VACCO, "Boeing Palomar Micro CubeSat Propulsion System." [Online]. Available: http://www.cubesat-propulsion.com/palomar-micro-propulsion-system/

[69] R. K. Masse, C. B. Carpenter, D. T. Schmuland, J. Overly, and M. Y. Allen, "CubeSat High-impulse Adaptable Modular Propulsion System (CHAMPS) Product Line Development Status and Mission Applications," in *49th AIAA/ASME/SAE/ASEE Joint Propulsion Conference*. Reston, Virginia: American Institute of Aeronautics and Astronautics, jul 2013. [Online]. Available: http://www.rocket.com/files/aerojet/documents/CubeSat/AIAA-2013-3760.pdfhttp://arc.aiaa.org/doi/10.2514/6.2013-3760

[70] Aerojet Rocketdyne, "MPS-120 CubeSat High-Impulse Adaptable Modular Propulsion System (CHAMPS)." [Online]. Available: http://www.rocket.com/cubesat/mps-120

[71] S. Powell, T. Knop, and S. Engelen, "Experimental evaluation of a green bi-propellant thruster for small satellite applications," in *Proceedings of the AIAA/USU Conference on Small Satellites*, aug 2016.

[72] Hyperion Technologies, "PM400," 2016. [Online]. Available: http://hyperiontechnologies.nl/products/pm400/

[73] Hyperion Technologies, "PM200," 2017. [Online]. Available: http://hyperiontechnologies.nl/products/pm200/

[74] NanoAvionics, "CubeSat Propulsion "EPSS" – Green Chemical Propulsion System," 2019. [Online]. Available: http://n-avionics.com/propulsion-systems/small-satellite-green-chemical-propulsion-system-epss/

[75] M. Tsay, J. Frongillo, D. Lafko, and J. Zwahlen, "Development Status and 1U CubeSat Application of Busek's 0,5N Green Monopropellant Thruster," in *Proceedings of the AIAA/USU Conference on Small Satellites*, 2014.

[76] Busek, "Green Monopropellant Thrusters," 2016. [Online]. Available: http://www.busek.com/technologies{_}{_}greenmonoprop.htm

[77] VACCO, "Hybrid ADN Delta-V / RCS System." [Online]. Available: http://www.cubesat-propulsion.com/hybrid-adn-delta-v-rcs-system/

[78] Gunter's Space, "ArgoMoon," 2017. [Online]. Available: http://space.skyrocket.de/doc{_}sdat/argomoon.htm

[79] VACCO, "ArgoMoon Propulsion System." [Online]. Available: http://www.cubesat-propulsion.com/argomoon-propulsion-system/

[80] VACCO, "Lunar Flashlight Propulsion System." [Online]. Available: http://www.cubesat-propulsion.com/lunar-flashlight-propulsion-system/

[81] Aerojet Rocketdyne, "MPS-130 CubeSat High-Impulse Adaptable." [Online]. Available: http://www.rocket.com/cubesat/mps-130

[82] V. Ethier, L. Paritsky, T. Moser, J. Slostad, and R. Hoyt, "Development of a CubeSat Water Electrolysis Propulsion System," in *Proceedings of the AIAA/USU Conference on Small Satellites*, 2013.

[83] K. James, M. Bodnar, M. Freedman, L. Osborne, R. Grist, and R. Hoyt, "HYDROS: High performance water-electrolysis propulsion for CubeSats and miscrosats," in *40th annual AAS Guidance & Control conference*, 2017. [Online]. Available: http://www.tethers.com/papers/AAS17-145{_}HYDROS{_}JAMES.pdf

[84] A. Fanfani, "D-SAT Mission: an In-Orbit Demonstration of Satellite Controlled Re-entry," in *Clean Space Industrial Days*, 2017.

[85] K. L. Zondervan, J. Fuller, D. Rowen, B. Hardy, C. Kobel, S.-h. Chen, P. Morrison, T. Smith, and A. Kremer, "CubeSat Solid Rocket Motor Propulsion Systems providing D Vs greater than 500 m / s," *Proceedings of the AIAA/USU Conference on Small Satellites*, no. August, 2014.

[86] U. Siddiqui, "Updated Performance Measurements of the Phase Four RF Thruster," *34th Space Symposium, Technical Track*, 2018. [Online]. Available: http://phasefour.io/wp-content/uploads/2018/04/Siddiqui-Tech-Track-Paper-Updated-Performance-Measurements-of-the-Phase-Four-RF-Thruster-2018.pdf

[87] PHASE FOUR, "PHASE FOUR RF Thruster," 2018. [Online]. Available: http://www.phasefour.io/product/

[88] M. U. Siddiqui, C. Cretel, J. Synowiec, A. G. Hsu, J. A. Young, and R. Spektor, "First Performance Measurements of the Phase Four RF Thruster," in *35th International Electric Propulsion Conference*, Atlanta, Georgia, USA, 2017. [Online]. Available: http://phasefour.io/wp-content/uploads/2017/09/Siddiqui-et-al-P4-RFT-2017.pdf

[89] Sitael, "XR-150 resistojet," 2017. [Online]. Available: http://www.sitael.com/wp-content/uploads/ProductSheet/XR-150.pdf

[90] G. Cifali, S. Gregucci, T. Andreussi, and M. Andrenucci, "Resistojet Thrusters for Auxiliary Propulsion of Full Electric Platforms," in *35th International Electric Propulsion Conference*, Atlanta, Georgia, USA, 2017. [Online]. Available: https://iepc2017.org/sites/default/files/speaker-papers/iepc-2017-371.pdf

[91] N. Arcis, A. Bulit, M. Gollor, P. Lionnet, J. C. Treuet, and I. A. Gomez, "Database on EP (and EP-related) technologies and TRL," Centre National d'Etudes Spatiales, Tech. Rep., 2015.

[92] Busek, "Busek Micro Resistojet." [Online]. Available: http://www.busek.com/index{_}htm{_}files/70008518B.pdf

[93] D. L. Carroll, J. M. Cardin, R. L. Burton, Benavides G. F., N. Hejmanowski, C. Woodruff, K. Bassett, D. King, J. Laystrom-Woodard, L. Richardson, C. Day, K. Hageman, and R. Bhandari, "Propulsion Unit For CubeSats (PUC)," in *62nd JANNAF Propulsion Meeting (7th Spacecraft Propulsion)*, Nashville, USA, jun 2015.

[94] CU Aerospace, "Propulsion Unit for CubeSats (PUC-SO2)," 2018. [Online]. Available: http://www.cuaerospace.com/Portals/2/SiteContent/pdfs/datasheets/PUC/PUC-Brochure-180710.pdf

[95] CU Aerospace, "Monofilament Vaporization Propulsion (MVP) System." [Online]. Available: http://www.cuaerospace.com/Portals/2/SiteContent/pdfs/datasheets/MVP/MVP-Datasheet-v8.pdf

[96] S. Ciaralli, M. Coletti, and S. B. Gabriel, "Results of the qualification test campaign of a Pulsed Plasma Thruster for Cubesat Propulsion (PPTCUP)," *Acta Astronautica*, vol. 121, pp. 314–322, apr 2016. [Online]. Available: http://linkinghub.elsevier.com/retrieve/pii/S0094576515003318

[97] Mars Space Ltd, "Pulsed Plasma Thruster (PPT) projects," 2018. [Online]. Available: https://mars-space.co.uk/ppt

[98] Busek, "BmP-220 Micro-Pulsed Plasma Thruster," 2016. [Online]. Available: http://www.busek.com/index{_}htm{_}files/70008502BmP-220DataSheetRevF.pdf

[99] S. Barral, J. Kurzyna, A. Szelecka, H. Rachubinski, E. Remirez, R. Martin, P. Ortiz, J. Alonso, S. Bottinelli, Y. Mabillard, A. Zaldívar, P. Rangsten, and C. R. Koppel, "First Experimental Characterization of a Pulsed Plasma Thruster with Non-Volatile Liquid Propellant," in *SPACE PROPULSION 2014*, Cologne, Germany, 2014.

[100] S. Barral, J. Kurzyna, A. Szelecka, H. Rachubinski, D. Danilko, R. Martín, E. Remírez, P. Ortiz, J. Alonso, Y. Mabillard, S. Bottinelli, A. Zaldívar, P. Rangsten, and C. R. Koppel, "Time-Of-Flight Spectrometry and Performance of a Pulsed Plasma Thruster with Non-Volatile Propellant," in *Joint Conference of 30th ISTS, 34th IEPC and 6th NSAT*, Hyogo-Kobe, Japan, jul 2015.

[101] M. Keidar, "Micro-Cathode Arc Thruster for small satellite propulsion," in *2016 IEEE Aerospace Conference*. IEEE, mar 2016, pp. 1–7. [Online]. Available: http://ieeexplore.ieee.org/document/7500506/

[102] M. Keidar, T. Zhuang, A. Shashurin, G. Teel, D. Chiu, J. Lukas, S. Haque, and L. Brieda, "Electric propulsion for small satellites," *Plasma Physics and Controlled Fusion*, vol. 57, no. 1, p. 014005, jan 2015. [Online]. Available: http://iopscience.iop.org/article/10.1088/0741-3335/57/1/014005/pdfhttp://stacks.iop.org/0741-3335/57/i=1/a=014005?key=crossref.d4b21d8033ccd743778fa7b5e359cb08

[103] L. Herrero, "Plasma jet pack technology overview," in *35th International Electric Propulsion Conference*, Atlante, Georgia, USA, 2017.

[104] J. K. Pittman, J. Corbett, E. Hanlon, M. Keidar, C. Kelly, C. Tingler, C. Vincent, and J. S. Kang, "Microcathode–Cold Gas Hybrid Propulsion System - BRICSat," in *32nd Space Symposium, Technical Track*, Colorado Springs, Colorado, USA, apr 2016.

[105] M. Tsay, J. Frongillo, and K. Hohman, "Iodine-Fueled Mini RF Ion Thruster for CubeSat Applications," in *Joint Conference of 30th ISTS, 34th IEPC and 6th NSAT*, Hyogo-Kobe, Japan, jul 2015.

[106] Busek, "Ion Thrusters." [Online]. Available: http://www.busek.com/technologies{_}{_}ion.htm

[107] M. Tsay, J. Frongillo, J. Model, J. Zwahlen, and L. Paritsky, "Flight Development of Iodine BIT-3 RF Ion Propulsion System for SLS EM-1 CubeSats," in *Proceedings of the AIAA/USU Conference on Small Satellites*, North Logan, Utah, USA, aug 2016.

[108] H. J. Leiter, C. Altmann, R. Kukies, J. Kuhmann, J.-P. Porst, M. Berger, and M. Rath, "Evolution of the AIRBUS DS GmbH Radio Frequency Ion Thruster Family," in *Joint Conference of 30th ISTS, 34th IEPC and 6th NSAT*, Hyogo-Kobe, Japan, jul 2015.

[109] Ariane Group, "Electric Ion Space Propulsion Systems and Thrusters," 2017. [Online]. Available: http://www.space-propulsion.com/spacecraft-propulsion/propulsion-systems/electric-propulsion/index.html

[110] E. H. Hall, "On a New Action of the Magnet on Electric Currents," *American Journal of Mathematics*, vol. 2, no. 3, pp. 287–292, 1879.

[111] A. Reissner, N. Buldrini, B. Seifert, T. Hörbe, F. Plesescu, and C. Scharlemann, "Introducing very high Δv Capability to Nanosats and Cubesats," in *Joint Conference of 30th International Symposium on Space Technology and Science 34th International Electric Propulsion Conference and 6th Nanosatellite Symposium*, Hyogo-Kobe, Japan, jul 2015.

[112] Enpulsion, "IFM Nano Thruster." [Online]. Available: https://www.enpulsion.com/

[113] Sitael, "HT100." [Online]. Available: http://www.sitael.com/wp-content/uploads/ProductSheet/HT100.pdf

[114] Busek, "BHT-200." [Online]. Available: http://www.busek.com/index{_}htm{_}files/70000700BHT-200DataSheetRev-.pdf

[115] N. Heitz, D. Henri, P. Lascombes, and J.-L. Maria, "Hall Effect Thruster for small satellites," in *35th International Electric Propulsion Conference*, Atlante, Georgia, USA, 2017.

[116] D. Krejci, "Demonstration of the ifm nano feep thruster in low earth orbit," in *4S Symposium*, 2018.

[117] D. Krejci, F. Mier-Hicks, C. Fucetola, P. C. Lozano, A. H. Schouten, and F. Martel, "Design and Characterization of a Scalable ion Electrospray Propulsion System," *Joint Conference of 30th ISTS, 34th IEPC and 6th NSAT, Hyogo-Kobe, Japan*, pp. 1–11, 2015.

[118] D. Krejci and P. Lozano, "Scalable ionic liquid electrospray thrusters for nanosatellites," *Advances in the Astronautical Sciences*, vol. 157, pp. 801–810, 2016.

[119] D. Krejci and P. Lozano, "CubeSat constellation management using Ionic Liquid Electrospray Propulsion," *Acta Astronautica*, vol. 151, no. September 2017, pp. 243–252, 2018. [Online]. Available: https://doi.org/10.1016/j.actaastro.2018.06.007

[120] Accion Systems, "Tiles Ionic Liquid Electrospray," 2017. [Online]. Available: https://www.accion-systems.com/tile

[121] Accion Systems, "Ion Electrospray Propulsion - Our Technology," 2017. [Online]. Available: https://www.accion-systems.com/our-technology/

[122] Busek, "BET-100 Busek Electrospray Thruster," 2016. [Online]. Available: http://www.busek.com/index{_}htm{_}files/70008516F.PDF

[123] Busek, "BET-1mN Busek Electrospray Thruster," 2016. [Online]. Available: http://www.busek.com/index{_}htm{_}files/70008500BET-1mNDataSheetRevH.pdf

[124] CubeSpace, "CubeWheel Small." [Online]. Available: https://www.cubesatshop.com/product/cubewheel-small/

[125] ISIS, "ISIS Magnetorquer board." [Online]. Available: https://www.cubesatshop.com/product/isis-magnetorquer-board/

[126] Blue Canyon Technologies, "XACT." [Online]. Available: https://bluecanyontech.com/components

[127] X. Xia, Z. Li, T. Wang, Y. Bai, S. Wu, and Z. Mu, "Nanopropulsion-based orbit maneuver scheme for CubeSat," in *2016 35th Chinese Control Conference (CCC)*, vol. 34, no. 11. IEEE, jul 2016, pp. 10 780–10 787.

[128] J. Hudson, S. Spangelo, A. Hine, D. Kolosa, and K. Lemmer, "Mission Analysis for CubeSats with Micropropulsion," *Journal of Spacecraft and Rockets*, vol. 53, no. 5, pp. 836–846, sep 2016.

[129] S. Spangelo and B. Longmier, "Optimization of CubeSat System-Level Design and Propulsion Systems for Earth-Escape Missions," *Journal of Spacecraft and Rockets*, vol. 52, no. 4, pp. 1009–1020, jul 2015.

[130] A. Elfving, "The Attitude and Orbit Control of XMM," *ESA Bulletin*, vol. 100, 1999. [Online]. Available: http://www.esa.int/esapub/bulletin/bullet100/ELFVING.pdf

[131] A. Scholz, "Implementation of Advanced Attitude Determination and Control Techniques into a Nanosatellite," Master Thesis, National Cheng Kung University, 2008.

[132] J. J. Likar, S. E. Stone, R. E. Lombardi, and K. A. Long, "Novel Radiation Design Approach for CubeSat Based Missions," *24th Annual AIAA/USU Conference on Small Satellites*, 2010.

[133] R. L. Staehle, D. Blaney, H. Hemmati, and D. Jones, "Interplanetary CubeSats: Opening the Solar System to a Broad Community at Lower Cost," 2013.

[134] S. R. Starin and J. Eterno, "Spacecraft Attitude Determination and Control Systems," 2011, pp. 565–591.

[135] ISIS, "CubeSat Solar Panels," 2019. [Online]. Available: https://www.cubesatshop.com/product/single-cubesat-solar-panels/

[136] C. Clark and R. Logan, "Power Budgets for Mission Success," 2011.

[137] J. E. Pollard, "Simplified Approach for Assessment of Low-Thrust Elliptical Orbit Transfers," *Proceedings of the International Electric Propulsion Conference 1997 (IEPC97)*, no. 1, pp. 979–986, 1997.

[138] J. B. Kuipers, *Quaternions and rotation sequences - A primer with applications to orbits, aerospace and virtual reality*, Princeton University Press, Ed. Princeton University Press, 1999.

[139] NIMA, "Department of Defense World Geodetic System 1984," *Technical Report 8350.2, Third Edition*, p. 175, 2000. [Online]. Available: http://earth-info.nga.mil/GandG/publications/tr8350.2/wgs84fin.pdf

[140] J. L. Junkins and H. Schaub, *Analytical Mechanics of Space Systems, Second Edition*, 2nd ed. Reston ,VA: American Institute of Aeronautics and Astronautics, jan 2009. [Online]. Available: http://dlx.b-ok.org/genesis/1160000/dd03ccd494abe67fbc10d3c733c54041/{_}as/[H.{_}Schaub,{_}J.{_}Junkins]{_}Analytical{_}Mechanics{_}of{_}Sp(b-ok.org).pdfhttp://arc.aiaa.org/doi/book/10.2514/4.867231

[141] N. A. Gatsonis, Y. Lu, J. Blandino, M. A. Demetriou, and N. Paschalidis, "Micropulsed Plasma Thrusters for Attitude Control of a Low-Earth-Orbiting CubeSat," *Journal of Spacecraft and Rockets*, vol. 53, no. 1, pp. 57–73, jan 2016. [Online]. Available: https://arc.aiaa.org/doi/10.2514/1.A33345

[142] NASA, "Spacecraft magnetic torques," NASA, Tech. Rep. March 1969, 1969.

[143] D. A. Vallado and D. Finkleman, "A critical assessment of satellite drag and atmospheric density modeling," *Acta Astronautica*, vol. 95, no. 1, pp. 141–165, 2014. [Online]. Available: http://dx.doi.org/10.1016/j.actaastro.2013.10.005

[144] NewSpace, "NCTR-M002 Magnetorquer Rod." [Online]. Available: https://www.cubesatshop.com/product/nctr-m002-magnetorquer-rod/

[145] NanoAvionics, "Magnetorquer "SatBus MTQ"." [Online]. Available: https://n-avionics.com/subsystems/cubesat-magnetorquer-satbus-mtq/

[146] GOMSpace, "NanoTorque GST-600," 2019. [Online]. Available: https://gomspace.com/shop/subsystems/attitude-orbit-control-systems/nanotorque-gst-600.aspx

[147] CubeSpace, "CubeWheel Medium." [Online]. Available: https://www.cubesatshop.com/product/cubewheel-medium/

[148] CubeSpace, "CubeWheel Large." [Online]. Available: https://www.cubesatshop.com/product/cubewheel-large/

[149] GOMSpace, "NanoTorque GSW-600," 2019. [Online]. Available: https://gomspace.com/shop/subsystems/attitude-orbit-control-systems/nanotorque-gsw-600.aspx

[150] NanoAvionics, "SatBus 4RW0." [Online]. Available: https://n-avionics.com/subsystems/cubesat-reaction-wheels-control-system-satbus-4rw/

[151] M. J. Sidi, *Spacecraft Dynamics and Control*. Cambridge: Cambridge University Press, 1997, vol. 7, no. 9.

[152] G. A. Landis, S. R. Oleson, M. L. McGuire, L. M. Burke, M. C. Martini, J. E. Fittje, and T. W. Packard, "A Cubesat Asteroid Mission: Propulsion Trade-offs," in *50th AIAA/ASME/SAE/ASEE Joint Propulsion Conference*, 2014.

[153] K. Miyata and J. C. V. D. Ha, "Attitude Control By Magnetic Torquer," pp. 1041–1060.

[154] D. A. Vallado and W. D. McClain, *Fundamentals of Astrodynamics and Applications*, 4th ed. Microcosm Press, 2013.

[155] A. E. Petropoulos, Z. B. Tarzi, G. Lantoine, T. Dargent, and R. Epenoy, "Techniques for designing many-revolution, electric-propulsion trajectories," *Advances in the Astronautical Sciences*, vol. 152, no. May, pp. 2367–2385, 2014.

[156] T. N. Edelbaum, "Propulsion Requirements for Controllable Satellites," *ARS Journal*, vol. 31, no. 8, pp. 1079–1089, aug 1961. [Online]. Available: http://arc.aiaa.org/doi/10.2514/8.5723

[157] J. A. Kechichian, "Reformulation of Edelbaum's Low-Thrust Transfer Problem Using Optimal Control Theory," *Journal of Guidance, Control, and Dynamics*, vol. 20, no. 5, pp. 988–994, sep 1997.

[158] A. E. Petropoulos, "Simple control laws for low-thrust orbit transfers," *AAS/AIAA Astrodynamics Specialists Conference*, 1998.

[159] D. Gaylor, "Analysis of Low Thrust Orbit Transfers Using the Lagrange Planetary Equations," 2000. [Online]. Available: http://lightsey.ae.utexas.edu/publications/cm1project-gaylor.pdf

[160] A. Ruggiero, P. Pergola, S. Marcuccio, M. Andrenucci, P. Manager, and V. President, "Low-Thrust Maneuvers for the Efficient Correction of Orbital Elements," *32nd International Electric Propulsion Conference*, 2011.

[161] J. A. Reiter, A. K. Nicholas, and D. B. Spencer, "Optimization of many-revolution, electric-propulsion trajectories with engin shutoff constraints," in *25th AAS/AIAA Flight Mechanics Meeting*. Reston ,VA: American Institute of Aeronautics and Astronautics, jan 2015. [Online]. Available: https://arc.aiaa.org/doi/book/10.2514/4.861543

[162] G. Quinsac, B. Segret, C. R. Koppel, and B. Mosser, "Attitude control : a key factor during the design of low-thrust propulsion for CubeSats," *Manuscript submitted for publication*, 2019.

[163] C. Koppel and G. Quinsac, "Electric Thruster Selection Criteria," in *8th European Conference for Aeronautics and Space Sciences (EUCASS)*, 2019.

[164] M. Nehrenz and M. Sorgenfrei, "A Comparison of Thruster Implementation Strategies for a Deep Space Nanosatellite," in *AIAA Guidance, Navigation, and Control Conference*, no. January 2015. Reston, Virginia: American Institute of Aeronautics and Astronautics, jan 2015.

[165] M. A. Silva, D. C. Guerrieri, A. Cervone, and E. Gill, "A review of MEMS micropropulsion technologies for CubeSats and PocketQubes," *Acta Astronautica*, vol. 143, no. December 2017, pp. 234–243, 2018.

[166] E. Thébault, C. C. Finlay, C. D. Beggan, P. Alken, J. Aubert, O. Barrois, F. Bertrand, T. Bondar, A. Boness, L. Brocco, E. Canet, A. Chambodut, A. Chulliat, P. Coïsson, F. Civet, A. Du, A. Fournier, I. Fratter, N. Gillet, B. Hamilton, M. Hamoudi, G. Hulot, T. Jager, M. Korte, W. Kuang, X. Lalanne, B. Langlais, J.-M. Léger, V. Lesur, F. J. Lowes, S. Macmillan, M. Mandea, C. Manoj, S. Maus, N. Olsen, V. Petrov, V. Ridley, M. Rother, T. J. Sabaka, D. Saturnino, R. Schachtschneider, O. Sirol, A. Tangborn, A. Thomson, L. Tøffner-Clausen, P. Vigneron, I. Wardinski, and T. Zvereva, "International Geomagnetic Reference Field: the 12th generation," *Earth, Planets and Space*, vol. 67, no. 1, p. 79, dec 2015.

[167] F. L. Markley and J. L. Crassidis, *Fundamentals of Spacecraft Attitude Determination and Control*. New York, NY: Springer New York, 2014, vol. 2. [Online]. Available: http://link.springer.com/10.1007/978-1-4939-0802-8

[168] J. R. Wertz, *Spacecraft Attitude Determination and Control*, ser. Astrophysics and Space Science Library, J. R. Wertz, Ed. Dordrecht: Springer Netherlands, 1978, vol. 73. [Online]. Available: http://link.springer.com/10.1007/978-94-009-9907-7

[169] J. M. Picone, A. E. Hedin, D. P. Drob, and A. C. Aikin, "NRLMSISE-00 empirical model of the atmosphere: Statistical comparisons and scientific issues," *Journal of Geophysical Research: Space Physics*, vol. 107, no. A12, pp. 1–16, 2002.

[170] M. Blanke and M. B. Larsen, "Satellite Dynamics and Control in a Quaternion Formulation - Lecture note for course 31365 Spacecraft Dynamics and Control at DTU," 2010.

RÉSUMÉ

L'apparition du standard CubeSat a profondément modifié le domaine des nano/microsatellites, notamment en promouvant la standardisation, des développements plus courts et des lancements partagés. L'intérêt combiné des agences spatiales et des entreprises a résulté en une forte croissance des lancements de CubeSats depuis vingt ans. De nombreux « composants sur étagère » sont maintenant développés dans le respect de ce standard. Pourtant, les contraintes importantes résultant de ce format réduit en termes de masse, volume et puissance disponibles ont jusqu'à présent limité l'envoi de CubeSats aux orbites terrestres basses. Des progrès sont en cours pour ce qui concerne le contrôle orbital et doivent permettre d'offrir à ces satellites plus de flexibilité, et notamment ouvrir la porte à des missions plus exotiques telles que des missions interplanétaires.
Cette thèse s'intéresse aux difficultés d'application de la philosophie des CubeSats au Système de Contrôle d'Attitude et d'Orbite (SCAO). L'utilisation de composants sur étagère pousse à considérer chaque sous-système indépendamment, pouvant conduire à des performances dégradées au niveau du satellite. En particulier, la distinction entre le système de contrôle d'attitude et celui d'orbite (SCA/GNC) cache des impacts mutuels. Ce travail développe une analyse de haut niveau sur différents cas d'étude représentatifs des besoins identifiés tels que la désorbitation depuis une orbite basse, la sortie de l'orbite terrestre ou encore les opérations de proximité. Une analyse fonctionnelle met l'accent sur les connexions entre les différents sous-systèmes nécessaires à la réussite de ces manœuvres orbitales. Il en ressort que l'approche conventionnelle a tendance à considérer que le contrôle de la direction de poussée ne nécessite pas de sous-système dédié. Les indices de performances usuels des systèmes de propulsions sont quant à eux lacunaires. Ils mettent l'accent sur la masse de carburant aux dépens de la masse sèche du système, et ils omettent la masse supplémentaire que représentent les besoins électriques et thermiques, conduisant parfois à des propositions infaisables au format CubeSat.
L'impact des propulseurs sur le design du SCA est quantifié à travers le développement d'un environnement de simulation du SCAO. On y observe d'importantes augmentations de la durée des manœuvres et de la consommation de carburant, voire une perte du satellite. En conséquence, des propositions sont faites pour permettre la réalisation du contrôle orbital souhaité. La description classique des systèmes de propulsion est quant à elle revisitée afin de fournir un indice prenant en compte l'ensemble des effets liés à l'intégration de propulseurs.

MOTS CLÉS

SCAO, Propulsion, GNC, SCA, Manoeuvre orbitale, Opérations de proximité, Impulsion système spécifique

ABSTRACT

The domain of nano/microsatellites has been irreversibly modified by the apparition of the CubeSat standard. The exponential growth of CubeSat launches during the past 20 years, combined with the growing interest of private companies and space agencies has confirmed the sustainability of a new approach to space missions: standardization, short release cycle and shared launches. This standard has paved the way to the democratization of subsystems available as "commercial off-the-shelf" (COTS). However, because of the drastic constraints imposed by the standard in terms of mass, volume and power, most CubeSats to date were launched in Low Earth Orbit (LEO). Among the limitations that this class of satellites still faces is the orbit control. It is expected to allow more flexibility to LEO missions and pave the way to interplanetary trajectories.
This thesis aims to highlight the remaining discrepancies between the CubeSat philosophy and the complexity of the Attitude and Orbit Control System (AOCS), and tackle some of them. Current "commercial off-the-shelf" (COTS) approach tends to consider each subsystem individually, making it difficult to ensure performances at system level. For our concern, the distinction between the attitude control and the orbit control (ADCS/GNC) hides inherent mutual impacts. This work proposes a high-level approach based on identified representative cases, such as deorbiting from LEO, escaping Earth orbit or proximity operations. Thanks to a functional analysis, the fundamental links between the required subsystems for a successful orbital maneuver are emphasized. It results that the conventional approach tends to neglect the attitude control required to ensure the expected pointing during the maneuver, usually considered to be within the limits of the non-dedicated ADCS. Classical performance indexes for propulsion systems are proved to be deficient, for instance focusing on the propellant mass at the expense of the dry mass of the system. They also omit the effects of the power and thermal requirements in terms of added mass, which sometimes result in unrealistic solutions at the CubeSat scale.
The thrusters' impact on the design of the ADCS is quantified through the development of an AOCS simulation environment. Important increases in maneuver duration and propellant consumption, even mission loss, are observed. They lead to propositions for ensure the success of expected orbital maneuvers. COTS propulsion systems' classical description is revisited with an enhanced system performance index, taking into account the multiple implications of a thruster integration.

KEYWORDS

AOCS, Propulsion, GNC, ADCS, Orbital maneuver, Proximity operation, System specific impulse